MASTER'S THESIS

For the degree of
Master of Science in Condensed Matter Physics

Characterization and use of permanent magnets with extremely strong field gradients

Inge Buanes Roth

May 24, 2009
Department of Physics
University of Oslo

IFE Institute for Energy Technology

Research for a better future

Characterization and use of permanent magnets with extremely strong field gradients

May 24, 2009
Inge Buanes Roth

Main supervisor: Arne Skjeltorp, Co-supervisor: Geir Helgesen
Advanced Materials and Complex Systems
Condensed Matter Physics - Department of Physics
Faculty of Mathematics and Natural Sciences
University of Oslo
&
Institute for Energy Technology

Abstract

Strong rare-earth *permanent magnets* have become relatively cheap to produce, and play an important role in the development of modern technology. One example is the integration of magnetophoresis and microfluidics, where permanent magnets are miniaturized and integrated onto lab-on-chip devices with the help of micro-electro-mechanical systems techniques.

A structure of two adjoined giant magnetic anisotropy rare-earth magnets with opposite directions of magnetization produces a very *strong* and *inhomogeneous* magnetic stray field. The field is several times stronger than the induction of the rare-earth material itself, and $\mathbf{B}\nabla\mathbf{B}$ reaches theoretical and simulated values of 10^8-10^{10} mT^2/m. Building upon this basis, a new design adds two thin, soft magnetic masks on top of the magnets, forming a small air gap directly above the junction line between them, in order to adjust the shape and strength of the stray field.

Simulations with 50 μm thick vanadium permendur masks show that, when the gap size decreases towards 50 μm, the tangential component of the stray field increases with a factor of 20%, and narrows in width comparable to the gap size. In a distance of 10 μm from the masks $\mathbf{B}\nabla\mathbf{B}$ now exceeds 10^{11} mT^2/m. The normal and tangential gradient of $\mathbf{B}$ are oppositely directed and on the same order, nevertheless, the tangential field is several times stronger than the normal field, thus the main contributor to $\mathbf{B}\nabla\mathbf{B}$.

Singularities in the demagnetization field above the corners of the masks are responsible for most of the increase and distortion of the magnetic stray field. However, above a *critical* distance of 40 μm they are undetectable. The stray field is now automatically reduced since the masks increase the absolute distance to the source of the field. Thus depending on mask thickness, all $\mathbf{B}\nabla\mathbf{B}$ distributions are correspondingly decreased. Magnetic separation of large bulk quantities is thus performed better in a device without masks, while separation of small quantities in confined regions, beneath the critical distance, benefits significantly from the new design.

Experimental results indicate that, the simulations predict close to realistic results above the critical distance. The experiments are, however, not performed close enough to observe the singularities, and the full extent of the simulations can thus not be verified. Nevertheless, as a consequence by the fact that, keeping corners perfectly square and junctions between materials ideal in a real device, simulations where $\mathbf{B}\nabla\mathbf{B}$ exceeds 10^{11} mT^2/m are not realistic. A more realistic value is 10^{10} mT^2/m, still several times larger than that in simulations of a structure without masks.

The new design is thus superior for separation purposes in microfluidic environments, if the separation distance is less than 40 μm. Developing new and better magnet and mask material compounds, as well as perfecting techniques ensuring ideal magnet-mask and magnet-magnet junctions will increase its potency even further.

Preface

This thesis is submitted for the degree of Master of Science in Condensed Matter Physics at the University of Oslo in collaboration with Institute for Energy Technology, and is wholly my work. It is the result of 10 months of arduous but rewarding work under the supervision of Geir Helgesen, and Arne Skjeltorp.

I happily seized this assignment because of its intriguing nature, and I understood the significance of investigating some of the unanswered questions it needed answers for. I also had the opportunity to work for IFE, and by doing so introducing me to a new and exciting environment.

I have relied on the guidance and help of many. Firstly, I would like to thank everyone at the physics department at IFE for their help and confidence in me, and especially my supervisor Geir Helgesen. Secondly, a big thanks to the electronics department at IFE helping me with my ever changing experimental equipment. Lastly, I can not thank my family enough for their never failing encouragements and support, and particularly my father for carefully proof-reading my work.

Thank you.

Inge Buanes Roth
May 24, 2009
University of Oslo
&
Institute for Energy Technology

Contents

List of Symbols

Symbol	Description	Unit
$\mathbf{A}$	Magnetic vector potential	T m , Wb m^{-1}
$\mathbf{B}$	Magnetic flux density	T , Wb m^{-2}
$\mathbf{H}$	Magnetic field strength	A m^{-1}
$\mathbf{M}$	Magnetization, volumetric	A m^{-1}
$\mathbf{J}$	Electric current density	A m^{-2}
μ	Permeability	H m^{-1} , N A^{-2}
μ_0	Vacuum permeability	$4\pi 10^{-7}$ H m^{-1}
χ_v	Susceptibility, volumetric	1
I	Electric current	A
q	Electric charge	C
$\mathbf{F}$	Force	kg m s^{-2}
$\mathbf{u}$	Fluid velocity	m s^{-1}
$\mathbf{v}$	Rigid body translational velocity	m s^{-1}
η	Viscosity, dynamic	kg m^{-1} s^{-1} , Pa s
$\mathbf{r}$	Position vector	m
a	Particle radius	m
m	Mass	kg
ρ	Mass density	kg m^{-3}
τ	Time constant	s
b	Mobility	s kg^{-1}

List of Figures

List of Tables

Chapter 1

Introduction

Ever since the discovery of magnetism, magnets and magnetic fields have been important tools in instruments, both in physics and experimental techniques. Today magnets are used in anything from car engine speed sensors to computer hard drive recording, and reading heads. In recent time, with the introduction of nanotechnology, a growing demand for magnets producing stronger and more inhomogeneous magnetic fields in smaller environments, has pushed science far beyond what only thirty-forty years ago seemed a daunting task. Still, applications based on magnetic properties have conventionally been dominated by strong magnetic fields produced exclusively by cooled solenoids, electromagnets, and superconducting magnets. Recently, however, the literature reports about *permanent magnet* systems, able to produce strong and inhomogeneous magnetic fields reaching field values of up to 5T. Moreover, it is anticipated that micro-electro-mechanical systems techniques, for fabrication of miniaturized magnets, can integrate such permanent magnetic structures into microfluidic analysis systems, thus widely expanding the possibilities for applications based on magnetophoresis.

1.1 Background

In the following we study an invention based on a half open Kittel domain, consisting two adjoined giant magnetic anisotropy rare-earth magnets with opposite directions of magnetization. At the top edges where the magnets meet, a very strong and inhomogeneous magnetic stray field is produced, several times stronger than the induction of the rare-earth material itself, and $\mathbf{B}\nabla\mathbf{B}$ reaches values of 10^8-10^{10} mT^2/m.

An innovative design proposes to add two thin, soft magnetic masks, forming a small air gap directly above the junction line on the top of these magnets. The gain by doing so is twofold. Firstly, the magnitude of the magnetic stray field is increased even further. Secondly, the width of the peak in the magnetic stray field extends a distance comparable to the gap size. Consequently, as the gap size decreases, the gradient of the stray field increases by orders of magnitude. The device, as a result, produces extremely intense magnetic forces with short ranged action, with possible applications in electronics, metallurgy, chemistry and biology.

Applications in magnetophoresis are of particular interest. The magnetic force on any magnetic or non-magnetic particle is proportional to its susceptibility (χ), the magnetic induction ($\mathbf{B}$), and the gradient of the applied field ($\nabla\mathbf{B}$). The intense magnetic forces can be used to separate weak paramagnetic substances from diamagnetic substances according to their susceptibility. One application concerns the separation of red blood cells, differentiating between oxyhemoglobin (diamagnetic) and deoxyhemoglobin (paramagnetic) saturated cells [1, 2].

Additionally, the device is proposed acting as a recording head, able to magnetize high coercivity storage media ($H_c = 0.35 - 1.15$ MA/m). This type of storage media will increase density, reliability, and lifetime of recording information considerably compared to today's standards [3].

1.2 Problem description

The main objectives in this thesis concern the generation of a simulation environment completely describing the behavior of the invention [4], aiming to define an optimal configuration of mask thickness, gap size, soft magnetic material in masks and permanent magnet material in magnets, in order to maximize $\mathbf{B}\nabla\mathbf{B}$. Secondly, simulations of the invention performed by Il'yashenko *et al.* [5] are investigated. Moreover, the theoretical approximations to a half open Kittel domain, derived by Samofalov *et al.* [6], forming the basis of the invention, are numerically studied. Finally, experiments where the magnetic stray field is measured on a model of the invention, aim to verify theory and simulations.

The objectives are as following:

- Numerically investigate the theoretical approximations describing the basis of the invention.
- Generate a simulation environment completely describing the invention.
- Investigate simulation results obtained for the invention.
- Perform experimental measurements on a model of the invention.
- Compare theory and simulations with experiments.

1.3 Disposition of the dissertation

Chapter 1 briefly discusses background work, problem description and methods, as well as incentives for carrying out the assignment.

Chapter 2 covers a theoretical introduction to magnetism, ending up formulating all the basic differential equations needed to define and solve any magnetostatic problem.

Chapter 3 gives a theoretical description of a half open Kittel domain, forming the basis of the invention as well as a detailed description of the device itself. Additionally, this chapter defines the basics needed to operate within MagNet's simulation environment, a professional finite element analysis program.

Chapter 4 presents all results and discussions concerning the simulations of half open Kittel domains and the device, including mask thickness, gap size, soft magnetic material, and permanent magnet material comparisons.

Chapter 5 investigates experimental results obtained from measuring the magnetic stray field on a model of the invention using semiconductor Hall effect sensors. Lastly, theory and simulations are compared to the experiments.

Chapter 6 theoretically studies the force on objects, moving in hydrodynamic fluid flows under the influence of externally applied magnetic fields. Different magnetophoresis methods operating on microfluidic scales are presented, and includes high-gradient magnetic separation techniques like field-flow fractionation (FFF), split-flow fractionation (SPLITT), and on-chip free-flow magnetophoresis.

Chapter 7 summarizes results and discussions concerning the invention as well as outlining what future work should focus on.

Chapter 2

Magnetostatics

The quantitative and qualitative importance of the key elements in the device, as well as the correlations between them, are studied in detail through finite element analysis (FEA). The basis of any magnetostatic problem is a set of partial differential equations (PDE), which the FEA method is particularly robust at solving. Having a firm grasp of the principle physical laws concerning these equations is essential, in order to understand how these problems are solved. The most important aspects of magnetostatics are thus covered in this chapter.

2.1 Magnetic flux density B

In classical electromagnetism the magnetic vector potential (**A**) in units of Weber per meter provides a mathematical way to define a magnetic field (**B**) in units of Weber per square meter, through magnetic field lines. It is analogous to the electric potential, which defines the electric field in electrostatics. The field lines, however, are not directly observable. Only the magnetic field they describe may be measured.

A field line is a locus[1]. It is defined by a vector field and a starting location within the field. A vector field defines a direction at all points in space; a field line may be constructed by tracing a path in the direction of the vector field. More precisely, the tangent line to the path at each point is required to be parallel to the vector field at the same point. In other words, these field lines are space-curves $\mathbf{r}(\ell)$, tangential to the local magnetic field vector $\mathbf{B}(\mathbf{x})$ which satisfy the differential equation

$$\frac{d\mathbf{r}}{d\ell} = \frac{\mathbf{B}(\mathbf{r}(\ell))}{|\mathbf{B}(\mathbf{r}(\ell))|}. \tag{2.1}$$

This definition yields $|d\mathbf{r}/d\ell = 1|$, demonstrating that the parameter ℓ is the arc-length along the field line, measured forward in the direction of the vector from point $\mathbf{r}(0)$ [7].

A complete description of the geometry of all the field lines of a vector field is sufficient, to completely specify the direction of the vector field everywhere. In order to depict the magnitude, a selection of field lines is drawn in such a way that, the

---

[1] In mathematics, a locus is a collection of points which share a property.

density of field lines at any location is proportional to the magnitude of the vector field at the same point.

Gauss's law for magnetism states that the magnetic field has divergence equal to zero [8]. Hence, it is a solenoidal vector field. A physical interpretation of this statement is that magnetic monopoles can not exist, and thus the field lines form closed loops. Using Helmholtz decomposition theorem [9, 10], Gauss's law for magnetism implies the existence of a vector potential such that $\nabla \times \mathbf{A} = \mathbf{B}$. Note that there is more than one possible $\mathbf{A}$ satisfying this equation for a given $\mathbf{B}$. As a matter of fact there are infinitely many. The magnetic field is thus invariant under transformation of any field on the form $\nabla\phi$, yielding $\nabla \times \mathbf{A} = \nabla \times (\mathbf{A} + \nabla\phi)$. This transformation is known as a gauge transformation, and the usual gauge for $\mathbf{A}$ in magnetostatics is $\nabla \cdot \mathbf{A} = 0$, known as the Coulomb gauge.

In general circumstances, the only way to find a field line is to integrate Equation 2.1. A useful shortcut is available, however, in cases with one symmetry dimension. In these special circumstances a general magnetic field satisfying $\nabla \cdot \mathbf{B} = 0$ can be written in terms of a scalar function called the flux function ($A(x, y)$), and an arbitrary component in the ignorable direction, both depending only on two coordinates. When z is the ignorable coordinate, the expression is $B(x, y) = \nabla A(x, y) \times \mathbf{z} + B(x, y)\mathbf{z}$, where the flux function is the z-component of the magnetic vector potential. The flux function then has the useful property of being constant along field lines since its derivative $dA(x, y)/d\ell = |\mathbf{B}^{-1}|\mathbf{B} \cdot \nabla A(x, y) = 0$. A selection of field lines is thus easily drawn for two-dimensional models by contouring the flux function.

Although the magnetic field is an abstract concept, the effects of $\mathbf{B}$ are concrete and physical. Figure 2.1 shows the field lines around two permanent magnets in the vicinity of a steel bar. In simplified terms, the field lines can be treated as elastic bands pulling the bar towards the magnets.

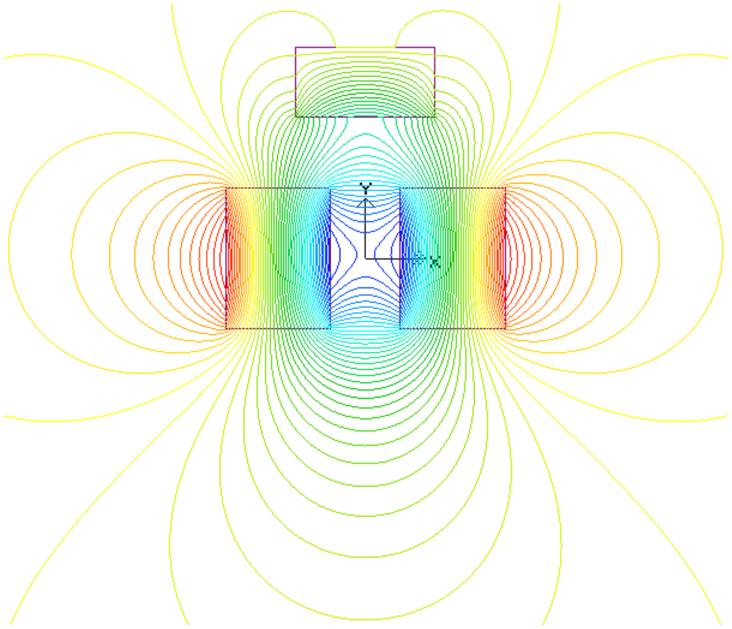

Figure 2.1: *Magnetic field lines around two permanent magnets with opposite directions of magnetization along the y-axis, in the vicinity of a rectangular steel bar.*

Another direct physical interpretation of **B** is given by the Lorentz equation. The magnetic force on an electric charge (q) moving with velocity $\mathbf{u}$ is $\mathbf{F}_{mag} = q\mathbf{u} \times \mathbf{B}$. This means that, the force on a charge moving in a magnetic field is always perpendicular to the magnetic field.

2.2 Magnetic field strength H

Electric currents give rise to magnetic fields. The currents may flow in conductors or coils or may take the form of currents produced by electron magnetic dipole moments in the atoms of a magnetic material. In either case the problem is to define the relationship between the magnetic field described by **B**, and the currents which are the source of the field. In seeking a mathematical form for this relationship that can be used to solve practical problems, it is useful to introduce a new magnetic quantity **H**, which is related both to **B** and to the currents that are the source of **B**. For a magnetic field in free space, set up by currents flowing in conductors, **H** is defined through the equation $\mathbf{B} = \mu_0 \mathbf{H}$ with units of Amperes per meter. The relationship between **H** and the currents is then given by Ampere's circuital law

$$\oint \mathbf{H} dS = I_{enc}, \tag{2.2}$$

where the integral on the left is taken round a closed path, and I_{enc} is the net free current that penetrates through the surface S. This equation makes it easy to calculate the field of a simple system such as a long straight conductor or a toroidal coil, and is the basis of the magnetic circuit concept, widely used for approximate calculations in electromagnetic devices. When magnetic materials are present, however, the situation is completely different.

2.3 Magnetic materials

Magnetic fields are typically conceptualized with so-called field lines. When such field lines encounter any sort of matter an interaction takes place, in which the number of lines is either increased or decreased. The original magnetic field therefore becomes amplified or diminished in the body of matter as a result of the interaction. This is true whether the matter is a typical magnetic material like iron or nickel, or a so-called non-magnetic material like copper or air.

Different substances possess varying degrees of magnetization. The aforementioned examples of strongly magnetic materials have the ability to strengthen an applied magnetic field by a factor of several thousand. Such highly magnetizable materials are called ferromagnetic. Certain other substances, like aluminium, only marginally increase an applied magnetic field. Such weakly magnetizable materials are called paramagnetic. Still other substances, like copper and the rare gases, slightly weaken an applied magnetic field. Such opposing magnetizable substances are called diamagnetic. However, as shown by Figure 2.2, all substances are magnetic to some extent. Only empty space is truly non-magnetic.

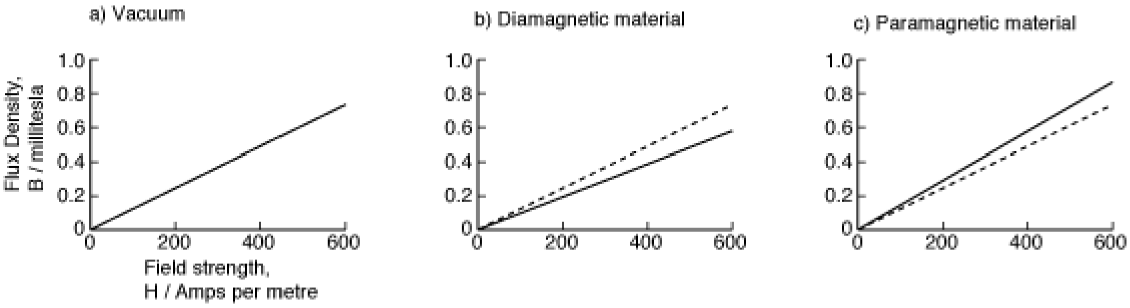

Figure 2.2: *The degree of magnetization in truly non-magnetic (a), diamagnetic (b) and paramagnetic materials (c). The dotted line in figure b and c corresponds to the solid line in figure a, i.e., an unperturbed magnetic field.*

The magnetic permeability of a substance is a numerical description of the extent to which that substance interacts with an applied magnetic field. Let an externally applied field be described by the vector quantity **H**. On passing through a body of interest, **H** magnetizes the body to a degree **M**, formally defined as the magnetic moment per unit volume. The units of **M** are usually Ampere per meter. The combined effects of the applied field and the magnetization of the bodies, the sum total flux per unit area or flux density is $\mathbf{B} = \mu_0(\mathbf{H}+\mathbf{M})$, where μ_0 is the permeability of free space equal to $4\pi \times 10^{-7}$ Henry per meter. In itself, the magnetization is unimportant. What matters is the relationship between **H** and the resultant **B**. This relationship can be extremely complex. The vectors may not be in the same direction, and the present value of **B** may depend on the past history, as well as the present value of **H**. For many practical purposes, however, these complexities can be ignored.

The absolute permeability (μ) of a magnetized body is defined as, the induction achieved for a given strength of applied field, i.e., $\mu = \mathbf{B}/\mathbf{H}$. Often, the absolute permeability is normalized by μ_0 to result in the relative permeability $\mu_r = \mu/\mu_0$. Figure 2.3 shows how the absolute permeability and flux density of a typical soft magnetic material varies with an externally applied field.

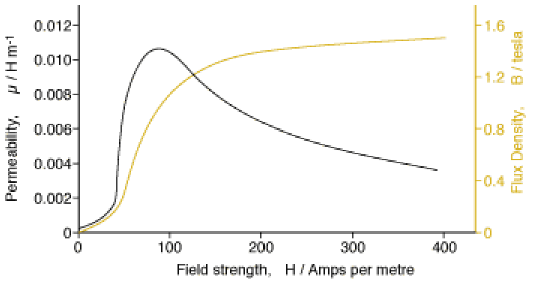

Figure 2.3: *Magnetic permeability (black) and flux density (yellow) in a typical soft magnetic material, varying with an externally applied field.*

The amount by which the relative permeability differs from unity is called the volume magnetic susceptibility, often called the intrinsic permeability, denoted χ_v such that $\chi_v = \mu_r - 1 = \mathbf{M}/\mathbf{H}$. Both χ_v and μ_r are dimensionless quantities. The volume magnetic susceptibility is easily converted to mass and molar susceptibilities, in cases where this is needed.

Moreover, all substances fall into one of three magnetic groups according to their magnetic susceptibility. The three groups include diamagnetic, paramagnetic, and ferromagnetic materials, with ferromagnetic as a subclass of the paramagnetic group. Two other important subclasses of the paramagnetic group, ferrimagnetic, and anti-ferromagnetic materials, are not included here. Additional discussions of these subclasses can be found in [11].

2.3.1 Diamagnetic materials

In any atom, the orbiting and spinning electrons behave like tiny current loops. As with any charge in motion, a magnetic moment is associated with each electron. The strength of the moment is typically expressed in units of Bohr magnetons.

Diamagnetism represents the special case in which the moments contributed by all electrons cancel, and the atom as a whole possesses a net zero magnetic moment. An applied field, however, can induce a moment in the diamagnetic material, where the induced moment opposes the applied field. The magnetization ($\mathbf{M}$) induced in the substance is therefore anti-parallel to the applied field ($\mathbf{H}$), and diamagnetic materials have relatively small negative values of χ_v since $\mu_r \lesssim 1$. Superconductors may be considered to be perfect diamagnets with $\chi_v = -1$, since they expel all fields from their interior, due to the Meissner effect. In other words, diamagnetic materials are repelled from magnetic fields, and forced towards minima of magnetic field strength. Because of this they are often referred to as non-magnetic.

Most materials are weakly diamagnetic, including gold, water, wood, glass, polymers, proteins, cells and DNA.

2.3.2 Paramagnetic materials

In a paramagnetic substance the individual electronic moments do not cancel, and the atom possesses a net non-zero moment. In an applied field, the weak diamagnetic response is dominated by the atoms tendency to align their moments parallel with the applied field direction. The materials experience a small force towards magnetic field maxima, i.e., they are attracted to magnetic fields.

Paramagnetic materials have relatively small positive values for χ_v since $\mu_r \gtrsim 1$. Thermal energy, however, retards a paramagnet's ability to align with an applied field. Over a considerable range of applied field and temperature, the paramagnetic susceptibility is constant. However, with very high applied fields and low temperatures, a paramagnetic material can be made to approach saturation, which means the condition of complete alignment with the field. Examples of paramagnetic materials include oxygen and platinum.

2.3.3 Ferromagnetic materials

Ferromagnetic substances are actually a subclass of paramagnetic substances. In both cases the individual electronic moments do not cancel, and the atom has a net non-zero magnetic moment, that tends to align itself parallel to an applied field.

However, a ferromagnet is much less affected by the randomizing action of thermal energy compared to a paramagnet. This is because the individual atomic moments of a ferromagnet are coupled in rigid parallelism, even in the absence of an applied magnetic field.

Ferromagnetic materials like iron, cobalt and nickel have $\chi \gg 0$ since $\mu_r \gg 1$, and are strongly attracted to magnetic fields. Another special case of paramagnetism is superparamagnetism. Superparamagnetic particles have a core of small iron oxide crystals encased by a polymer shell. The particles are magnetised in a magnetic field. However, they have no magnetic memory. Once the external field is removed, the particles redisperse and behave like a non-magnetic material.

With no applied field, a demagnetized ferromagnet is comprised of several magnetic domains. Within each domain, the individual atomic moments are parallel to one another or coupled, and the domain has a net non-zero magnetization. However, the direction of this magnetization is generally opposed by a neighbourring domain. The vector sum of all magnetizations among the domains is zero. This condition is called the state of spontaneous magnetization.

With an increasing applied field, domains with favourable magnetization directions relative to the applied field direction, grow at the expense of the less favourably oriented domains. The exchange forces responsible for the ferromagnetic coupling are explained by Heisenberg's quantum mechanical model [12]. However, above a critical temperature known as the Curie point, the exchange forces disappear and the formerly ferromagnetic material behaves exactly like a paramagnet.

2.3.3.1 Hysteresis in ferromagnetic materials

When a ferromagnetic material is magnetized in one direction, it will not relax back to zero magnetization when the imposed magnetizing field is removed. If an alternating magnetic field is applied to the material, its magnetization will trace out a path called a hysteresis loop. The term hysteresis has been used to describe many instances where an effect lags behind the cause. However, Ewing was apparently the first to use the term in science, when he applied it to the particular magnetic phenomenon displayed by ferromagnetic materials [11]. Magnetic hysteresis occurs during the cyclical magnetization of a ferromagnet, as seen in Figure 2.4.

The magnetization path created, while increasing an externally applied field, is not retraced on subsequent decrease and even the reversal of the field. Some magnetization, known as remanence, remains in the material after the external field has been removed. Some compositions of ferromagnetic materials will retain an imposed magnetization indefinitely, and as a consequence useful as permanent magnets.

During magnetization, ferromagnetic materials show very different characteristics from diamagnetic and paramagnetic materials. The dotted line in the first quadrant in Figure 2.4 shows an initial magnetization curve for a typical ferromagnetic material. Note that $\mathbf{M}$ is not linear with $\mathbf{H}$, except in the very low and very high-field regions. Because of this, the permeability μ for ferromagnetic materials must always be specified at a certain applied field. Note that μ is the slope of the line, connecting a point of interest on the magnetization curve to the origin. It is not the slope of the curve itself, although this value $d\mathbf{M}/d\mathbf{H}$ is called the differential permeability.

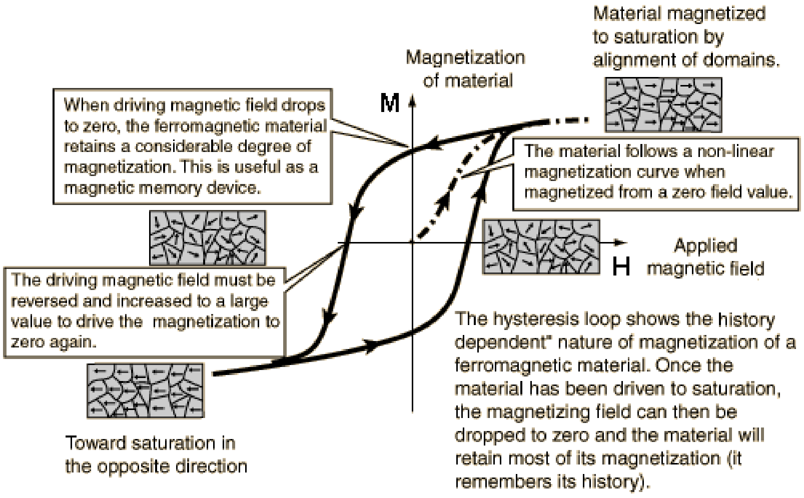

Figure 2.4: *The magnetization in a ferromagnetic material traces out a loop called a hysteresis, when subjected to an alternating externally applied magnetic field.*

Another ferromagnetic characteristic evident in Figure 2.4 is saturation. Once the applied field has exceeded a certain but relatively low value, the slope of the magnetization curve assumes a constant value of unity. At this point the induced magnetization in the material has reached a maximum value, and the material is said to be saturated. For all practical purposes, all magnetic moments in the ferromagnetic material are aligned with the applied field at saturation. This maximum magnetization is often called the saturation induction (B_s) [13]. Note, that B_s is an intrinsic property, and does not include the applied field in its value. This characteristic is typical for ferromagnetic materials, like iron, nickel, cobalt, manganese and their alloys.

The ferromagnetic materials can be divided into two main categories, hard and soft magnetic materials, as shown by Figure 2.5.

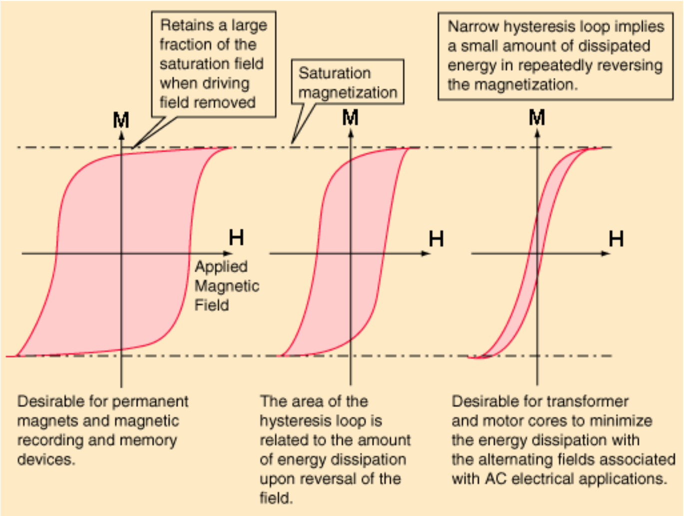

Figure 2.5: *Comparison of hysteresis loops for hard magnetic (left), and soft magnetic (right) materials.*

Soft magnetic materials includes a wide variety of compounds. In a material such as transformer steel, the magnetization virtually disappears when the external field is removed. As a consequence, the magnetization curve almost passes through the origin. For these materials it is convenient to express the magnetic induction as $\mathbf{B} = \mu_0\mu_r\mathbf{H}$. Typically μ_r is not constant but varies with $\mathbf{H}$. It has an initial value of several thousand, but may fall well below 100 in the saturation region.

Permanent magnets are hard magnetic materials, which have the property that some magnetization remains in the material when the external field is removed. For these materials, the important part of the magnetization curve lies in the second quadrant, known as the demagnetization characteristic. Permanent magnet materials have two distinctive parameters: the remanence ($\mathbf{B}_r$) is the magnetization remaining in the material when the applied field is zero, and the coercivity ($\mathbf{H}_c$) is the negative value of $\mathbf{H}$ that must be applied to reduce the magnetization to zero.

Some permanent magnet materials like samarium-cobalt or neodymium-iron-boron, have magnetization curves which are virtually straight lines from $(0,\mathbf{B}_r)$ to $(-\mathbf{H}_c,0)$. These materials are treated as linear, with a constant relative permeability μ_r specified by $\mathbf{B}_r$ and $\mathbf{H}_c$.

2.4 Magnetostatics formulation

The following set of SI unit equations covers the fundamental physicial laws, used for solving the differential equations of magnetostatic problems in numerical analysis [14].

From Maxwell's equations for static magnetic fields, the field intensity ($\mathbf{H}$), flux density ($\mathbf{B}$), and current density ($\mathbf{J}$) must obey

$$\nabla \times \mathbf{H} = \mathbf{J} \tag{2.3}$$

$$\nabla \cdot \mathbf{B} = 0 \tag{2.4}$$

$$\nabla \cdot \mathbf{J} = 0. \tag{2.5}$$

For non-magnetic and soft magnetic materials the relationship

$$\mathbf{B} = \mu\mathbf{H} \tag{2.6}$$

holds true, while for hard magnetic materials like permanent magnets

$$\mathbf{B} = \mu(\mathbf{H} + \mathbf{H}_c), \tag{2.7}$$

where $\mathbf{H}_c$ is the coercive field intensity of the magnet. For isotropic materials the magnetic permeability is

$$\mu = \mu_0\mu_r, \tag{2.8}$$

where $\mu_0 = 4\pi 10^{-7}$ Hm^{-1}, and μ_r is the relative permeability. If the material is non-linear, μ is a function of $\mathbf{B}$, otherwise it is constant.

Maxwell's equations requires that the tangential components of **H** and normal components of **B** have to be continuous across any material interface, thus

$$\mathbf{n} \times \mathbf{H}_1 = \mathbf{n} \times \mathbf{H}_2 \tag{2.9}$$

$$\mathbf{n} \cdot \mathbf{B}_1 = \mathbf{n} \cdot \mathbf{B}_2. \tag{2.10}$$

The finite element method used by most FEA programs has a single value of each variable on an interface, and therefore requires that the quantities chosen for system variables must be continuous across the interface. However, in the general case, meeting the continuity requirements can be impossible.

Instead of using field quantities, any field that satisfy the above equations can be calculated via the magnetic vector potential using the expression

$$\mathbf{B} = \nabla \times \mathbf{A}, \tag{2.11}$$

which always enforces 2.4. Furthermore, **A** can be shown to be continuous everywhere in the domain, and represents the condition of 2.9 and 2.10 correctly.

The magnetic vector potential can be derived from Ampere's law in Equation 2.2, and shown to be the integrated effect at each point of all the current loops active in the domain. In this derivation **A** has components parallel to the components of **J**, thus it can be determined a priori which components of **A** must be represented.

Equation 2.11 alone is not sufficient to uniquely define **A**. It must be supplemented by a gauge definition of $\nabla \cdot \mathbf{A}$ to be unique, usually taken as the Coulomb gauge $\nabla \cdot \mathbf{A} = 0$, a definition consistent with the derivation of **A** from Ampere's Law. It is not important what the gauge condition is, in all cases $\nabla \times \mathbf{A}$ and therefore the field quantities, remain the same.

For every point of a computational domain, except those inside permanent magnets, the combination of Equation 2.3, 2.6 and 2.11 implies

$$\nabla \times (\frac{1}{\mu} \nabla \times \mathbf{A}) = \mathbf{J}, \tag{2.12}$$

whereas for points inside permanent magnets the corresponding expression resultant from Equation 2.3, 2.7 and 2.11 is

$$\nabla \times (\frac{1}{\mu} \nabla \times \mathbf{A} - \mathbf{H}_c) = \mathbf{J}. \tag{2.13}$$

Equation 2.13 is valid for every point in a computational domain and for all materials, since it incorporates Equation 2.12 for space regions outside permanent magnets by simply setting $\mathbf{H}_c = 0$. Thus, the advantage of using vector potential formulation is that Equation 2.3-2.7, forming the mathematical model of the problem, have been combined into a single equation.

Applying the curl theorem

$$\int\int\int_V \nabla \times \mathbf{F} dV = \oint\oint_S (\mathbf{n} \times \mathbf{F}) dS \tag{2.14}$$

on Equation 2.12 results in

$$\int\int\int_V \nabla \times \big((\nabla \times \mathbf{A})/\mu\big) dV = \int\int\int_V \nabla \times \mathbf{H} dV = \oint\oint_S \mathbf{n} \times \mathbf{H} dS. \qquad (2.15)$$

The natural boundary condition thus defines $\mathbf{n} \times \mathbf{H}$ on external boundaries, and $\mathbf{n} \times \mathbf{H}$ is assumed continuous across internal boundaries, consistent with Maxwell's equations.

In the general three-dimensional case, $\mathbf{J}$ and $\mathbf{A}$ are vectors with tree components each. In the two-dimensional case, however, the magnetic vector potential has some very useful properties. For the xy-plane of translational geometry, the current and therefore the vector potential, is in the z-direction. The components of $\mathbf{B}$ are thus given by

$$B_x = \frac{\partial A_z}{\partial y}, B_y = \frac{-\partial A_z}{\partial x}. \qquad (2.16)$$

From equation 2.16, it may be shown that equipotentials which are lines of constant A_z are field lines. Thus, if $\mathbf{A}$ is found, $\mathbf{B}$ and $\mathbf{H}$ can be deduced from 2.11 and 2.6 or 2.7, respectively.

2.5 Summary and discussion

The differential equations, derived from Maxwell's fundamental magnetostatic equations, are sufficient to establish a numerical analysis tool for solving almost any 2D magnetostatic problem. With the theoretical foundation now at hand it is time to look at the environment in which these equations are applied. The degree to which the equations give accurate answers depends heavily on the geometry, dimensionality, and material properties of the magnetostatic structure. A detailed theoretical description of the basis of the invention as well as a qualitative description of the invention itself, coupled with a thorough discussion of a finite element analysis program called MagNet, is thus covered in the next chapter.

Chapter 3

Simulation environment

This chapter describes the half open Kittel domain forming the basis of the invention, as well as all the key factors of the invention itself. Furthermore, the magnetostatic differential equations established in Chapter 1 are solved using FEA in MagNet, and the simulation parameters in this environment are thoroughly discussed. FEA methods are powerful techniques and accurate tools, even when studying structures whose components are very small, or when dealing with very weak or strong forces. Complex domains, problems where the desired precision varies across the system, or regions where the solution lacks smoothness, are handled particularly well. This is promising, since the system in question shows important and interesting characteristics, dealing with extremely intense magnetic forces with short range action, typical on the order of 10^8-10^{11} mT^2/m in a 10-100 μm range.

3.1 Kittel domain - the basis of the invention

Magnetic and non-magnetic particle separation in conventional magnetophoresis is an area, mainly dominated by strong magnetic fields produced by cooled solenoids, electromagnets, and superconducting magnets. Recently, however, the literature reports about *permanent magnet* systems, able to produce strong magnetic stray fields reaching field values of up to 5T [15, 16], produced in closed systems formed as a type of Halbach cylinder [17, 18, 19]. These strong fields are possible due to the discovery of giant magnetic anisotropy[1] permanent magnets based on rare-earth elements [20]. It is reported, however, that the fields are uniform and as such not interesting, since magnetic separation of any practical use requires sources which produce *strong*, but also *high-gradient* magnetic fields. The magnetic force, that acts on a magnetic or non-magnetic particle, is proportional to its susceptibility (χ), the magnetic induction ($\mathbf{B}$), and the gradient of the applied field ($\nabla\mathbf{B}$), i.e., $\mathbf{F} \propto \chi\mathbf{B}\nabla\mathbf{B}$ [21]. Thus, to increase the sensitivity of magnetic separation, the highest possible value of $\mathbf{B}\nabla\mathbf{B}$ is required.

---

[1] A magnetic anisotropic material will align its moment to an easy axis of magnetization. Orienting the magnetic direction in the direction of the easy axis, optimizes the magnetic induction behavior outside the magnet in the pole environment, and makes it possible to achieve the maximum value of remanence, and energy product for the given material.

3.1.1 Theoretical approximations

Figure 3.1 shows the half open Kittel domain considered by Samofalov *et al.* in [3, 6]. The structure consists of two adjoined giant magnetic anisotropy rare-earth magnets with opposite directions of magnetization, placed on top of a yoke made of a soft magnetic material.

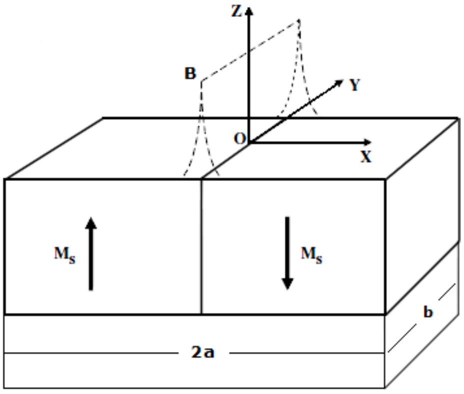

Figure 3.1: *Schematic of a half open Kittel domain structure. Two permanent magnets with opposite directions of magnetization (*$\boldsymbol{M}_s$*) are joined together, enforcing a strong, and inhomogeneous magnetic stray field (*$\boldsymbol{B}$*) noted by a dotted line in the figure. The yoke in the structure eliminates magnetic charges of opposite signs on the bottom poles of the magnets, thus increasing the stray field over the upper plane of the structure. For future references, O is understood as the point where* $x, y, z \to 0$.

A strong magnetic stray field is produced in a small volume in the vicinity of the junction line in the zone of the upper edges of the joining magnet faces, where a step-wise change of poles take place. The $B_x(x,z)$ and $B_z(x,z)$ component of the stray field are described by the following expressions in SI units, derived by Samofalov *et al.* [6]:

$$B_x(x,z) = M_s\frac{\mu_0}{4\pi}[\ln(a^2-2ax+x^2+z^2)-2\ln(x^2+z^2)+\ln(a^2+2ax+x^2+z^2)] \quad (3.1)$$

$$B_z(x,z) = M_s\frac{\mu_0}{4\pi}\big(\arctan(\frac{a+x}{z})-\arctan(\frac{a-x}{z})-2\arctan(\frac{x}{z})\big), \quad (3.2)$$

where $M_s = B_r/\mu$, and a is the size of the magnets along the x-axis. The expressions are derived for a structure where $b \gg a$, but are valid even when $b \approx a$. The latter case, however, overestimates the stray field with a factor of 10-15%, but only in the immediate vicinity of O. Additionally, the expressions are derived for a structure *without* a yoke, consequently the expressions do not describe the complete picture of the magnetic stray field above the magnets for a structure *with* yoke, only the field close to point O.

In a small area $-0.1a \leq x \leq 0.1a$ around point O, the magnetic stray field makes an abrupt jump, increasing in magnitude as $z \to 0$, noted by a dotted line in Figure 3.1. The strength of the components of this field are found calculating the gradient of the potential, and in this region the intensity of the tangential component ($B_x(x,z)$)

reaches values, several times stronger than the induction of the magnet material itself. The maximum value of Equation 3.2 is less than $B_r/2 \approx M_s\mu/2$, thus the normal component ($B_z(x,z)$) comprises less than half the value of the induction of the magnet material. Finally, owing to the geometry of the system, $B_y(x,z) \approx 0$, and thus ignored. As a result, the magnitude of the magnetic stray field is described by $B_{st} = (B_x^2 + B_z^2)^{1/2}$.

The magnets must be highly anisotropic, and the reason is connected to the value of the demagnetization field (B_d) penetrating inside the domain body, corresponding to the considered stray field (B_{st}) over the domain. The uniaxial anisotropy field of the ferromagnet is given as $B_K = 2K/M_s$, where K is the anisotropy constant. If $B_K \gg B_r$, then B_d does not produce substantial deflection of magnetization from the easy axis.

In uniaxial ferromagnets with large but finite values of the anisotropy field, where $B_K \approx B_r$, then B_d can produce deflection of the magnetization vector from the easy axis, and will favour the closure of the magnetic flux in the subsurface layer, i.e., the magnetization distribution will be inhomogeneous in the domains of the surface similar to a transition layer called a Bloch wall[2] [12]. This inhomogeneous distribution leads to formation of closed domains, and the half open one-dimensional Kittel domain structure does not exist in plates with relatively low anisotropy, as a result of this. In order for highest possible field values, the magnets must therefore be made of materials with much greater magnetic anisotropy than the induction of the material itself, such as neodymium-iron-boron, iron-platinum, or samarium-cobalt permanent magnets.

Figure 3.2 shows the field lines around an open and a half open Kittel domain. The yoke in the half open domain prevents flux from escaping, pushing it back into the magnets, thus increasing the magnetic stray field over the upper plane of the structure.

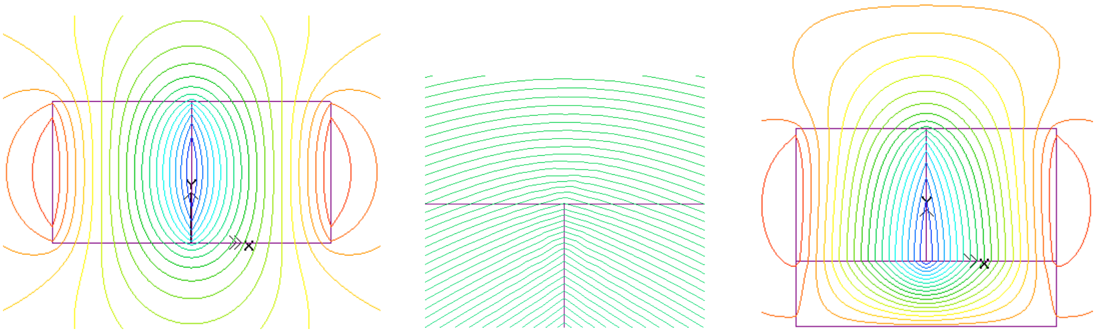

Figure 3.2: *Field lines around an open Kittel domain (left), and a half open Kittel domain (right). The middle picture shows the field lines in a half open domain, zoomed in on the top junction between the magnets.*

The important practical feature of the magnetic system described is the fact that, the magnetic stray field possesses an extremely high gradient, which in the area near

---

[2] A Bloch wall is a narrow transition region at the boundary between magnetic domains, over which the magnetization changes from its value in one domain to that in the next. The magnetization rotates through the plane of the wall unlike the Néel wall, where the magnetization rotates in the plane of the wall.

point O depending on distance to the surface, reaches theoretical values of 10^5-10^7 mT/m, while the product $\mathbf{B}\nabla\mathbf{B}$ reaches theoretical values of 10^8-10^{10} mT^2/m. A huge disadvantage with this design, however, is the near impossible task of controlling the shape and strength of the magnetic stray field, which in turn makes magnetic separation less accurate, as well as more difficult.

3.2 Inventive device

In order to establish control over the strength and shape of the magnetic stray field, thus control of the gradient, a high-gradient magnetic field device, for separation of substances, is suggested by Il'yashenko *et al.* [4, 5].

The device, as seen in Figure 3.3, is based on a half open Kittel domain structure, and is embodied in the form of two rectangular shaped magnets (1, 2) of constant magnetization ($\mathbf{M}_s$), joined together by the side faces (3, junction line). They have polarities oppositely directed, and with greater magnetic anisotropy than the induction of the magnet material. The magnets are mounted on top of a common base (4, yoke), made of a non-retentive material. Two thin plates (5, 6, masks), also made of a non-retentive material, are placed on the top faces of the magnets, forming a gap (7) arranged above the top edges of the magnets adjoined faces. Two devices (8, 9) are mounted on the left and right side of the magnets, in order to regulate the gap size, while a thin transparent table (10) is used for separating substances (11).

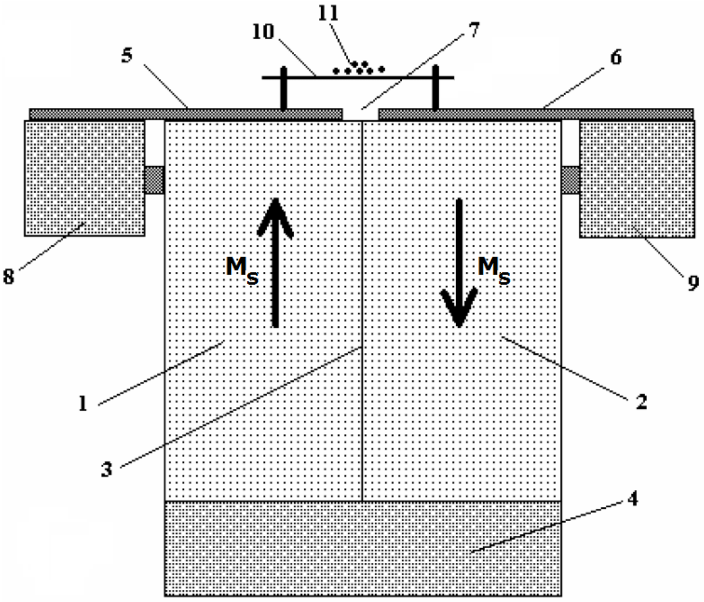

Figure 3.3: *Schematic drawing of a permanent magnet system, designed to produce extremely strong magnetic field gradients.*

The effect of introducing the soft magnetic masks is seen in Figure 3.4. As the field lines "move" from left to right, they are soaked up by the soft magnetic material in the masks, as it is much more permeable than the surrounding air. The mask material is also chosen for its high magnetization saturation, thus, depending on the thickness, preventing most of the flux from escaping beyond the masks. However, once the field lines "reach" the gap, they are "released" into the air. Note that, due to geometry there will be a relative large build-up of flux near the mask corners. In any case, the concept is now that, the second mask located at the other side of the gap "forces" these field lines to abruptly change their direction, in order to get back into a more permeable material. This sudden change of direction over a very small distance comparable to the gap size increases the magnetic gradient, compared to a system without masks. As a result, $\mathbf{B}\nabla\mathbf{B}$ increases.

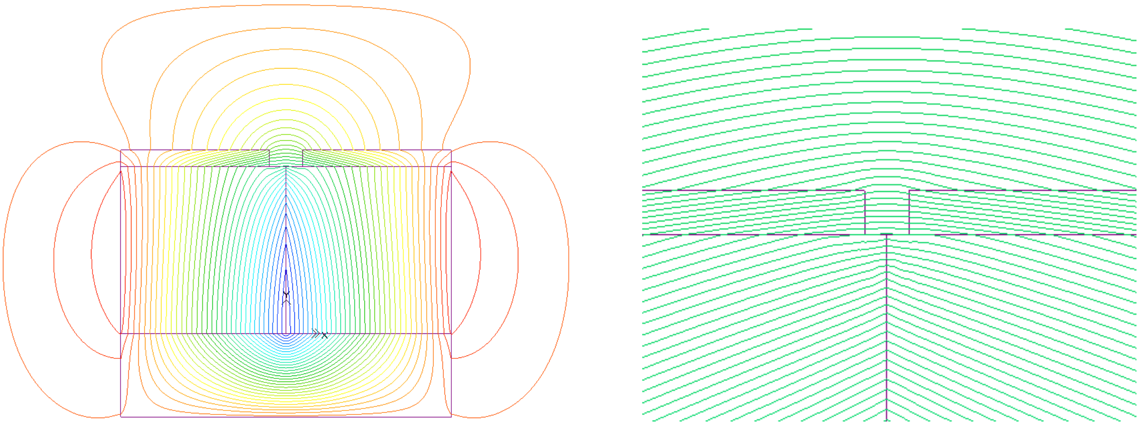

Figure 3.4: *Field lines around a half open Kittel domain with masks. The picture to the right shows field lines in a similar domain, zoomed in on the gap at the top of the magnets junction line.*

3.2.1 Four key factors

Mainly four key factors contribute to altering the strength and shape of the magnetic stray field, and these are comprehensively studied in a numerical environment. The goal is to find an optimal combination, in order to maximize $\mathbf{B}\nabla\mathbf{B}$. The factors include but are not limited to:

- The coercivity of the permanent magnets: the coercivity determines the strength of the magnetic stray field.
- The thickness of the masks: a thick mask prevents leakage of flux and increases saturation volume, however, locates the point of separation further away from the magnet surfaces.
- The size of the gap: the path of the field lines leaking out of one mask, making their way back into the other mask, thus the profile of the stray field distribution is determined by the gap size.
- The soft magnetic material: the basis for choosing a soft magnetic material rests on two criteria, the magnetization saturation, and magnetic permeability of the material. To date the most promising soft magnetic material is vanadium permendur (VFeCo), with saturation levels at room temperature up to 2.5 T.

3.3 Approaching finite element analysis

A handful of different FEA-solvers have been tested at some stage during the simulations. Most of them, however, presents problems including reduced control of mesh structures, restrictions on number of nodes and iterations allowed, lack of non-linear solver options, or to low solution accuracies. Infolytica MagNet on the other hand, excels and proves to be just the solver for the task at hand. This program is fully devoted to solving magnetostatic problems, with built in options for non-linear materials, no restrictions on solution accuracy, mesh structure, model design, number of nodes, or iterations.

- Infolytica MagNet[3]
- FlexPDE 3.0[4]
- Ansoft Maxwell[5]
- LISA[6]
- FEMLAB[7]
- FEMM[8]
- Quickfield[9]

According to J. D. Edwards (2007) in [22]:

> ”MagNet is the most advanced package currently available for modeling electromagnetic devices on a personal computer. It provides a ”virtual laboratory” in which the user can create models from magnetic materials and coils, view displays in the form of field plots and graphs, and get numerical values for quantities such as flux linkage and force.”

The full version core of MagNet offers a powerful technique for numerically solving electromagnetic field equations, and comes with facilities for user-defined adjustment of the model parameters, calculation of further results from the field solution, and control of the operation via scripting forms. It is designed as a full 3D-modeling tool for solving static magnetic field problems, but offers the option of 2D-modeling, with a substantial saving in computing resources and solution time. The version of the software used in this thesis, however, is restricted to two-dimensional static magnetic fields, without scripting options for automatic extraction of solution data.

MagNet employs a finite element method, to solve the 2D form of Equation 2.13 for the magnetic potentials [23]. The region of the problem is divided into a mesh of

---

[3] `http://www.infolytica.com/`

[4] `http://www.pdesolutions.com/`

[5] `http://eetimes.firstlightera.com/EN/Microsites/1/Ansoft/Maxwell.htm`

[6] `http://www.lisa-fet.com/`

[7] `http://www.femlab.com/`

[8] `http://femm.foster-miller.net/wiki/HomePage`

[9] `http://www.quickfield.com/`

triangular elements, and the potential in each element is approximated by a simple function of the x and z coordinates. The simplest function is a linear variation with position. This gives first-order elements, where the potential inside a triangular element is obtained from the potentials at the three vertices, or nodes. High-order elements use higher order polynomials and additional nodes to represent the potential. The problem of solving Equation 2.13 then reduces to the solution of a set of linear equations for the unknown potentials at all the nodes. This is repeated several times if the model contains non-linear magnetic materials.

The accuracy of the finite element solution depends on three factors: the nature of the field, the size of the elements, and the element order. In regions where the direction or magnitude of the field changes rapidly, high accuracy requires small elements, or a high element order. In addition, the methods used to find the finite element solution are iterative, with an adjustable error criterion for terminating the process. The accuracy can be improved by increasing the order of the polynomial, or using smaller elements in critical regions of the model by adjusting the adaption refinement.

With any numerical method, perfect accuracy is not possible. Even with full use of the options for improving the accuracy, the solutions generated by MagNet contain errors. In most cases, these errors are insignificant and likely to be smaller than the changes caused by manufacturing tolerances, or variations in the magnetic properties of the materials. Calculated values for forces, however, are particularly sensitive to errors in the field solution, and are likely to change significantly as the solution accuracy is improved.

Similarly, where quantities are expected to be equal in magnitude, the difference should be a small fraction of the mean magnitude. As a result, the automatic method of refining the mesh may not yield an accurate solution. A typical example is the calculation of forces in a device, where an active air gap is very small compared to the dimensions of adjoining materials. In this region the values may not converge towards a limit when the refinement level is increased. Cases like this require an increase of the subdivision of the mesh structure along the edges in order to increase the accuracy, and poses a small but manageable problem in the device studied in this thesis.

3.4 MagNet solver options

When non-linear magnetic materials are present, the permeability (μ) depends on the local value of $\mathbf{B}$. Equation 2.13 is thus solved as the following in MagNet:

1. Constant values of permeability are chosen for each element, found from the initial slope of the material's magnetization curve.
2. The resultant linear equations are solved numerically for the magnetic potential, using a semi-iterative conjugate gradient method.
3. The flux density values are calculated from the magnetic potential, and the results are used to calculate new values for the element permeabilities.
4. The process is repeated until the permeability values of the elements converge.

This solver routine lists several essential commands for controlling input and output accuracy in the 2D magnetostatic model solved by MagNet:

- Conjugent gradient (CG) steps: At each step in the conjugate gradient process, the change in the solution is monitored. The process continues until the change is less than the CG tolerance.

- Permeability calculation: For 3D problems MagNet gives a choice of the Newton-Raphson method[10], or successive substitution for calculating updated element permeability values. The default Newton-Raphson method normally converges more rapidly, but there can be convergence problems with some material characteristics, in which case the successive substitution method is required. In 2D problems, the Newton-Raphson method is the only available option.

- Newton steps: At each step in the permeability calculation process, the change in the solution is monitored. The process continues either, until the change is less than the Newton tolerance, or until the limit of maximum Newton iterations is reached. Problems where permanent magnet material is in direct contact with non-linear soft magnetic material, where the flux density values are very high, or closed magnetic circuits in iron surrounding a current should run with very low tolerances, and increased numbers of iterations.

- Adaption: This is an automatic process to refine the mesh structure, in order to improve the solution accuracy. For 3D models, there is a choice of two adaption methods: h-type adaption where element sizes are halved, and p-type adaption where the element polynomial order is increased. For 2D models, only h-type adaption is available. A consequence of the finite element approximation to the true field is a discontinuity in the value of $\mathbf{B}$, from one element to the next. MagNet determines which elements to refine, by calculating the discontinuity error values. At each adaption step, elements with the largest error are refined first. The total number of elements, refined at each step, is determined by the percentage of elements to refine option. After each adaption step, the change in the calculated value of stored magnetic energy is monitored. Adaption continues until this change is less than a specified tolerance, or the specified number of steps has been reached. If the quantity of interest is the force rather than an energy related quantity such as inductance, a more accurate solution may be required. The change in the stored magnetic energy may therefore not be a good indicator. In such cases, it is often advantageous to set the tolerance to a very low value, and control the mesh refinement by adjusting the maximum number of adaption steps. The optimum setting can be determined by changing the number of steps, and monitoring the change in the force values.

---

[10] Newton-Raphson method is one of the best methods, for successively finding better approximations to the roots of real valued functions. Starting out with an initial guess, which is reasonably close to the true root, the function is approximated by its tangent line, and the x-intercept of this tangent line is computed. This x-intercept will typically be a better approximation to the root of the function than the original guess, and the method is iterated until the desired solution accuracy is obtained [24].

- Polynomial order: The solver polynomial order setting is useful for initial tests on a complex model, and for 2D models the solver polynomial order option sets the value, which will be used for the entire model. With some models, increasing the polynomial order, is as effective as using adaption to improve the solution accuracy. In most cases, however, good results will be obtained by setting the polynomial order to 2, but special cases requires a high order in conjunction with adaption.

- Control of the mesh structure: MagNet determines the initial mesh structure automatically. However, adaption can be used to refine the mesh, to get an even more accurate starting solution. In cases where this process fails, or gives very long solution times, direct control of the mesh structure is possible by specifying the following quantities: Maximum-element-size determines the maximum element edge length. This can be increased to force adaption, to start with a coarse mesh, or reduced to give a fine mesh. Curvature-refinement-ratio measures the maximum deviation, when a curved part of the model is approximated by the straight-line edge of an element. Curvature-refinement minimum-element-size limits over-discretization of tight curves, when the elements are refined. These properties can be set for the entire model, or on individual components, surfaces, and edges. In addition, the mesh can be controlled by edge subdivision. This feature of MagNet enables the ability to specify the number of segments on a given component edge, line, or arc, when the initial mesh is generated. The subdivisions can be linear, or logarithmic.

- Boundary conditions: To solve the field equations it is necessary to specify what happens to the field beyond the device. Theoretically the field extends to infinity, which implies an open boundary. In 2D models, an artificial boundary takes the form of a closed curve, along which a property of the field is specified. In other words, the field property is the boundary condition. Two kinds of boundary conditions are relatively easily implemented solving the field equations: The Dirichlet and the Neumann boundaries, which are the tangential and normal boundary conditions, respectively. The tangential boundary condition simulates a constant flux over any portion of the boundary, i.e., the entire outer boundary will become a flux line. It is equivalent to putting the model in a cavity of a material with zero permeability, so that no flux can escape from the model. If the boundary is taken sufficiently far away from the components of the model, it is a good approximation to an open boundary. The normal boundary condition, however, simulates the direction of $\mathbf{B}$ at right angles to any portion of the boundary, i.e., the flux lines enter the portion at right angles. If the field normal boundary condition is applied to the entire boundary, the effect is equivalent to putting the model in a cavity of a material with infinite permeability. This has the opposite effect to the flux tangential boundary, drawing flux away from the model, which is a simple way of simulating the effect of a magnetic screen.

3.5 Summary and discussion

A detailed theoretical description of the basis of the invention as well as a qualitative description of the invention itself has been coupled with a thorough discussion of MagNet, a professional finite element analysis program. Seeing how there are four key factors contributing to altering the strength and shape of the magnetic field, it is imperative that the combination of these factors are comprehensively studied, in an array of different configurations. With emphasis on the models and solver routines discussed so far, the next chapter thus deals with simulations of the invention, aiming to find an optimal configuration of the key factors maximizing $\mathbf{B}\nabla\mathbf{B}$.

Chapter 4

Simulation study

The most important task of the simulations is to establish an optimal configuration of mask thickness, gap size, permanent magnet, and soft magnetic material in a structured manner, with emphasis on the model explained in Chapter 3, in order to increase $\mathbf{B}\nabla\mathbf{B}$ as much as possible.

4.1 Modelling the system

MagNet provides an extensible scripting utility tool to automate modelling and solving. Through the use of these scripts, the characteristics of the model, as seen in Figure 4.1, e.g., length scales, materials, boundary conditions, and solver options, are easily changed in a standard text editor.

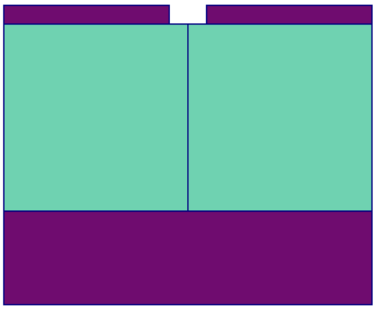

Figure 4.1: *Schematic drawing of a simple model made in MagNet, able to produce a very strong magnetic stray field with extremely strong gradients. Any parameter can easily be changed, using the scripting utility in MagNet, e.g., mask thickness, and gap size, which in this case have been over-exaggerated for better visual effects.*

There are mainly three factors contributing to the complexity of solving the model numerically. Number one is the fact that, two permanent magnets with opposite directions of magnetization are forced together, creating a strong magnetic stray field in the vicinity of their junction line, in the zone of the upper edges of the joining magnet faces. Secondly, the complexity of working with extremely small length scales, e.g., mask thickness, and gap size. Lastly, the problem of having permanent magnet material in direct contact with non-linear soft magnetic material, seriously increasing the difficulty of the permeability calculation process.

Moreover, there are two complications that restricts the solution accuracy even further, not due to complexity in the model itself, but more of a physical nature. Firstly, the amount of physical memory (RAM) available, secondly, the simulation time. The challenging task is to find a good relationship between acceptable simulation times and solution accuracy, not exceeding the RAM limit. In order to do so, careful analysis of a simpler model is carried out where the solver options, as explained in Chapter 3, are appropriately chosen. The presented model is only solved in 2D, due to symmetry in the geometry of the device, with parameters as the following:

- The conjugate gradient step is set with a tolerance of $1{\cdot}10^{-22}$; the program skips to the next step when the solution changes less than this in the course of one iteration.
- A 2D Newton-Raphson method is used for calculating updated element permeability values, with a tolerance level set to $1{\cdot}10^{-15}$.
- To improve the solution accuracy even further, the h-adaption process is used with a 100% refinement of the mesh structure, in conjunction with a tolerance of $5{\cdot}10^{-6}$.
- The model incorporates non-linear materials, hence a non-linear solver routine is chosen.
- A polynomial order of 4 is used; this is a global value that applies throughout the model.
- The option of improving the initial mesh quality before solving is enabled.
- The Dirichlet (flux tangential) boundary condition is used, simulating the model in a cavity of a material with zero permeability, i.e., in an environment where no external magnetic sources interferes with the model.

4.1.1 Materials and configurations

During the simulations, two different soft magnetic and three permanent magnet materials are tested. The permanent magnets are simulated as linear, isotropic materials having real coefficients with a constant magnetization parallel to the z-axis, with parameters as in Table 4.1. The permanent magnet materials neodymium-iron-boron 42H and 50M are simulated with specifications obtained from EastMagnet[1]. The permanent magnet labeled NdFeB "perfect" is at present time not manufacturable, however, is most likely possible to make in the future.

Note that the permanent magnet material of type NdFeB 42H is of particular interest, since the experimental studies are performed on a model currently held at IFE, with specifications similar to this material. The results obtained by Il'yashenko *et al.* [5] are also carried out with permanent magnets similar to NdFeB 42H.

---

[1] Rare-earth permanent magnet manufacturer `http://www.eastmagnets.com/Neodymium_Block_Magnets.htm`

Permanent magnet material

Parameters	NdFeB 42H	NdFeB 50M	"Perfect"
Energy product $(BH)_{max}$ [kJ/m^3]	320	390	n/a
Magnetic remanence B_r [T]	1.32	1.45	2.00
Relative permeability μ_r	1.10	1.10	1.10
Coercivity H_c [kA/m]	955	1033	1455
Dimension [mm^3]	50×50×25	50×50×25	50×50×25

Table 4.1: *Specifications of all know parameters of the permanent magnet materials used in the simulations. The magnet labeled "perfect" is a fictitious NdFeB magnet, while NdFeB 42H and NdFeB 50M are standard rare-earth permanent magnets.*

The soft magnetic materials incorporated in the simulations includes vanadium permendur, and a cold rolled low carbon steel mixture, with a carbon weight[2] between 0.08-0.13%. They are represented by non-linear magnetization curves in Figure 4.2, whose data is listed in Appendix A.1-A.2. The magnetization curve for vanadium permendur is obtained from the materials library in FEMM, while the curve for low carbon steel is found in MagNet. Vanadium permendur is chosen for its high magnetization saturation with $B_s = 2.39$ T. Low carbon steel has a slightly lower saturation with $B_s = 2.22$ T. Alternating between the two materials will provide information about the dependency of the saturation point of the mask material.

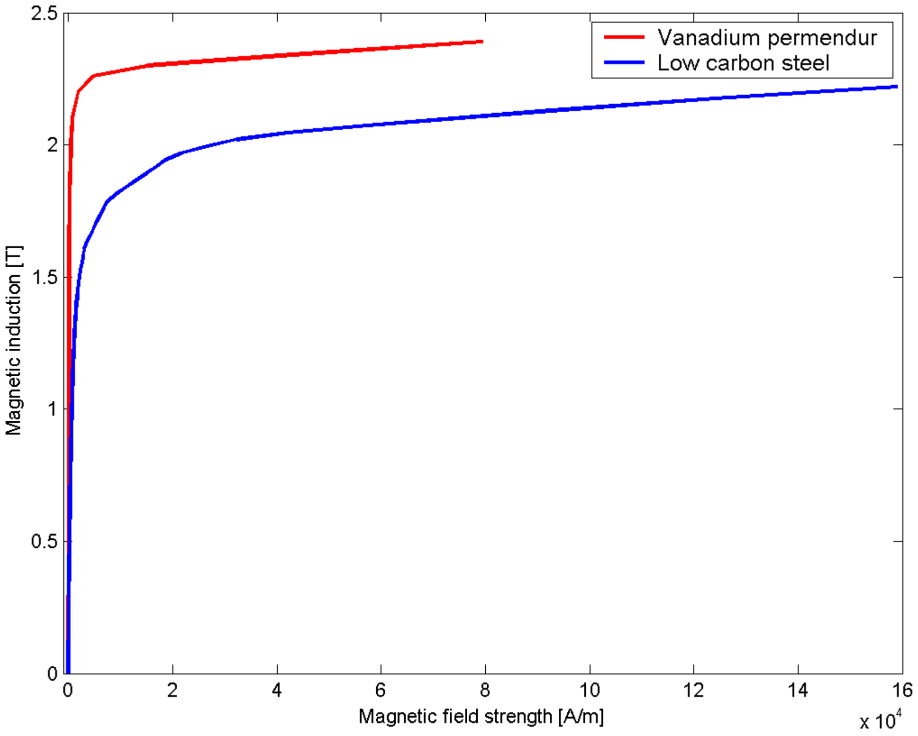

Figure 4.2: *Non-linear magnetization curves of vanadium permendur and low carbon steel, as found in the libraries of FEMM and MagNet, respectively.*

---

[2] `http://www.efunda.com/materials/alloys/carbon_steels/show_carbon.cfm?ID=AISI_1010&prop=all&Page_Title=AISI%201010`

A series of different configurations, cf., Tables 4.2, 4.3 and 4.4, of mask thicknesses, gap sizes, mask and magnet materials are studied. In each case the yoke is 25.0 mm thick, and made of vanadium permendur, while the model is surrounded by air whose relative permeability $\mu_r = 1.00$.

NdFeB 42H

Configurations		Simulation times [$\times 10^4$ s]	
Analog system		0.36	
Mask thickness [mm]	Gap size [mm]	VFeCo mask	Steel mask
0.05	0.05	4.32	14.4
0.05	0.10	1.29	0.69
0.05	0.30	1.86	1.44
0.05	0.50	1.44	1.44
0.05	1.00	1.62	1.26
0.10	0.05	1.20	1.11
0.10	0.10	1.20	0.84
0.30	0.05	1.02	0.60
0.30	0.30	0.42	0.42
0.50	0.05	1.08	0.78
0.50	0.50	1.05	0.81
1.00	0.05	1.14	0.66
1.00	1.00	0.36	0.72

Table 4.2: *Configuration of mask thickness and gap size, with corresponding simulation times in seconds. The permanent magnet NdFeB 42H has a coercivity* H_c = *955 kA/m, relative permeability* μ_r = *1.10, and a magnetic remanence* B_r = *1.32 T. The analog configuration represents a system without masks.*

NdFeB 50M

Configurations		Simulation times [$\times 10^4$ s]	
Analog system		1.62	
Mask thickness [mm]	Gap size [mm]	VFeCo mask	Steel mask
0.05	0.05	4.32	2.76
0.30	0.05	1.44	1.14
0.30	0.30	0.96	1.14

Table 4.3: *Configuration of mask thickness and gap size, with corresponding simulation times in seconds. The permanent magnet NdFeB 50M has a coercivity* H_c = *1033 kA/m, relative permeability* μ_r = *1.10, and a magnetic remanence* B_r = *1.45 T. The analog configuration represents a system without masks.*

NdFeB ”perfect”

Configurations		Simulation times [$\times 10^4$ s]	
Analog system		1.08	
Mask thickness [mm]	Gap size [mm]	VFeCo mask	Steel mask
0.05	0.05	4.14	5.52
0.30	0.05	0.78	0.96
0.30	0.30	0.90	0.78

Table 4.4: *Configuration of mask thickness and gap size, with corresponding simulation times in seconds. The permanent magnet NdFeB ”perfect” has a coercivity* $H_c = 1455$ *kA/m, relative permeability* $\mu_r = 1.10$*, and a magnetic remanence* $B_r = 2.00$ *T. The analog configuration represents a system without masks.*

4.2 Results

The tangential (B_x) and normal (B_z) component are, for several elevations in the magnetic stray field, exported to standard text format files after a successful simulation. The data is then imported to MatLab[3], in order to create graphical representation of both the magnetic field and gradient. Appendix B.1-B.3 contains details of all scripts used in MatLab.

Note, however, there is a small, delicate problem connected to all the results throughout the discussion. It arises from the fact that, MagNet delivers a thousand data points resolution in any elevation plot as long as the mesh structure allows it, i.e, has enough nodes between the end points. The problem then manifests itself by requesting elevation plots between two end points very close together, or very far from each other.

Choosing the points to close to each other can lead to very noisy $\mathbf{B}\nabla\mathbf{B}$ characteristics, and may furthermore produce false results. This is obvious since small irregularities in B_x and B_z, due to mesh grid entangling and discontinuities in values of the magnetic field or permeability, can severely distort the shape and value of the gradient. This problem often occurs where the magnetic field rapidly changes magnitude, or in the transition layer between non-linear and permanent magnets. Choosing the points to far away from each other, and distinct features of $\mathbf{B}\nabla\mathbf{B}$ might disappear as B_x and B_z become more smooth.

Determining just the right distance is critical. Such an assessment is made, and a distance of 20.0 mm between the end points give satisfactory results in most cases, thus used for most elevation plots requested. The graphical representations are in most cases, however, zoomed in on much smaller areas around the center of the gap.

The results of the simulations are split into three categories: (I) study of mask thickness, (II) study of gap size, and (III) study of dependency and behavior of soft magnetic material in the masks. The discussion, however, starts with a look at the analog system for different permanent magnet materials, i.e., a system without masks, to make the transition between the aforementioned categories smoother.

---

[3] MatLab is a powerful matrix processing tool `http://www.mathworks.com/`

4.2.1 Theory and simulation comparisons in analog systems

Figure 4.3 shows a general contour plot of the simulated values of component B_x and B_z of the magnetic stray field in an analog system.

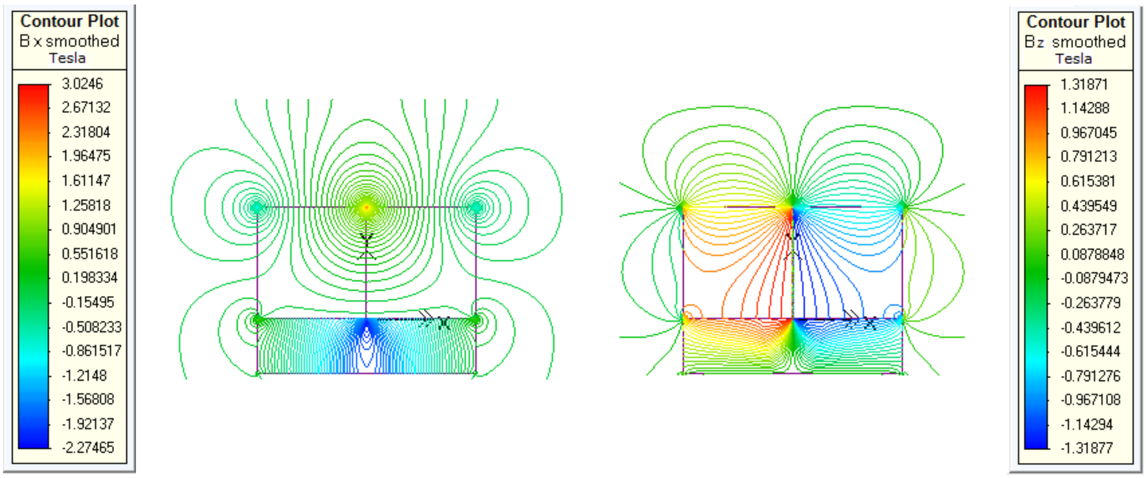

Figure 4.3: *Contours of the flux density, produced by the tangential component (B_x, left) and normal component (B_z, right) of the magnetic stray field in an analog system. The permanent magnets are made with NdFeB 42H specifications, cf., Table 4.1. The yoke prevents flux leakage, i.e., eliminates charges of opposite signs on the bottom poles of the magnets, thus increasing the stray field over the upper plane of the structure.*

Close to the surface in the vicinity of point O, as explained in Figure 3.1, B_x reaches values several times stronger than the induction of the magnet material itself, while B_z changes sign crossing the junction line, in agreement with theory [6].

Several interesting characteristics of the analog systems are studied, including comparisons of theoretical and simulated B_x and B_z distributions 0.01 mm above the surface of the magnets, as shown in Figure 4.4 and 4.5, respectively. Note that, all coordinates are relative to the axis in Figure 3.1. A comparison of the distribution of B_x versus the distance to the magnets in the z-direction, normal to the magnet surfaces, is shown in Figure 4.6, while Figure 4.7 shows comparisons of $\mathbf{B}\nabla\mathbf{B}$ distributions, 0.01 mm above the surface of the magnets.

The strength of the components of the stray field, according to simulation distributions in Figure 4.4-4.6, are precisely linear with the coercivity of the magnets, thus in agreement with the theoretical approximations derived in Equation 3.1 and 3.2, where B_x, $B_z \propto M_s$. Furthermore, the theoretical approximations match the shape of the simulated distributions. There are deviations in the tangential distributions close to O, however, caused by the fact that the field is overestimated with a factor of 10-15%. Note that, when $x = 0$ the second term in Equation 3.1 gives positive contributions to the tangential field when $z < 1$, with a diverging behavior growing as $z \rightarrow 0$, zero contribution when $z = 1$, and small negative contributions when $z > 1$. Knowing that the theoretical approximation to B_x is extremely sensitive when $z \rightarrow 0$, the calculations are only performed as low as $z = 0.01$, i.e., 0.01 mm above the surface of the magnets. However, after correcting the theoretical tangential distributions for overestimating the tangential field in O, they match the simulations very well.

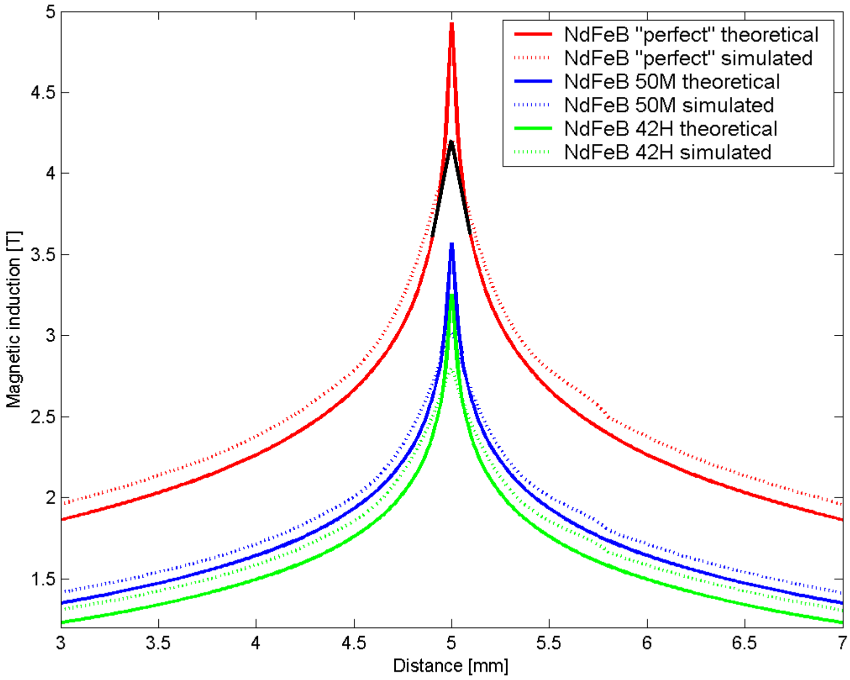

Figure 4.4: *Comparison of theoretical and simulated B_x distributions 0.01 mm above the surface of three different permanent magnet materials. The black peak in the NdFeB "perfect", theoretical distribution is corrected for a 15% overestimation of the field. The corrected theoretical distribution matches the simulated distribution better and better closing in on O, until there is a complete match in $x = y = 0$ as explained in Chapter 3. The correction constitutes a similar behavior for all magnet materials.*

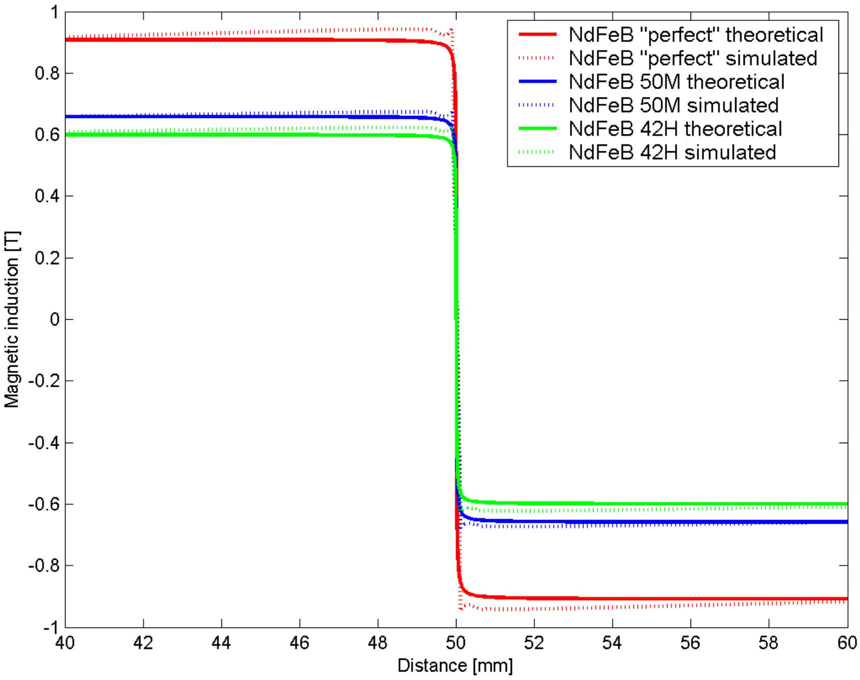

Figure 4.5: *Comparison of theoretical and simulated B_z distributions 0.01 mm above the surface of three different permanent magnet materials. The theoretical distributions are not overestimated and match the simulated distributions very well.*

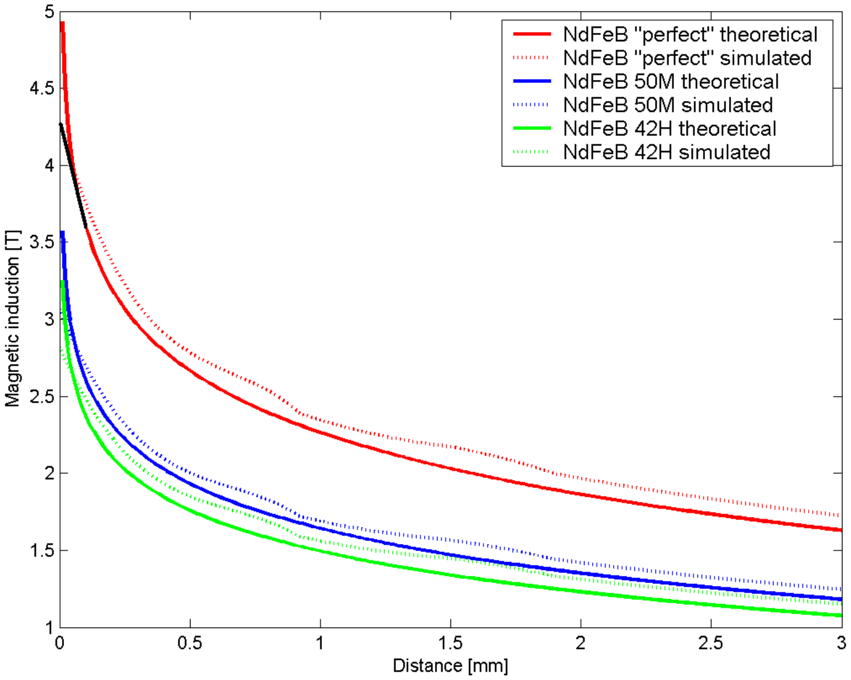

Figure 4.6: *Comparison of theoretical and simulated* B_x *distributions in* $x = 0$*, versus the distance from the surface of three different permanent magnet materials. The first point in the curves corresponds to* $z = 0.01$*. The black line in the NdFeB "perfect", theoretical distribution is corrected for a 15% overestimation of the field, and in* $z = 0.01$ *there is a complete match between theory and simulation.*

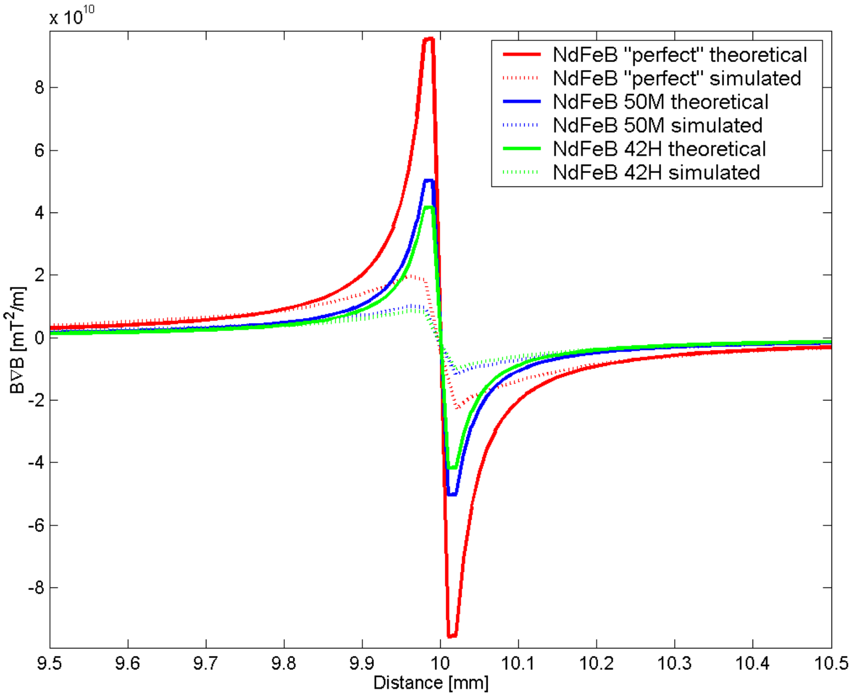

Figure 4.7: *Comparison of theoretical and simulated* $\boldsymbol{B}\nabla\boldsymbol{B}$ *distributions 0.01 mm above the surface of three different permanent magnet materials. Note that, when corrected for a 15% overestimation of the tangential field the maximum value of theoretical and simulated* $\boldsymbol{B}\nabla\boldsymbol{B}$ *distributions are approximately the same.*

From Equations 3.1 and 3.2 it follows that

$$\mathbf{B}\nabla\mathbf{B} \propto M_s^2\left(\frac{A(a,x,z)\partial A(a,x,z)}{\partial x} + \frac{B(a,x,z)\partial B(a,x,z)}{dz}\right), \tag{4.1}$$

where A and B depends only on the dimensions of the system. This behavior is also observed in the simulations. The NdFeB 42H simulation states that $\mathbf{B}\nabla\mathbf{B}$ reaches a value of 8.6×10^9 mT^2/m, in a distance of 0.01 mm to the surface of the magnets. When the theoretical tangential field distribution is corrected for a 15% overestimation, the theoretical value of $\mathbf{B}\nabla\mathbf{B}$ reaches a value approximately that obtained in simulations, thus placing both within range of the expected result of 10^8-10^{10} mT^2/m, derived in [6].

Thus, so far there is an agreement between simulations and theory. The theoretical and simulated models, however, are based on ideal adjoining surfaces of the materials, opposed to non-ideal in real life devices, consequently predicting unrealistically obtainable values.

4.2.2 Mask thickness comparisons

The behavior of the magnetic stray field is investigated in Figure 4.8 and 4.9, where masks of different thicknesses, cf., Table 4.2, are added on top of a half open Kittel domain. The tangential component of the field drastically changes characteristics, when the distance to the masks is 0.01 mm.

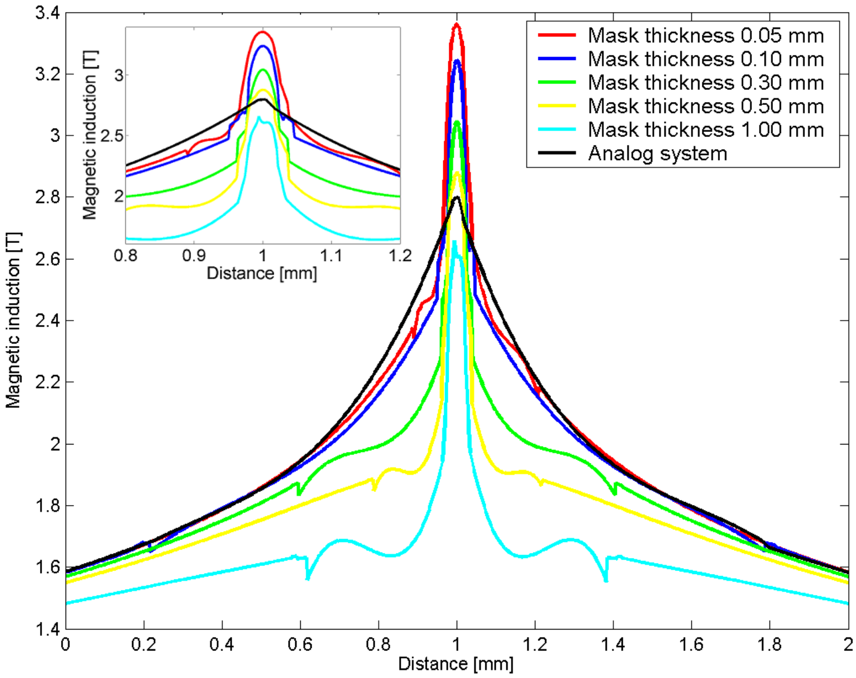

Figure 4.8: *Comparison of tangential magnetic stray field distributions (B_x) 0.01 mm above the surface of vanadium permendur masks of different thicknesses. The gap size is kept constant at 0.05 mm, and NdFeB 42H magnets are used. The analog comparison is taken 0.01 mm above the surface of the magnets. The inset shows the same distributions, however, zoomed closer in around the center of the gap.*

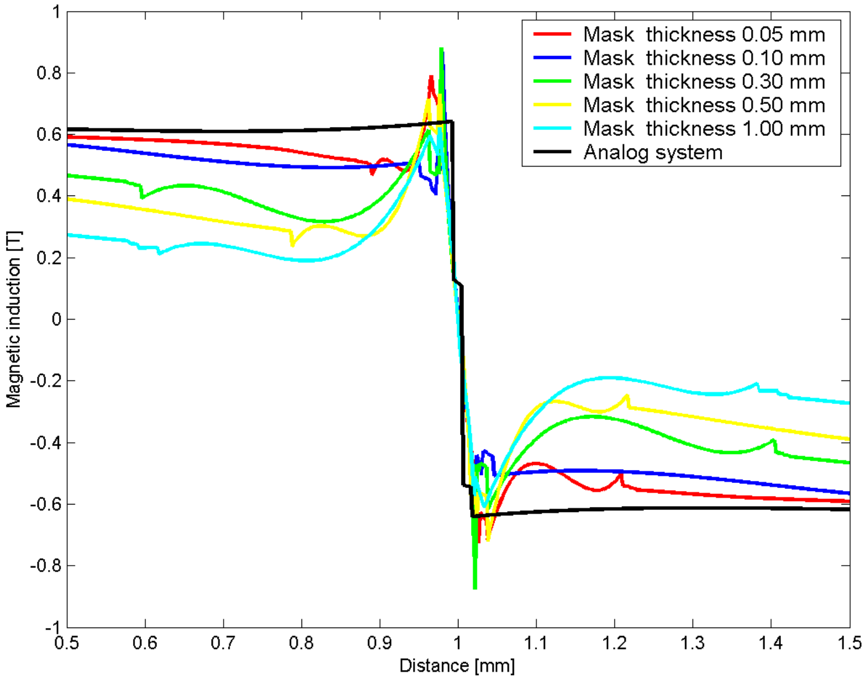

Figure 4.9: *Comparison of normal magnetic stray field distributions* (B_z) *0.01 mm above the surface of vanadium permendur masks of different thicknesses. The gap size is kept constant at 0.05 mm, and NdFeB 42H magnets are used. The analog comparison is taken 0.01 mm above the surface of the magnets.*

The effect of adding 0.05 mm thick masks, forming a 0.05 mm gap size on top of a half open Kittel domain, is studied by Il'yashenko *et al.* [5]:

> "A device with a mask creates a magnetic field with the tangential component of the induction exceeding 4.0 T (Fig. 2). This is almost 1.3 times more than in an analogue system [6]. The width of the peak of the tangential component of the magnetic field at half height in the device with the mask is narrower than for an analogue system without a mask (Fig. 2)."

Almost the exact same pattern is observed in the new simulations. After adding 0.05 mm thick masks, forming a gap of 0.05 mm on top of the domain, the tangential component of the magnetic stray field, in a distance of 0.01 mm above the masks, is about 1.2 times larger than in the analog system. The width of the peak of this tangential field at half height, is also narrower than in the analog system, thus producing a higher gradient.

When the masks thickens, the values of the tangential and normal fields are lowered, connected to the fact that they are measured further and further away from the source of the stray field, as well as the masks soaking up more and more flux. As the thickness of the masks approach 0.50 mm, the strength of the tangential field is even lower than in the analog structure. However, this does not affect the gradient. The shape of the tangential field is preserved, and stays much sharper than in the analog system, regardless of mask thickness.

Rave *et al.* [25] show that ferromagnetic bodies exhibit a singular behavior in the vicinity of sharp square edges, caused by the demagnetization field around the edge. This is observed as fringes, or sudden peaks, in the center of the normal distribution of the stray field, where the upper corners of the masks are located. The effect is not directly observable in the tangential field. In this case, the two singularities merge together to form one, adding to the total induction of the peak. However, above an exchange distance $\Lambda = (A/2\pi M_s^2)^{\frac{1}{2}}$, where A is the exchange constant, the singularities are effectively smoothed by a logarithmic singularity in the exchange field, supported by Thiaville *et al.* [26], and as a result a crystal anisotropy field always has a finite value.

Figure 4.10 shows distributions of the tangential field in $x = 0$ versus the z-direction normal to the surface. The gap size is kept constant at 0.05 mm, and the thickness of the masks is varied. As expected, the tangential component is linear with the thickness, while the steepness of the curves are the same regardless of thickness, supported by the tangential distribution comparison in Figure 4.8.

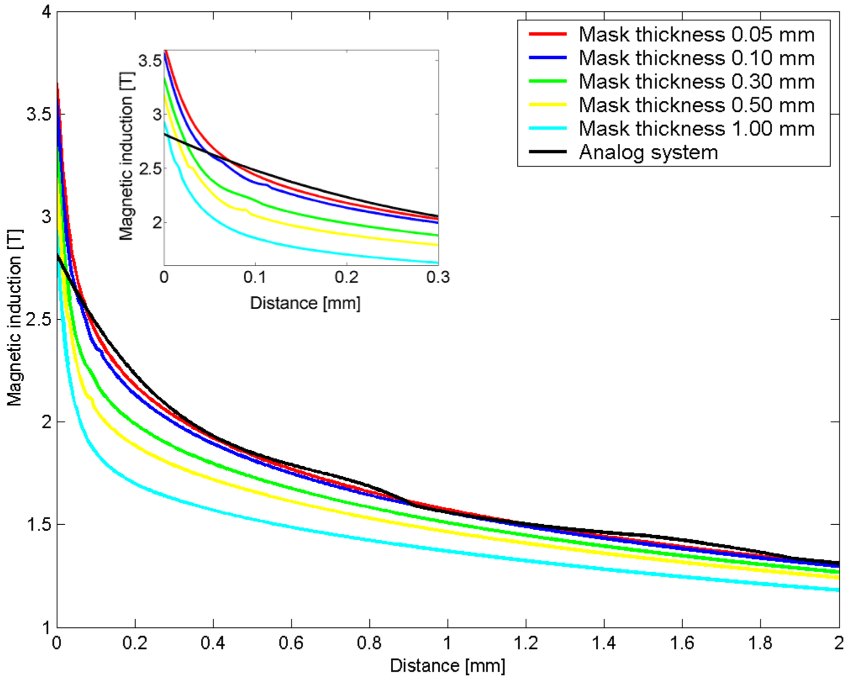

Figure 4.10: *Comparison of B_x distributions in $x = 0$, versus the distance to the surface of vanadium permendur masks, i.e., in the z-direction relative to $z = 0$. The gap size is kept constant at 0.05 mm, and the mask thicknesses varies. NdFeB 42H permanent magnets are used in all distributions. The analog comparison is taken 0.01 mm above the surface of the magnets. The inset shows the same distributions, however, for a smaller z-distance.*

Figure 4.11 now shows how $\mathbf{B}\nabla\mathbf{B}$ behaves 0.01 mm above the surface of masks, that varies in thickness when the gap size is kept constant at 0.05 mm. Clearly, the tendency is that $\mathbf{B}\nabla\mathbf{B}$ increases, as the thickness of the masks decreases. A structure, with 0.05 mm thick masks, produces a value roughly six times larger than in the analog structure. Even for a mask as thick as 1.00 mm, the value is almost four times that in the analog structure.

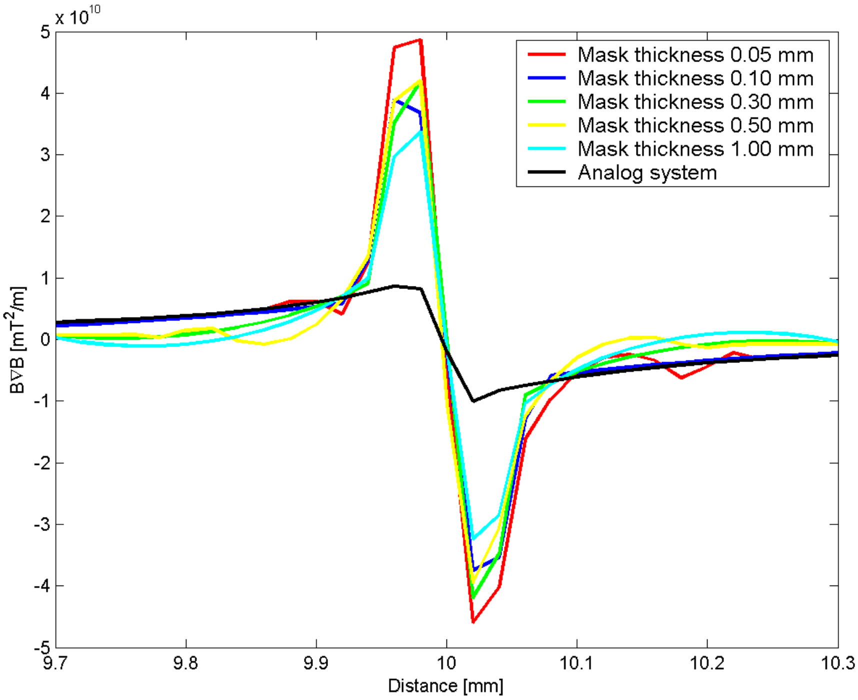

Figure 4.11: *Comparison of* $\boldsymbol{B}\nabla\boldsymbol{B}$ *distributions 0.01 mm above the surface of vanadium permendur masks of different thicknesses. The gap size is kept constant at 0.05 mm, and NdFeB 42H magnets are used. The analog comparison is taken 0.01 mm above the surface of the magnets.*

The noise that is seen in the distributions is caused by numerical imperfections in MagNet, and is not real physical properties of the structure. In a best case scenario, the curves will be smooth. Instabilities occur, nevertheless, as a result of the simulations running with a tolerance of only $5{\cdot}10^{-6}$ in the refinement of the mesh structure. The current version of MagNet is only able to operate with a maximum of 4 gigabyte of physical memory. Once the tolerance closes in on $5{\cdot}10^{-6}$ this threshold is reached, and the program is not able to create more nodes in the mesh, thus, terminating the process. This is of course connected to the fact that, representing very thin masks, and small air gaps, where field values and permeabilities change rapidly, requires a lot of nodes.

Figure 4.12 and 4.13 indicates that, as the distance to the masks increases $\mathbf{B}\nabla\mathbf{B}$ decreases. Further notice that, in a distance of 0.10 mm the analog distribution is larger than in any of the other distributions. The reason is that the field, hence the gradient, is no longer influenced by the singularities in the vicinity of the sharp corners of the masks. Consequently the masks now have the opposite effect than what is desired. A thicker mask increases the distance to the source of the stray field, as well as "trapping" more flux, which combined lowers the magnetic induction. In this distance $\nabla\mathbf{B}$ is on the order of 10^6 mT/m, thus consistent with the simulations in [5].

The results suggests that, in order to increase the magnetic separation potential of the device, a mask thickness of 0.05 mm is favorable. The separation should also be performed as close as possible to the surface of the masks, and in any case closer than 0.10 mm, in order to utilize the full potential in the gradient of the field.

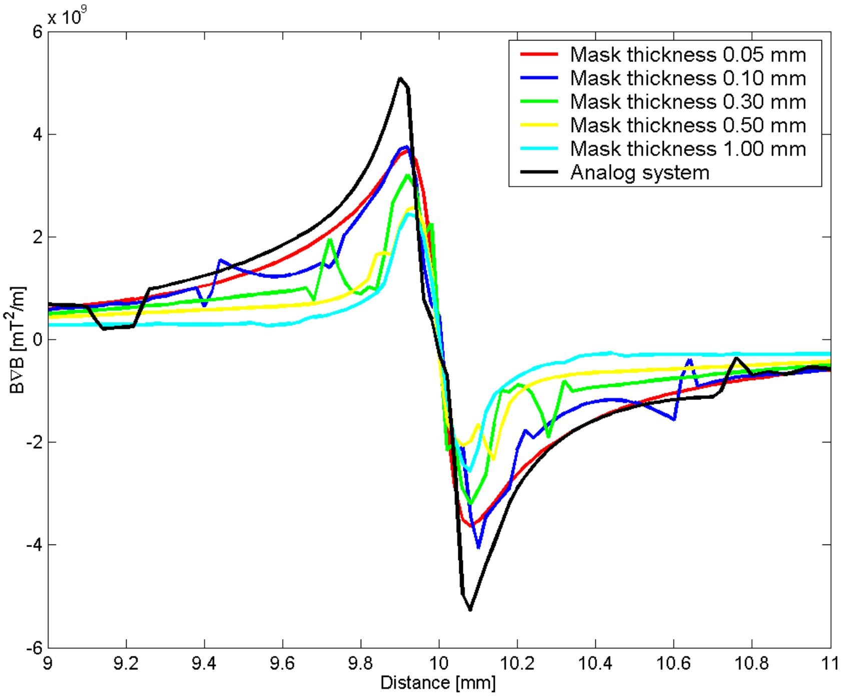

Figure 4.12: *Comparison of* $\boldsymbol{B}\nabla\boldsymbol{B}$ *distributions 0.10 mm above the surface of vanadium permendur masks of different thicknesses. The gap size is kept constant at 0.05 mm, and NdFeB 42H magnets are used. The analog comparison is taken 0.10 mm above the surface of the magnets.*

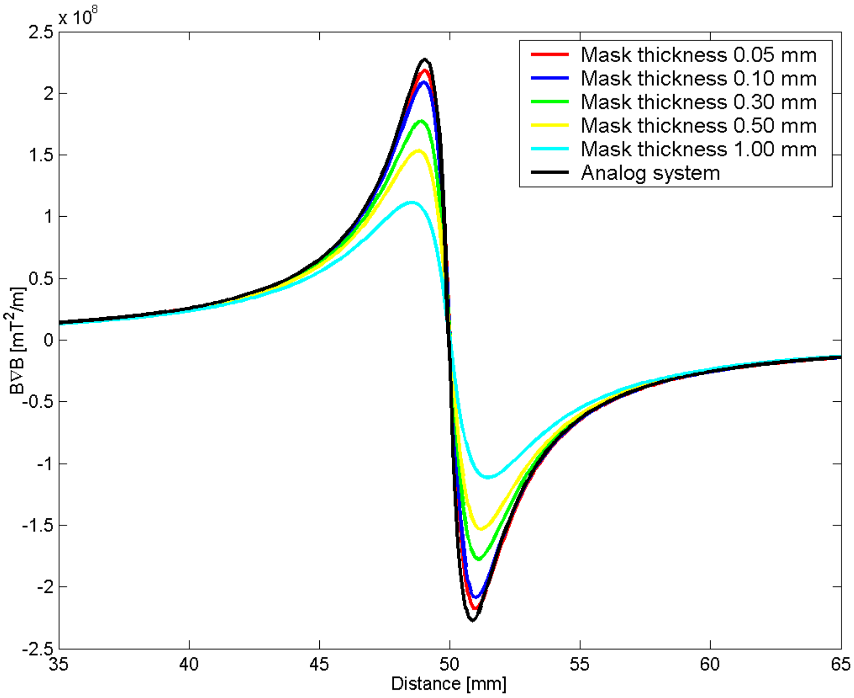

Figure 4.13: *Comparison of* $\boldsymbol{B}\nabla\boldsymbol{B}$ *distributions 1.00 mm above the surface of vanadium permendur masks of different thicknesses. The gap size is kept constant at 0.05 mm, and NdFeB 42H magnets are used. The analog comparison is taken 1.00 mm above the surface of the magnets.*

As a concluding remark about mask thicknesses, it is worth to mention that further narrowing the field distribution will drastically increase **B∇B**, since most of the dependency here lies in the shape of the magnetic stray field. Additionally, as seen in Figure 4.14, the z-gradient of **B** opposes the x-gradient of **B**. The gradients are on the same order, however, B_x is roughly five times larger than B_z, thus $B_x(\nabla B)_x$ is the dominating contributor to the magnetic force and will keep growing relatively stronger, since the new design increases the tangential field, but not the normal.

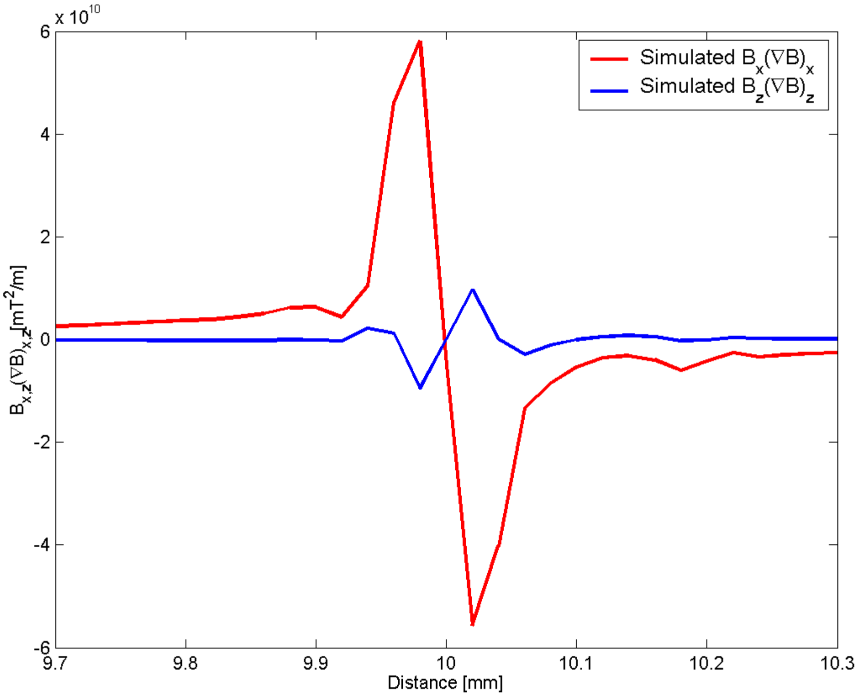

Figure 4.14: *Comparison of simulated $B_x(\nabla B)_x$ and $B_z(\nabla B)_z$ distributions 0.01 mm above the surface of the masks. The comparison shows that $B_z(\nabla B)_z$ opposes $B_x(\nabla B)_x$, however, $B_x(\nabla B)_x$ is roughly five times stronger than $B_z(\nabla B)_z$, thus the dominating contributor to the magnetic force.*

4.2.3 Gap size comparisons

It has been established that **B∇B** increases, compared to an analog structure when the thickness of the masks decreases, but how are the shapes of B_x and B_z affected, facing increasing gap sizes? In order to investigate this, structures with 0.05 mm thick masks are subject to increasing gap sizes, according to Table 4.2, and Figure 4.15-4.16 and 4.17 show how B_x and B_z changes, respectively.

As the gap size increases the contribution to the tangential field, caused by singularities in the demagnetization field around the sharp corners of the masks, become more and more distinct. As mentioned earlier, this effect is observed as a single fringe in the tangential field when the gap size is very small, in fact smaller than 0.10 mm. Starting from a gap of 1.00 mm, Figure 4.16 shows just how the shape of the tangential profile is "pushed" upwards, as the fringes merge when the gap decreases in size. Furthermore, when the gap size increases towards and above

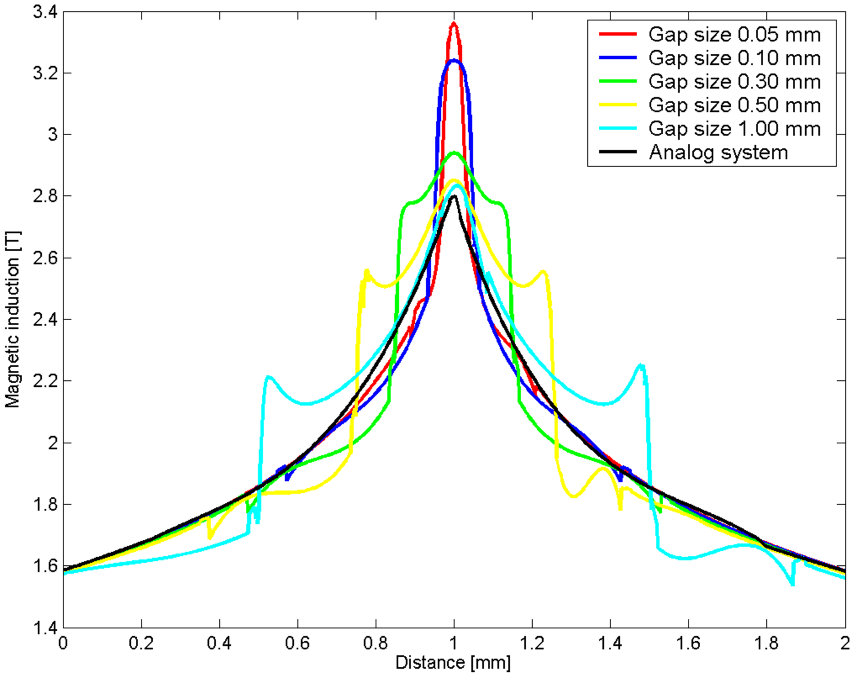

Figure 4.15: *Comparison of tangential magnetic stray field distributions (B_x) 0.01 mm above the surface of masks of vanadium permendur for different gap sizes. The mask thickness is kept constant at 0.05 mm, and NdFeB 42H magnets are used. The analog comparison is taken 0.01 mm above the surface of the magnets.*

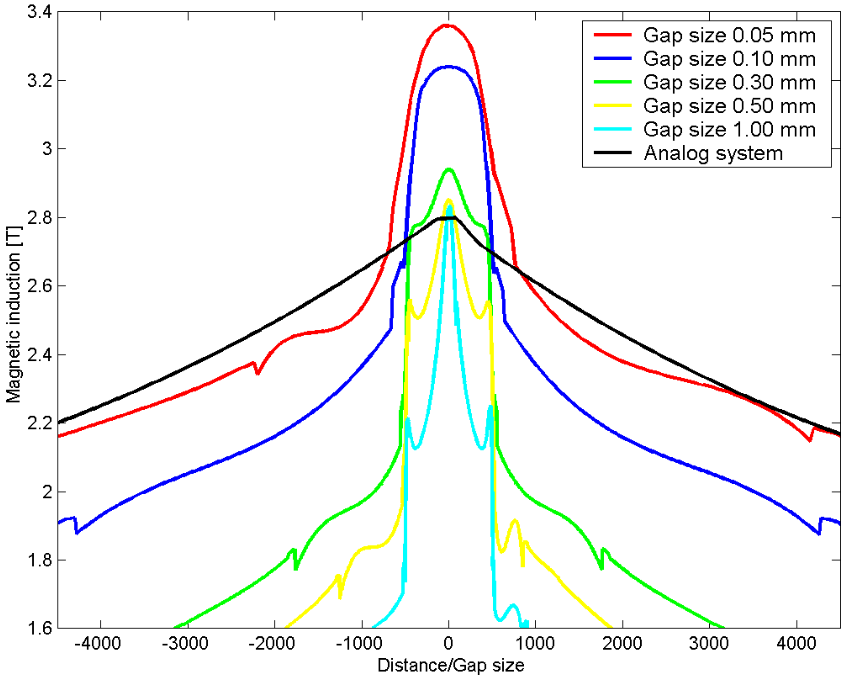

Figure 4.16: *Comparison of the same tangential magnetic stray field distributions (B_x) 0.01 mm above the surface of masks of vanadium permendur as in Figure 4.15, with distances scaled to the respective gap sizes. The mask thickness is kept constant at 0.05 mm, and NdFeB 42H magnets are used. The analog comparison is taken 0.01 mm above the surface of the magnets and scaled to fit the x-axis.*

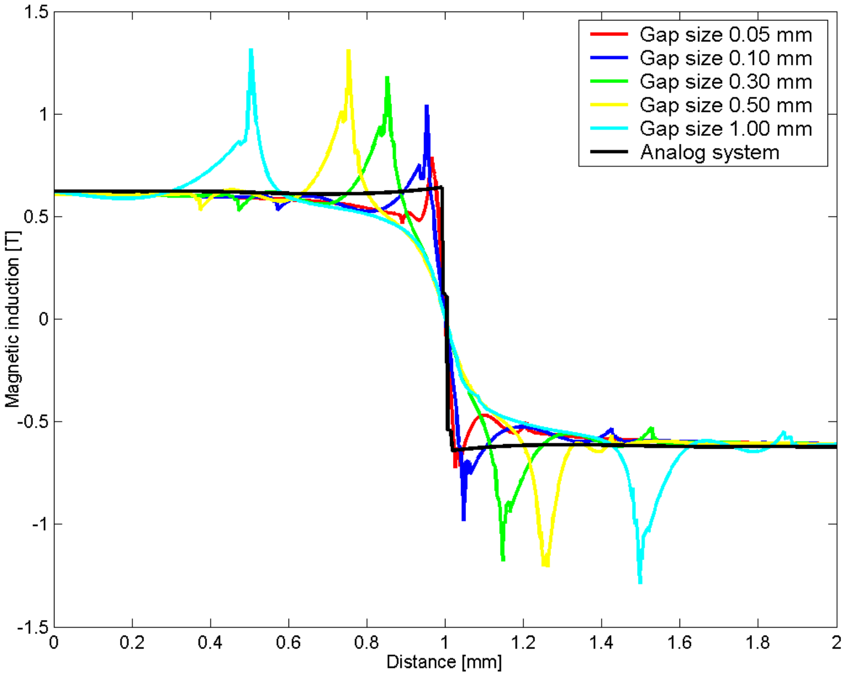

Figure 4.17: *Comparison of normal magnetic stray field distributions (B_z) 0.01 mm above the surface of masks of vanadium permendur for different gap sizes. The mask thickness is kept constant at 0.05 mm, and NdFeB 42H magnets are used. The analog comparison is taken 0.01 mm above the surface of the magnets.*

0.30 mm, the tangential distribution converges towards the strength and shape of the analog distribution, but with visible fringes located at the position of the mask corners, matching the fringes in the normal distribution.

As discussed in the previous section, the gradient is no longer influenced by singularities in the demagnetization field when the distance to the masks is increased to 0.10 mm. This behavior is additionally seen in Figure 4.18 and 4.19, where the fringes in the tangential and normal distribution almost disappear, regardless of gap size. In fact, both distributions converge towards the behavior of the analog system, because the masks are only 0.05 mm thick, and as a result only have a small negative effect on the magnetic stray field.

Figure 4.20-4.21 show how the strength, shape, and position of $\mathbf{B}\nabla\mathbf{B}$ changes with increasing gap sizes. Above gap sizes of approximately 0.10 mm, the driving forces in $\mathbf{B}\nabla\mathbf{B}$ are no longer located in the center of the gap, but caused by gathering and escape of flux in and around the corners of the masks. Hence, the locations of the field gradient minima and maxima are determined by the gap size. The singularities at the corners, however, are caused by ideal square edges. Precisely controlling the shape of these corners in real devices is difficult. A slightly rounder corner will most likely significantly decrease the effect. The simulations, nevertheless, supports the idea of adding masks on top of the magnets, in order to increase the potential of the magnetic force, but strongly suggests using gap sizes below 0.10 mm.

The maximum value of $\mathbf{B}\nabla\mathbf{B}$, found from simulation 0.01 mm above the surface of the masks, is a factor of eight lower compared to what is reported in [5], but still roughly six times higher than in the corresponding analog structure. On the

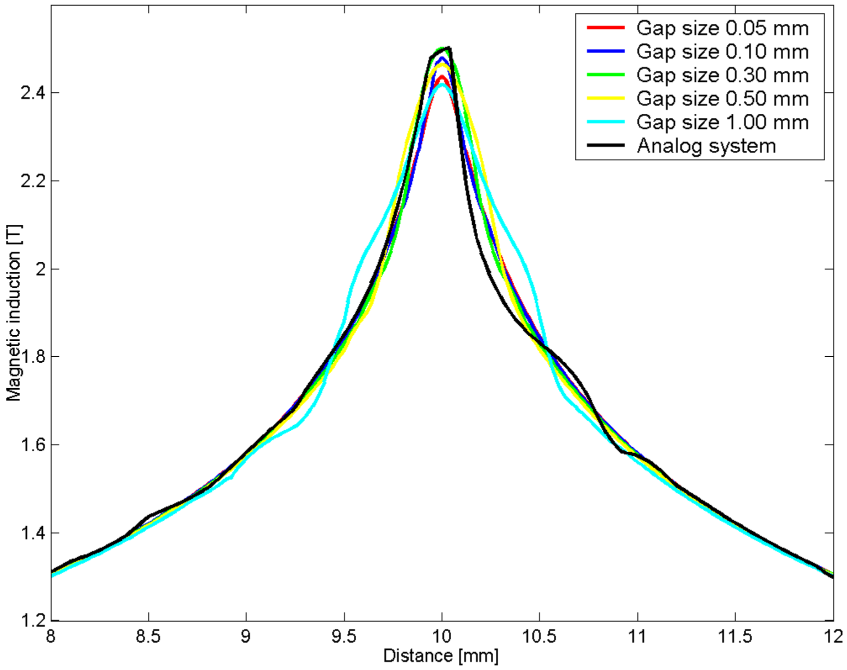

Figure 4.18: *Comparison of tangential magnetic stray field distributions (B_x) 0.10 mm above the surface of masks of vanadium permendur for different gap sizes. The mask thickness is kept constant at 0.05 mm, and NdFeB 42H magnets are used. The analog comparison is taken 0.10 mm above the surface of the magnets.*

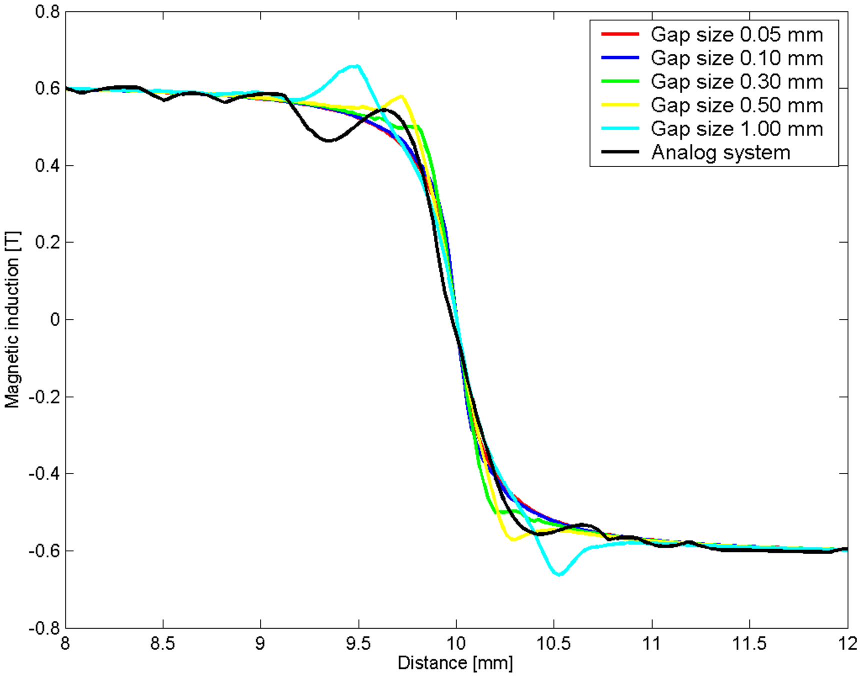

Figure 4.19: *Comparison of normal magnetic stray field distributions (B_z) 0.10 mm above the surface of masks of vanadium permendur for different gap sizes. The mask thickness is kept constant at 0.05 mm, and NdFeB 42H magnets are used. The analog comparison is taken 0.10 mm above the surface of the magnets.*

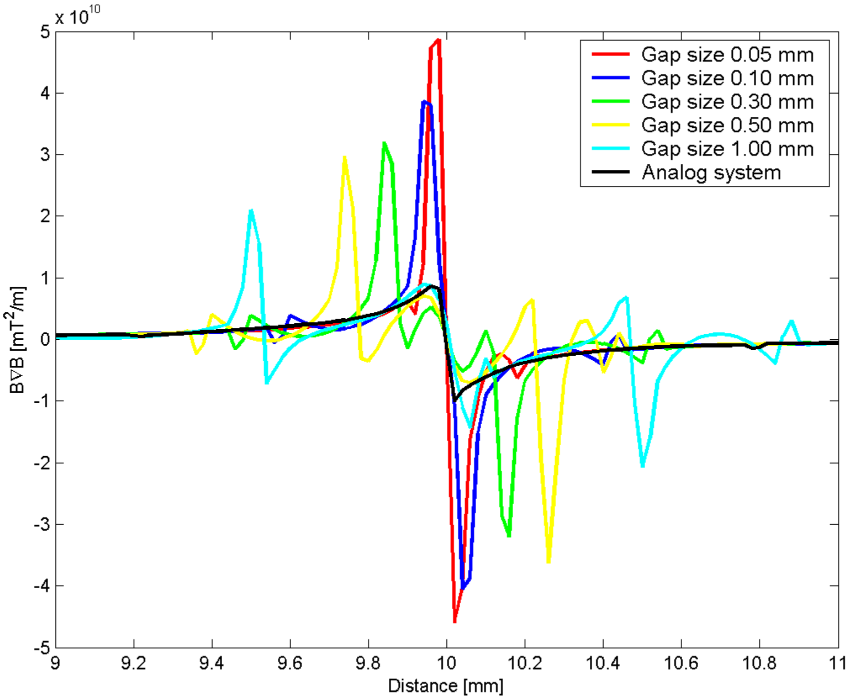

Figure 4.20: *Comparison of $\boldsymbol{B}\nabla\boldsymbol{B}$ distributions 0.01 mm above the surface of masks of vanadium permendur for different gap sizes. The mask thickness is kept constant at 0.05 mm, and NdFeB 42H magnets are used. The analog comparison is taken 0.01 mm above the surface of the magnets.*

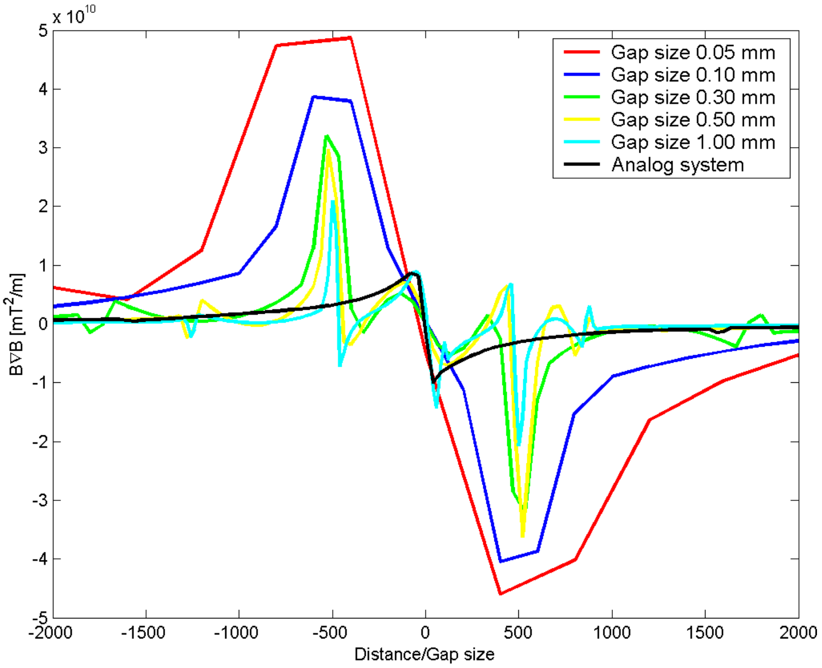

Figure 4.21: *Comparison of the same $\boldsymbol{B}\nabla\boldsymbol{B}$ distributions 0.01 mm above the surface of masks of vanadium permendur as in Figure 4.20, with distances scaled to the respective gap sizes. The mask thickness is kept constant at 0.05 mm, and NdFeB 42H magnets are used. The analog comparison is taken 0.01 mm above the surface of the magnets, and scaled to fit the x-axis.*

other hand, an interesting thing is observed in the $\mathbf{B}\nabla\mathbf{B}$ distributions 0.01 mm above the masks in Figure 4.22. The magnetic field data is obtained 2.00 mm between the end points around the center of the air gap in steps of 0.002 mm, opposed to 20.0 mm in steps of 0.02 mm used so far. Due to the aforementioned problem with numerical instabilities, caused by discontinuities in permeabilities and field values, the distributions are extremely noisy, and consequently hard to interpret. The general behavior somewhat opposes what is seen in Figure 4.20, nevertheless, $\mathbf{B}\nabla\mathbf{B}$ reaches values of 10^{11} mT^2/m, much closer to the reported value of 4.2×10^{11} mT^2/m in [5].

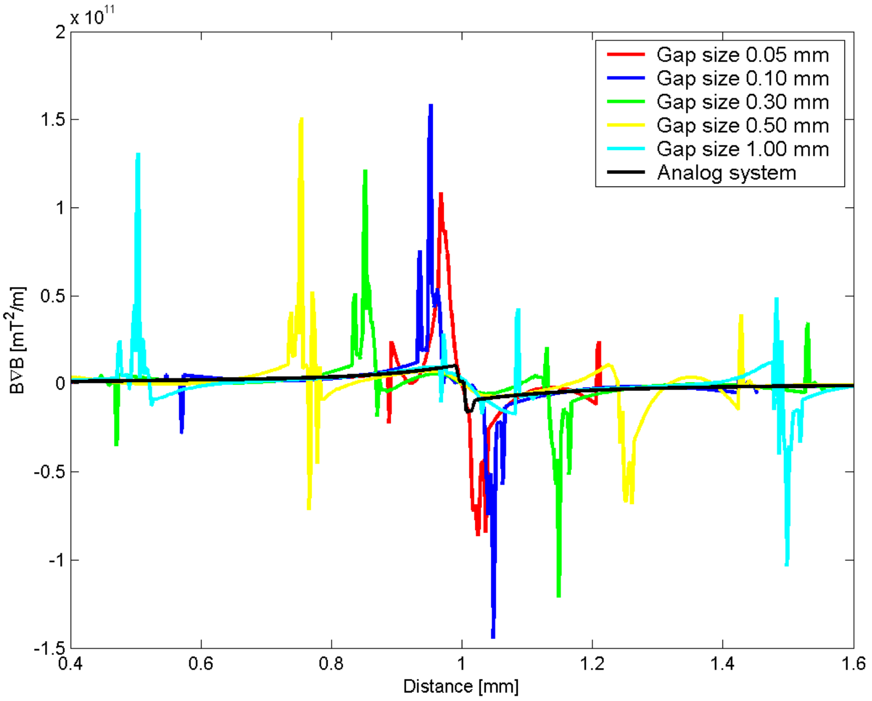

Figure 4.22: *Comparison of $\boldsymbol{B}\nabla\boldsymbol{B}$ distributions 0.01 mm above the surface of vanadium permendur masks 2.00 mm between the end points symmetrically around $x = 0$. The masks are kept constant at 0.05 mm, and NdFeB 42H permanent magnets are used.*

A preliminary conclusion so far suggest that the thinner the mask the better, but more importantly, the gap size needs to be smaller than approximately 0.10 mm. However, most importantly is the fact that, the new design only produces larger $\mathbf{B}\nabla\mathbf{B}$ values than in a corresponding analog structure, if the distance to the masks is smaller than 0.10 mm. In an attempt to determine the exact distance above the masks, where the singularites in the demagnetization field are undetectable, $\mathbf{B}\nabla\mathbf{B}$ distributions 0.04 mm above vanadium permendur masks of different thicknesses, where the gap size is kept constant at 0.05 mm, are compared in Figure 4.23. The distributions are very noisy, still connected to numerical instabilities caused by discontinuities in permeability and field values. Additionally, the individual distributions with masks might not be accurately described, relative to each other. There is, nevertheless, little doubt that a device with masks produces larger $\mathbf{B}\nabla\mathbf{B}$ values than that in the analog structure, but only slightly larger. Increasing the distance to 0.05 mm will most likely cause all distributions to converge towards the analog distribution. A distance of 0.04 mm is thus a much better estimate of the distance above the masks where the singularites in the demagnetization field become undetectable. In other words, the new design only works better and produces larger **B∇B** values than a corresponding analog structure, *if* the distance to the masks is equal to, or less than 0.04 mm. For future references, this distance shall be referred to as the *critical* distance.

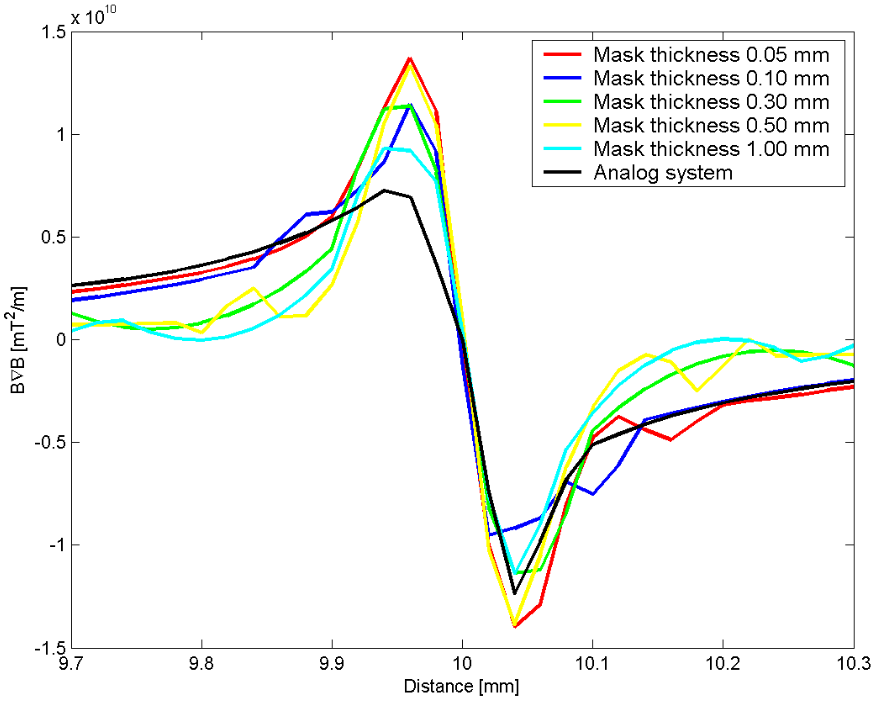

Figure 4.23: *Comparison of* $\boldsymbol{B\nabla B}$ *distributions 0.04 mm above the surface of vanadium permendur masks of different thicknesses. The gap size is kept constant at 0.05 mm, and NdFeB 42H magnets are used. The analog comparison is taken 0.04 mm above the surface of the magnets.*

There is a problem, however, that needs more investigation in order to make any final conclusions. How important are the characteristics of the materials used in the masks, e.g., magnetic saturation and permeability, and are the behavior of the non-linear materials representative to the real materials?

4.2.4 Examining behavior of soft magnetic mask material

A comparison of the tangential and normal distribution of the magnetic stray field 0.01 mm and 0.10 mm above the surface of vanadium permendur, and low carbon steel masks, are shown in Figure 4.24 and Figure 4.25, respectively.

The magnetic saturation of vanadium permendur is 7.66% higher than that of low carbon steel. Using vanadium permendur, contra low carbon steel in the masks, increases the peak in the tangential distribution by 2.3% 0.01 mm above the surface of the masks. In a distance of 0.10 mm, however, the gain drops to 0.4%, confirming that the singularities in the demagnetization above the mask corners have dissappeared. Increasing the saturation of the masks thus changes the strength of **B∇B**, demonstrated in Figure 4.26. Choosing vanadium permendur over low carbon steel makes up for a 6-8% increase in **B∇B**, very close to the difference in magnetic saturation between

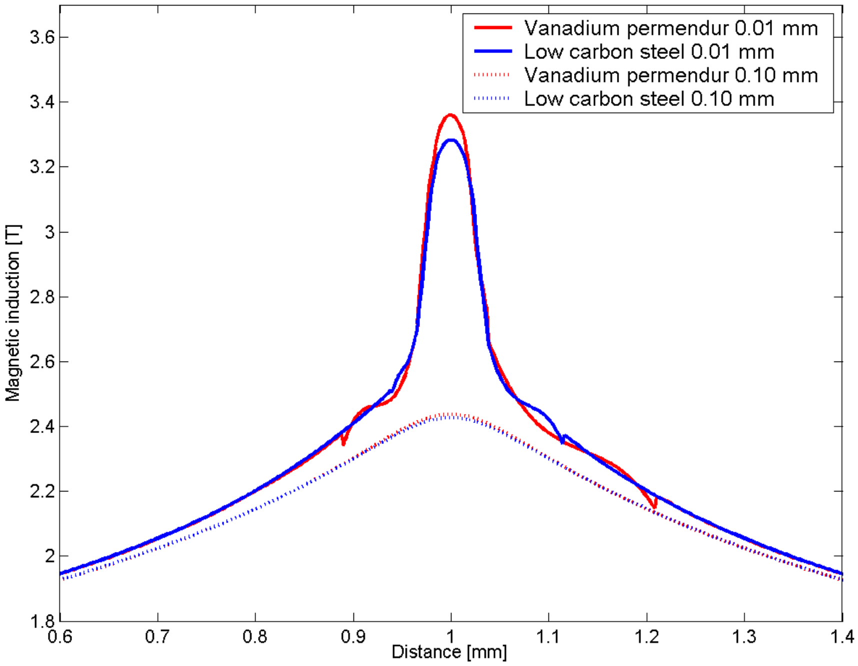

Figure 4.24: *Comparison of tangential magnetic stray field distributions (B_x) 0.01 and 0.10 mm above the surface of vanadium permendur and low carbon steel masks. The mask thickness and gap size is kept constant at 0.05 mm, and NdFeB 42H magnets are used.*

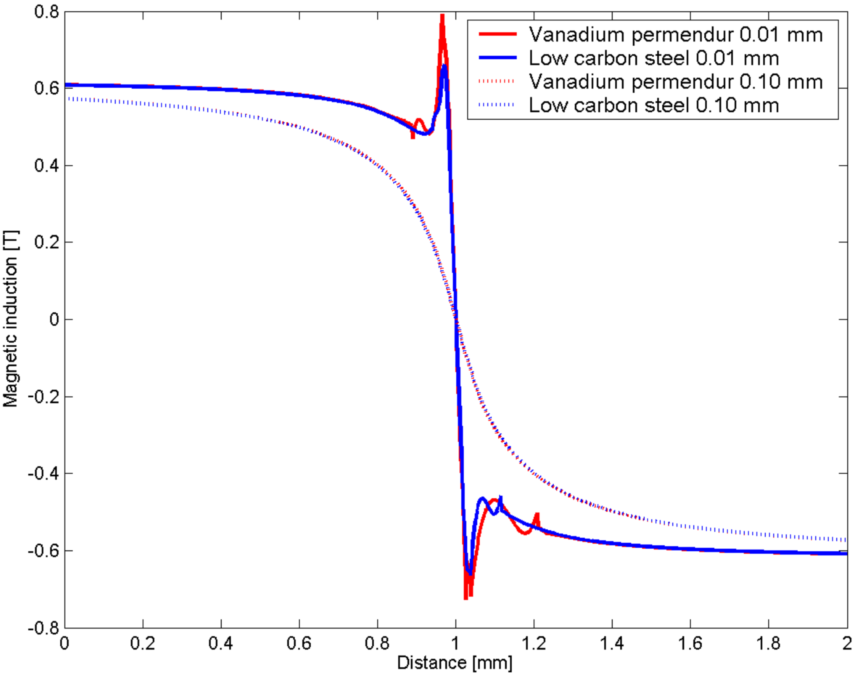

Figure 4.25: *Comparison of tangential magnetic stray field distributions (B_z) 0.01 and 0.10 mm above the surface of vanadium permendur and low carbon steel masks. The mask thickness and gap size is kept constant at 0.05 mm, and NdFeB 42H magnets are used.*

the materials. Consequently, increasing the magnetic saturation of the mask material constitute close to a linear increase in $\mathbf{B}\nabla\mathbf{B}$ below the critical distance.

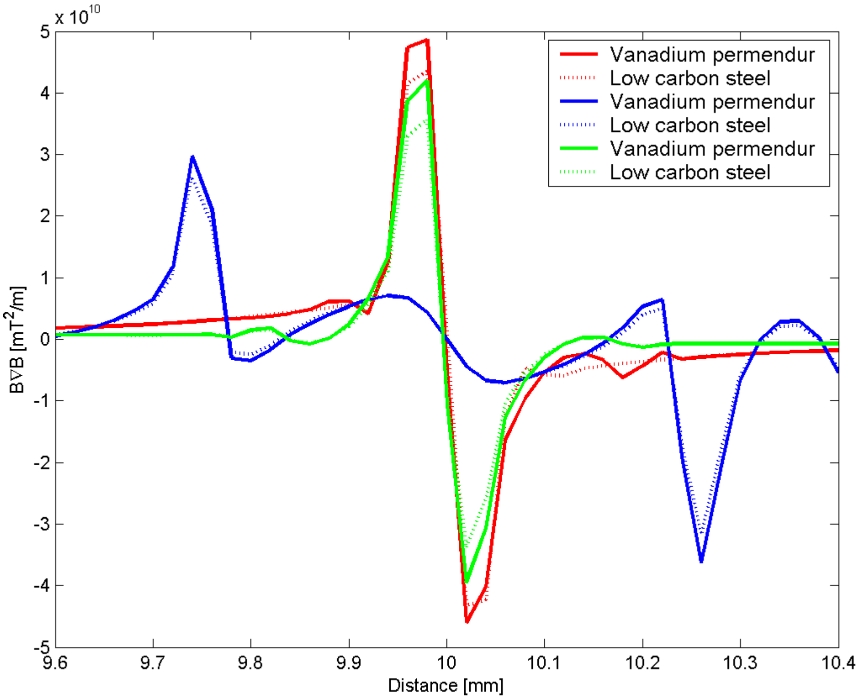

Figure 4.26: *Comparison of $\boldsymbol{B}\nabla\boldsymbol{B}$ distributions 0.01 mm above the surface of vanadium permendur, and low carbon steel masks. The colored curves correspond to the following: red has a mask thickness of 0.05 mm and a gap size of 0.05 mm; green has a mask thickness of 0.05 mm and a gap size of 0.50 mm; blue has a mask thickness of 0.50 mm and a gap size of 0.05 mm. NdFeB 42H magnets are used.*

A connection between the magnetic saturation of the masks, the strength of the magnetic stray field, and its gradient has been worked out, but how reliable are the results? Simulating very thin and non-linear materials, especially in direct contact with permanent magnets, seriously aggravates the problem at hand. As a result, an assessment of the behavior of the non-linear materials is necessary, i.e., how the permeability and saturation change with an externally applied field.

Figure 4.27 shows the magnetic induction (B_m), external magnetic field (H_m), and magnetization saturation (B_s) in the middle of vanadium permendur, and low carbon steel masks. The external field is represented as the field, solely produced by the permanent magnets, in Ampere per meter, multiplied by the permeability of free space (μ_0). Two weak spots are located symmetrically around the center, to the far left and right above the magnets, in agreement with the field lines observed in Figure 3.4. In this area, the value of the external field drops as low as 50 A/m, nevertheless, the magnetic induction inside the masks reaches 0.5 T, dictating highly permeable mask materials. This observation is sustained in Figure 4.28, reflecting the relative permeability (μ_r) across the masks, where the maximum relative permeability of vanadium permendur is approximately 7000 times unity. Closing in on the air gap, however, the permeability drops to approximately twice that of free space, and finally to unity inside the air gap, as seen in Figure 4.29.

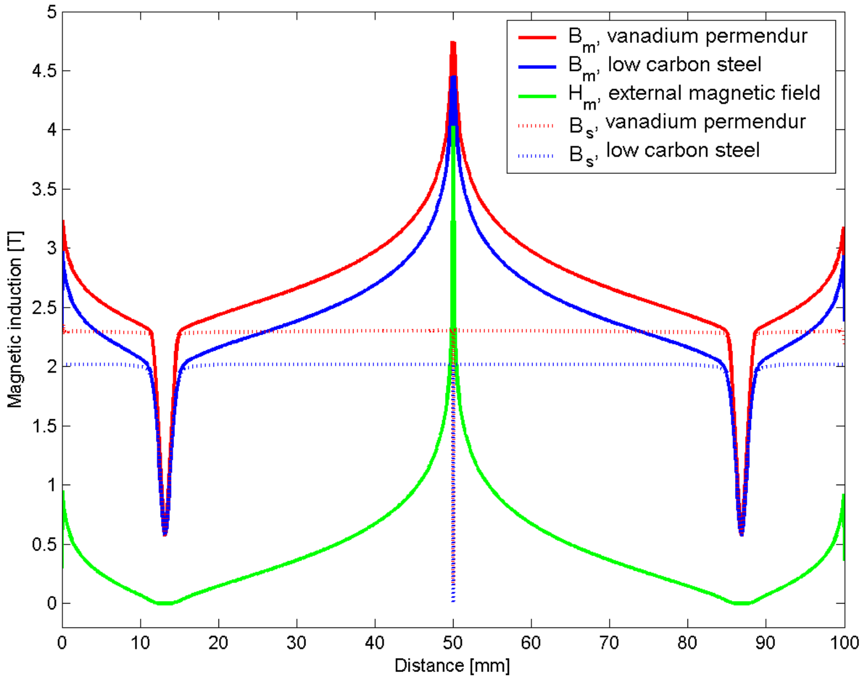

Figure 4.27: *Comparisons of the magnetic induction, external magnetic field as well as magnetic saturation of vanadium permendur, and low carbon steel masks. The masks are 0.05 mm thick, and resting on top of NdFeB 42H permanent magnets with a magnetic remanence $B_r = 1.32$ T. All comparisons are made in the middle of the mask, with an air gap of 0.05 mm.*

There is a pressing question, however, which needs some consideration. Are the soft magnetic materials more permeable and saturated than they realistically are? There are no easy answers to this question, nevertheless, it is possible to verify that the saturation of the masks do not exceed the limits in the magnetization curves, shown in Figure 4.2.

The magnetization saturation of both vanadium permendur and low carbon steel masks are found, using Equation 2.7, and shown as dotted lines in Figure **??**. The saturations are approximately 2.30 T, and 2.05 T for vanadium permendur and low carbon steel, respectively, consistent with the saturation in the magnetization curves of the materials, never exceeding the limits. The magnetic induction at the weak spots are also solely produced by the magnetization of the mask materials. Additionally, the saturation drops to zero inside the air gap. This is of course good news, and suggests that the simulations of these materials are, if not realistic, close to realistic.

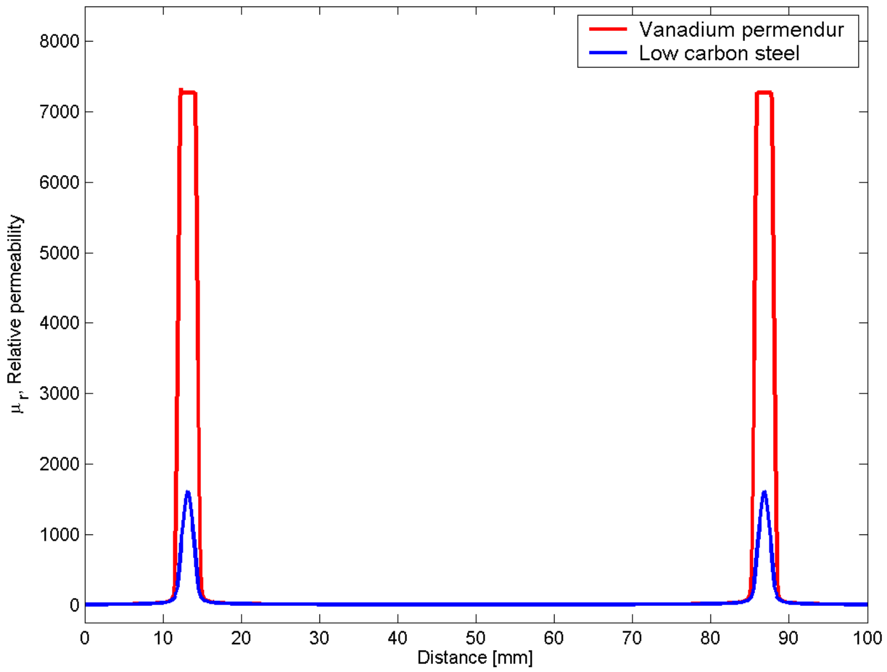

Figure 4.28: *Comparison of the relative permeability in the middle of vanadium permendur, and low carbon steel masks. The masks are 0.05 mm thick, and resting on top of NdFeB 42H permanent magnets with a magnetic remanence* B_r *= 1.32 T.*

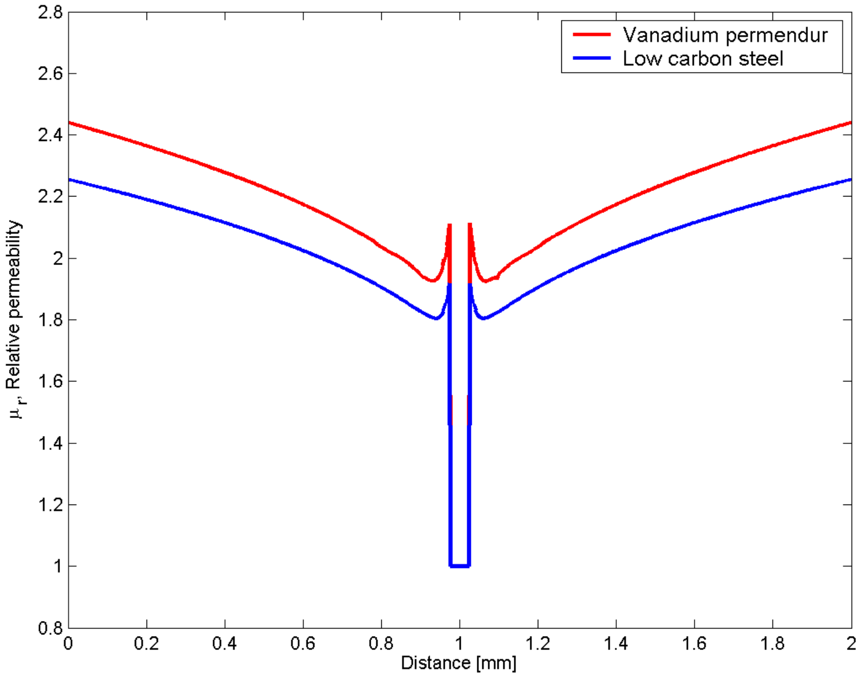

Figure 4.29: *Comparison of the relative permeability around the air gap in the middle of vanadium permendur and low carbon steel masks. The masks are 0.05 mm thick, and resting on top of NdFeB 42H permanent magnets with a magnetic remanence* B_r *= 1.32 T.*

4.3 Summary and discussion

The magnetic force, acting on magnetic and non-magnetic particles, is proportional to the magnetic susceptibility (χ) of the substance, the magnetic induction ($\mathbf{B}$), and the gradient of the applied magnetic field ($\nabla\mathbf{B}$). Establishing a connection between $\mathbf{B}\nabla\mathbf{B}$, mask thickness, gap size, soft magnetic, and permanent magnet material is therefore essential, in order to determine an optimal configuration of the design, where the goal is to increase the magnetic separation capacity of the newly designed device.

Numerical studies of the theoretical approximations to half open Kittel domains, when corrected for a 15% overestimation of the tangential field in the immediate vicinity of point O, estimate $\mathbf{B}\nabla\mathbf{B}$ values on the order of 10^9 mT^2/m. The corrected theoretical distributions match the simulations, and do not exceed the results derived for half open Kittel domains in [6].

Simulations show that, adding 0.05 mm thick vanadium permendur masks forming a gap of less than 0.10 mm on top of a half open Kittel domain increases the strength of the tangential field, in a distance of 0.01 mm, with a factor of up to 20% compared to an analog system, i.e., a structure without masks. The width of the peak in the tangential distribution is also narrower than in the corresponding analog structure. These results are consistent with what is obtained by Il'yashenko *et al.* in [5].

Further analysis show that, $\mathbf{B}\nabla\mathbf{B}$ increases compared to that in the corresponding analog structure, when the mask thickness and gap size decrease from 1.00 mm and down to 0.05 mm, until it reaches a maximum value in the range of 10^{10}-10^{11} mT^2/m, depending on what distribution the gradient is obtained from. Distributions 20.00 mm between the end points around the center compared to 2.00 mm produce less noise, but lowers the value of the gradient. The noise is suppressed when the distance increases, connected to that fact that, local numerical instabilities, caused by discontinuities in permeability and field values, are smoothed out and disappears. However, as the distance increases, the distributions are less accurately described, consequently lowering the value of the gradient. The results of 10^{11} mT^2/m, obtained for 2.00 mm distributions in a distance of 0.01 mm to the masks are, regardless of noise, comparable to what is obtained in [5]. In any case the simulations predicts that, $\mathbf{B}\nabla\mathbf{B}$ is increased at least a factor of six compared to the analog structure in a distance of 0.01 mm to the masks, regardless of distance between the end points.

The singularities in the demagnetization field around the sharp corners of the masks, contributing to the increase of the tangential field, merge together to form one when the gap size decreases below approximately 0.10 mm. The merging consequently "pushes" the tangential distribution upwards, adding to the total magnetic induction of the peak, and the width of the peak narrows. Above this gap size, however, the strongest gradients are no longer positioned in the center of the gap, but governed by the location of the mask corners, with values of $\mathbf{B}\nabla\mathbf{B}$ in the range of 10^{10}-10^{11} mT^2/m, and approaching analog values of 10^9 mT^2/m in the center of the gap. Simulations additionally show that in distances larger than a *critical* distance of 40 μm, the singularities in the demagnetization field disappear. The masks now decrease the magnitude of the field, since the absolute distance to the magnets is increased, and the distribution profile of $\mathbf{B}\nabla\mathbf{B}$ converge towards the analog distribution, with maximum values depending on the thickness of the masks.

As a consequence, the device has the ability to control the position of the gradient maxima and minima by adjusting the gap size. The singularities at the mask corners, however, are produced in demagnetization fields near ideal square edges, and precisely controlling the shape of these corners in real devices is difficult. Additionally, when the gap size is smaller than 0.10 mm, the gradient maxima and minima is a result of two singularities merging in the tangential field. For these particular reasons the simulations strongly suggest using gap sizes below 0.10 mm, in order to focus the separation in the center of the gap for and additive effect.

The device is able to produce an extremely strong magnetic field gradient several times stronger than in the analog system, owing to the fact that, most of the dependency in $\mathbf{B}\nabla\mathbf{B}$ lies in the shape the magnetic stray field. The z-gradient of $\mathbf{B}$ opposes the x-gradient, nevertheless, B_x is larger than B_z, thus $B_x(\nabla B)_x$ is the dominating contributor to the magnetic force. Future work should thus be motivated towards narrowing the field distribution even further. This will only slightly increase the value of the tangential field, but drastically increase the gradient, however, both contributing to increasing the magnetic force.

Additional study show that, the strength of the magnetic stray field is proportional to the coercivity of the permanent magnets, while $\mathbf{B}\nabla\mathbf{B}$ is proportional to the square of the coercivity. Furthermore, $\mathbf{B}\nabla\mathbf{B}$ is proportional to the saturation of the masks *if* the distance to the masks is less than the critical distance. As a result, producing new and better compounds will increase the effectiveness of the newly designed device even further.

The gradient is focused in a small volume, thus producing intense magnetic forces with short ranged action. This is of great interest, not only for separation of nanoparticles or biological materials like blood cells and DNA, but also for making magnetic recording heads, able to magnetize high coercivity storage media ($H_c = 0.35 - 1.15$ MA/m), where the objective is to manipulate single electrons at a time. The active element in recording heads thus needs to be as small as possible.

As a concluding remark, the results throughout this chapter are based on models with perfectly square edges and ideal adjoining surfaces between materials, difficult to obtain in real devices. The results, derived from theory and simulations, are thus likely to be larger than the corresponding experimental measurement of the device.

Chapter 5

Experimental study

How credible are the theoretical approximations and the results obtained in the simulations? In order to answer these questions, the magnetic stray field is experimentally measured on a model of the system.

Unfortunately, equipment for measuring strong magnetic fields with the presicion we would like is not available to us. We therefore, to the best of our knowledge, made a tool in collaboration with the electronics department at IFE, able to measure the stray magnetic field on the model in a distance of 1.75 mm above the surface of the masks.

5.1 The Hall effect and Lorentz force

The magnetic field is measured using small semiconductors, exploiting a natural phenomena called the Hall effect. The basic physical principle underlying the Hall effect is the Lorentz force. When a carrier moves along a direction perpendicular to an applied magnetic field it experiences a force, acting normal to both the motion of the carrier, and the applied magnetic field. In the semiconductor shown in Figure 5.1 the carriers are predominately electrons, moving with a constant current in the presence of a perpendicular magnetic field (**B**). Electrons subject to the Lorentz force drifts away from the current line towards the left side of the bar, leading to an excess surface electrical charge on that side. The result is a potential drop across the two sides, known as the Hall voltage. This transverse voltage obeys the expression $V_H = IB/qnd$, where I is the current, d the sample thickness, n the bulk carrier density, and q the elementary charge [27].

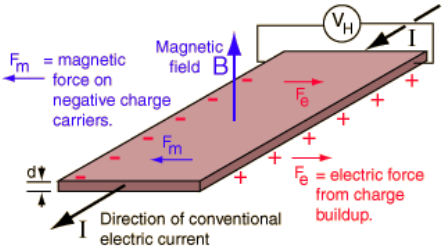

Figure 5.1: *Principle behind the Hall effect in a semiconductor.*

5.1.1 Hall effect sensors

It is imperative that the probes used in the experiments are as small and thin as possible, in order to measure the magnetic stray field as close as possible to the surface of the masks, where it is the strongest. Furthermore, the active sensors must be able to operate linearly in very high magnetic flux density ranges, for accurate measurements of the field. Note that, when referring to a probe it is understood as the branded surface encasing a small active semiconductor Hall element sensor, i.e., the probe is *not* the sensor.

Figure 5.2 and 5.3 show two different probes used in the experiments, both made by Chen Yang Technologies[1].

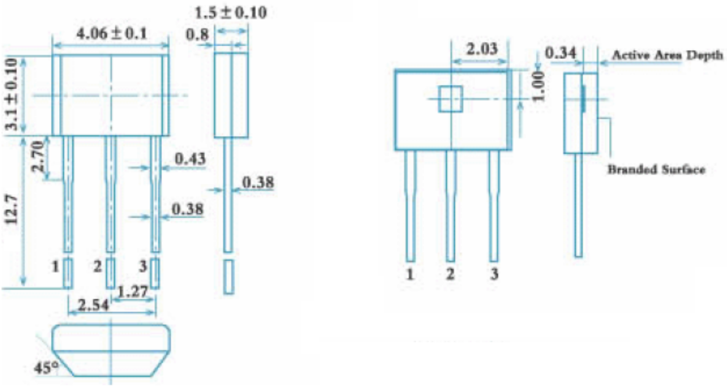

Figure 5.2: *Schematic drawing of a CYL49E probe, whose Hall effect sensor is used to calibrate a CY-P15A Hall effect sensor. Pin 1 is connected to a 5.00 V power supply, pin 2 to ground, and pin 3 provides Hall voltage output. All length scales in millimeters.*

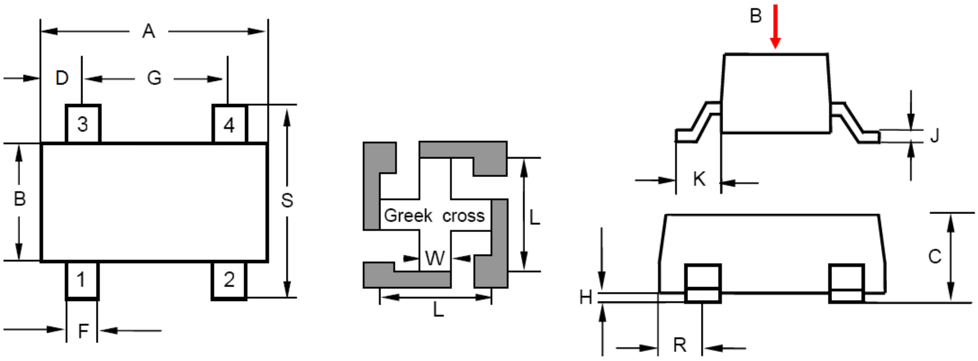

Figure 5.3: *Schematic drawing of a CY-P15A probe (left and right), used in order to measure the magnetic stray field. Pin 1 is connected to an input current no larger than 1.50 mA, pin 2 and 4 to ground, and pin 3 provides Hall voltage output. The middle picture shows the active Hall effect sensor area, situated in the center of the probe. The grey areas are ohmic contacts, while the active sensing area is the white cross, known as a Greek cross. Table 5.1 shows specifications of SOT 143 package and Greek cross dimensions, i.e., characteristic CY-P15A probe, and sensor length scales.*

---

[1] Company specializing in permanent magnets, soft ferrite cores, measuring instruments as well as Hall effect sensors. `http://www.chenyang-ism.com/`

	Min. dim. [mm]	Max. dim. [mm]
A	2.8	3.04
B	1.2	1.39
C	0.89	1.14
D	0.45	0.60
F	0.39	0.50
G	1.78	2.03
H	0.013	0.10
J	0.08	0.15
K	0.46	0.60
R	0.45	0.60
S	2.11	2.48
L	0.21	0.21
W	0.07	0.07

Table 5.1: *Minimum and maximum dimensions of the SOT 143 package encasing a Greek cross Hall effect sensor.*

The SOT 143 package, encasing the CY-P15A Hall effect sensor, is the smallest probe we could find with satisfactory specifications of the active sensor. The sensor operates linearly in a magnetic field ranging, from 0.10 μT to 2.00 T. Unfortunately, it is not calibrated. A CYL49E sensor with a characteristics curve as in Figure 5.4, is thus used to calibrate the CY-P15A sensor. It requires a 5.00 V constant power source in order to operate with outputs changing linearly with the magnetic flux density of the input ,in a confirmed range of -90.0 mT to 90.0 mT.

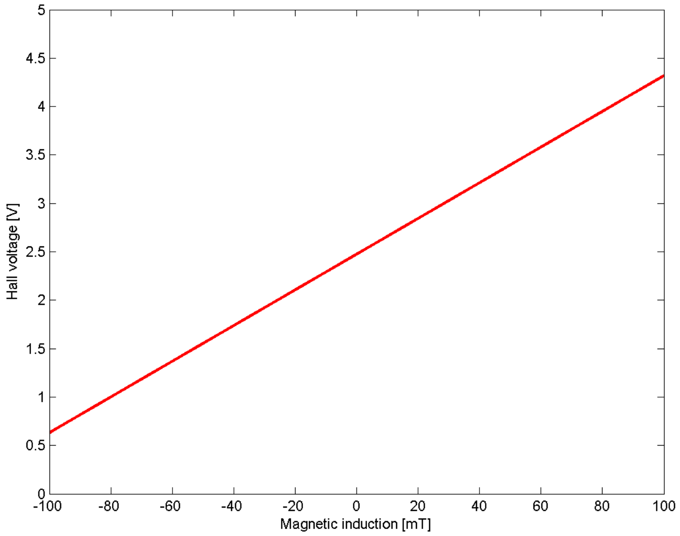

Figure 5.4: *Characteristics curve of a CYL49E Hall effect sensor, as listed by ChenYang Technologies GmbH & Co. KG. The sensor operates linearly in a range of -90.0 mT to 90.0 mT*

5.2 Implementation and design

The measurements are performed in a controlled environment, where the positions of the probes are governed with micrometer precision. Furthermore, in order to minimize disturbances in electronic equipment, possibly sensitive to magnetic fields, the setup is designed to ensure that most of the electronics are located far away from the magnets themselves. The result is an experimental setup as in Figure 5.5.

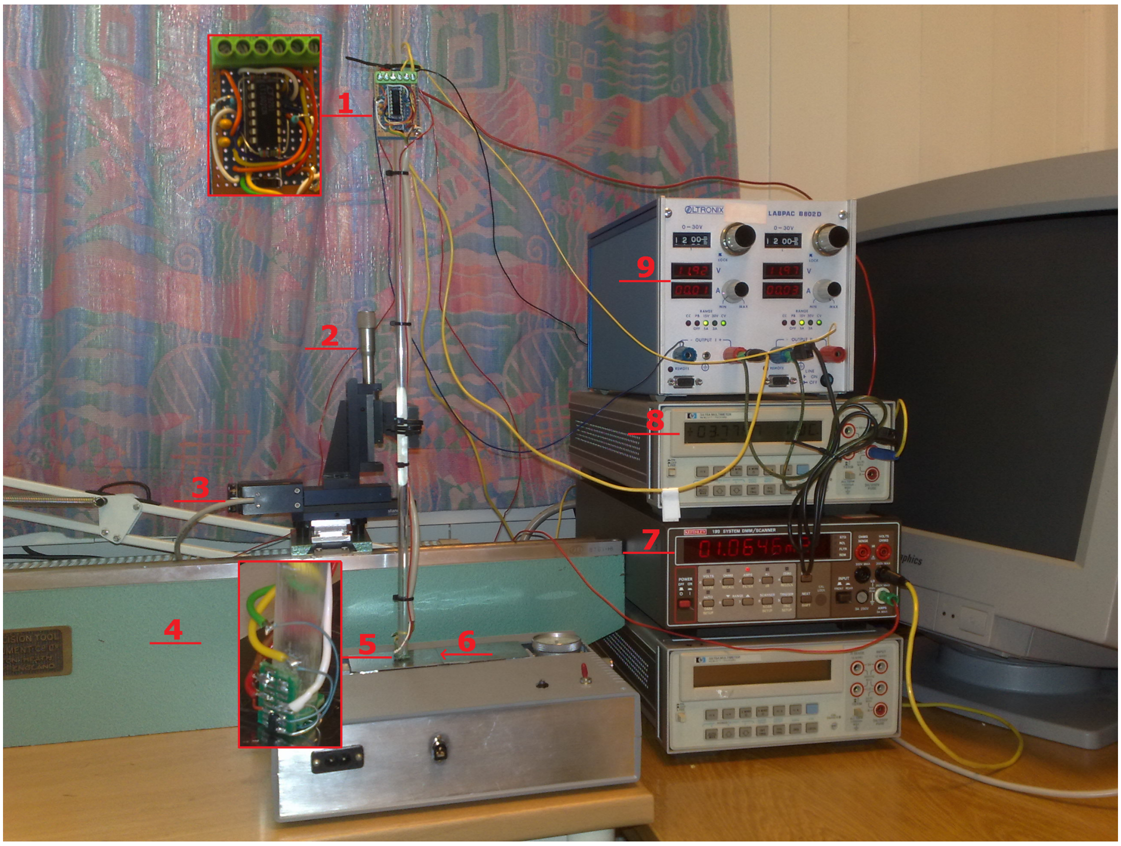

Figure 5.5: *The complete experimental setup of all equipment except the power source supplying the sensors with constant current. In ascending order:* ***1.*** *Operational amplifier soldered onto a circuit card. The box encased in red shows a close up of the amplifier.* ***2.*** *Manual translation stage adjusting the position in the z-direction.* ***3.*** *Motorised translation stage adjusting the position in the x-direction.* ***4.*** *Heavy work bench on which the translation stages are mounted.* ***5.*** *Two CY-P15A probes mounted at the tip of a long plastic rod, whose sensors measures the magnetic field. The box encased in red shows a close up of the tangential probe. The normal probe is located underneath the end of the glass rod, thus not visible.* ***6.*** *Small gap in the masks above the magnets.* ***7.*** *Multimeter, monitoring the current through the sensors.* ***8.*** *Multimeter, monitoring the Hall voltage output.* ***9.*** *Power supply unit (PSU) supplying the operational amplifier with ±12.0 V.*

The two CY-P15A probes are soldered onto two printer cards mounted at the tip of a long plastic rod. The wires from the sensors are pulled up along the rod, and connected to an operational amplifier on a small circuit card. A detailed circuit diagram of the connection between the sensors and the operational amplifier is shown in Figure 5.6.

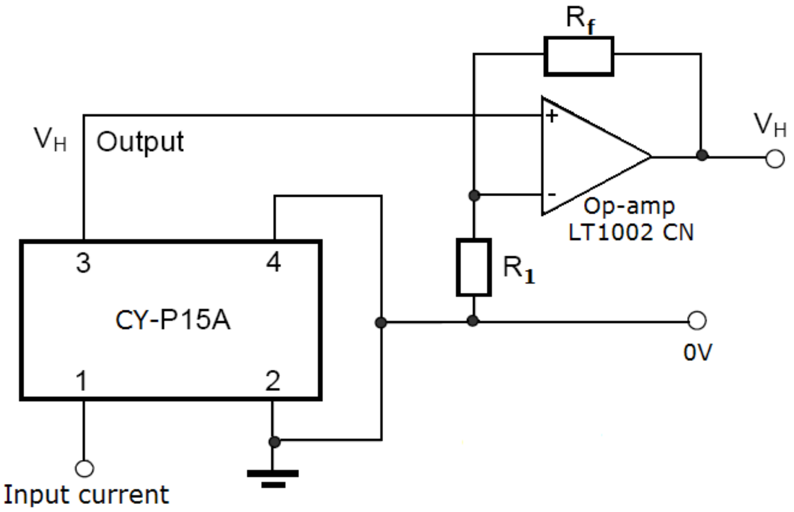

Figure 5.6: *Circuit diagram of a CY-P15A Hall effect sensor, where pin 1-4 are connected to the four ohmic contact points on the Greek cross. A LT1002 operational amplifier (op-amp) is further connected to the sensor in the non-inverting amplifier configuration. The input signal is applied to the non-inverting input (+) of the op-amp. The feedback, on the other hand, is taken from the output of the op-amp via a resistor (R_f) to the inverting input (-) of the op-amp, where another resistor (R_1) is taken to ground. As the signal moves in either direction, the output will follow in phase to maintain the inverting input at the same voltage as the non-inverting input. The result of this circuit is a device which can amplify signals, without inverting the polarity of the original input voltage. The voltage gain is always more than 1, and is worked out from $V_{gain} = (1 + \frac{R_f}{R_1})$. In this case resistors R_1 and R_f are equal to 1.0 kΩ and 2.7 kΩ, respectively, thus $V_{gain} = 3.7$.*

In order to improve the sensitivity of the sensors, thus increasing the resolution in the measurements of the magnetic stray field, a LT1002 dual matched precision operational amplifier is connected to the sensor, increasing the Hall voltage output with a factor of 3.7. The amplifier is produced by Linear Technology[2], and has an insignificant maximum offset voltage of 100 μV.

The position of the probes are governed by a motorised translation stage with an accuracy of 1.25 μm in the x-direction, and a manual translation stage with an accuracy of 10.0 μm in the z-direction. The translation stages, depicted in Figure 5.7, are assembled together and tightly fastened onto a heavy work bench, in order to prevent unwanted movement of the probe heads during the measurements. The motors are produced by Standa[3], an opto-mechanical manufacturer.

The operational amplifier is supplied with ±12.00 V, while the CY-P15A Hall effect sensors are supplied with a constant current of 1.06 mA, thus safely within operational limits. The Hall voltage output is monitored by a multimeter, delivering the data to a PC through a GPIB[4] bus interface.

---

[2] Company specializing in designing, manufacturing, and marketing a broad line of standard high performance integrated circuits. `http://www.linear.com/`

[3] Company specializing in developing motorised and manual translation and rotation stages, as well as motion controllers. `http://www.standa.lt/`.

[4] Eight bit general purpose interface bus, originally created for use with automated test equipment.

Figure 5.7: *Translation stages, governing the position of the probes in the x (left) and z-directions (right). The device to the left is a motorised 8MT173-50 model, while the device to the right is a 7T173-25 model, which adjusts the position manually.*

5.2.1 LabVIEW and data processing

National Instrument's Laboratory Virtual Instrumentation Engineering Workbench (LabVIEW)[5] is a virtual environment tool, enabling users to develop applications which includes receiving data through dasy-chained GPIB bus interfaces in automated measurements, and controlling instruments. LabVIEW is executed in sequence, step by step performing commands in pre-programmed subroutines, called virtual instruments (VI). Each instrument has three components: a block diagram, a front panel, and a connector panel. The block diagram is a set of function-nodes wired together, where information propagates through the wires, and a node executes as soon as all its input data becomes available. The front panel is a graphical interface for entering initializing values and parameters, as well as for starting and stopping routines. Lastly, the connector panel enables users to connect different VI's together.

For this particular experiment, LabVIEW is used to operate the motorised translation stage, governing the position of the probe in the x-direction, as well as recording Hall voltage outputs acquired from multimeters. Appendix C.1 contains a detailed block diagram of a VI instrument, performing these tasks in the experiments.

5.2.2 Calibration of CY-P15A sensors

Placing a CYL49E sensor inside weak and uniform magnetic fields yields Hall voltages that are compared to its characteristics curve, thus obtaining the field strength at those points. The field is then measured again, at the exact same points with a CY-P15A sensor. The outputs are compared to the field strength already found, thus obtaining a magnetic flux density versus Hall voltage characteristics curve for that CY-P15A sensor.

The calibration is performed on two weak magnets, producing relatively uniform magnetic fields. The magnetic field must be weak in order to not exceed the limit, above which the CYL49E sensor is no longer linear. Furthermore, by relatively uniform, it is understood that the magnetic field does not change considerably over distances, comparable to the uncertainty in the thickness of the branded surface encasing the sensors, which in all cases is very close to ± 0.10 mm.

---

[5] `http://www.ni.com/labview/`

According to Table 5.1 and Figure 5.2, the difference in thickness between a CYL49E and CY-P15A probe is 0.54 mm. Furthermore, assuming that the active Hall elements are point sensors, thus disregarding the size of the elements themselves and assuming they are positioned in the center in all spatial directions, the CY-P15A sensor sits 0.27 mm closer to the surface of the probe, compared to the CYL49E sensor.

The calibration is performed 0.75 mm and 6.50 mm above the surface of the magnets. The difference in distance from sensor to probe-surface is taken into account, by measuring the magnetic field 0.27 mm further away from the magnet with the CY-P15A probes, equal to 216 steps â 1.25 μm with the motorised translation stage. Figure 5.8 shows the calibrated characteristics curve obtained for both CY-P15A sensors. The experimental data producing the curves is listed in Appendix D.1-D.3, while Appendix B.4 contains a MatLab script used to process the data.

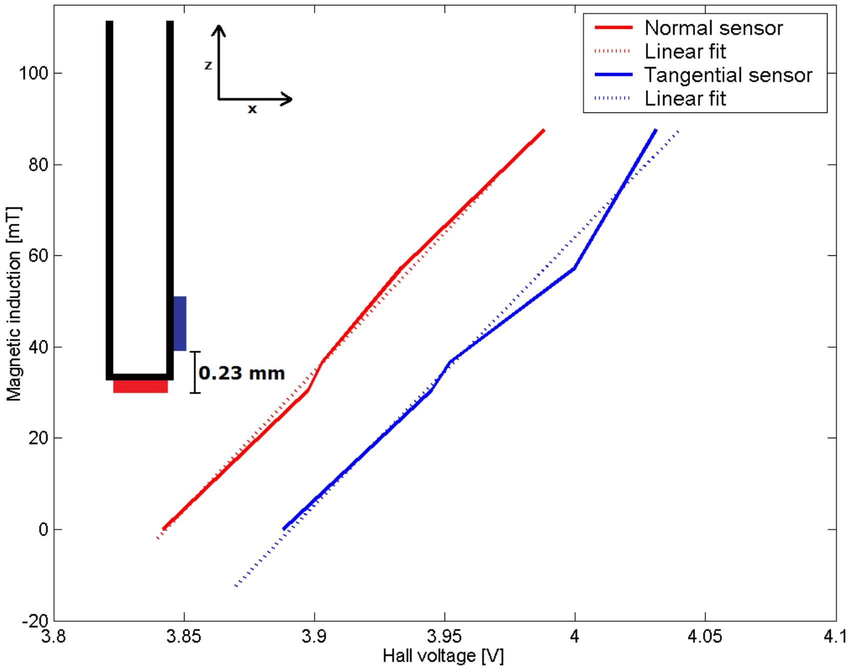

Figure 5.8: *Two calibrated characteristic curves, obtained for the two CY-P15A Hall effect sensors used in the experiments. The linear fits are produced in MatLab, and yields two equations computing the magnetic induction for a specific Hall voltage. The inlet figure (upper left) shows the corresponding tangential probe (blue), and normal probe (red) mounted at the plastic rod in such way that, the distance from the lower edge of the tangential probe to the surface of the normal probe is 0.23 mm.*

The calibrated equations for the tangential and normal CY-P15A sensors, where x is the measured Hall voltage and y the magnetic induction are

$$y_{tangential} = 587.16\frac{mT}{V} \times x - 2284.6mT \tag{5.1}$$

$$y_{normal} = 608.02\frac{mT}{V} \times x - 2336.7mT. \tag{5.2}$$

5.3 Results

The model, upon which the experiments are performed, consists of two giant magnetic anisotropy neodymium-iron-boron permanent magnets of dimension $50\times50\times25$ mm^3, coercivity $H_c = 955$ kA/m, and magnetic remenance $B_r = 1.30$ T. The magnets rest on a base made of low carbon steel, and on top of the magnets there are two 0.30 mm thick masks, also made of low carbon steel.

The probes are positioned perpendicular to the x and z-component of the magnetic field in $y = 0$. The surface is sweeped 20.0 mm in the x-direction, in steps of 0.05 mm over a gap approximately 0.10 mm wide. Note that, all coordinates are relative to the axis in Figure 3.1. According to Figure 5.8, the minimum obtainable distance between the bottom edge of the tangential probe to the surface of the masks is 0.23 mm. Thus, still assuming that the active Hall elements inside the probes are positioned in the center in all spatial directions, disregarding the size of the elements themselves, the tangential field is measured no closer than 1.75 mm to the surface of the masks.

5.3.1 Magnetic stray field distribution comparisons

Figure 5.9 and 5.10 show the tangential and normal distribution of the magnetic stray field, respectively, measured 1.75 mm above the masks together with theoretical approximations and simulations. Appendix D.3-D.4 contain all Hall voltage experimental data, that in combination with Equation 5.1-5.2, produce the distributions.

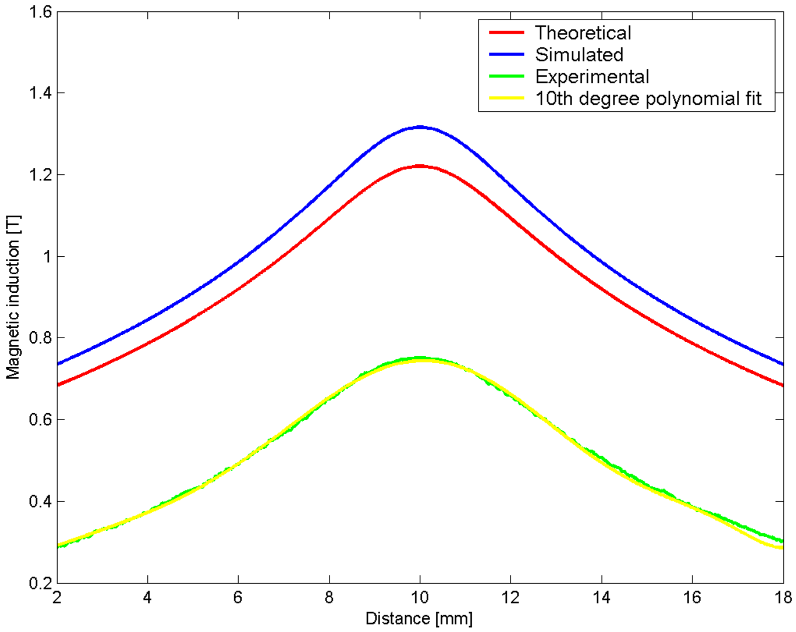

Figure 5.9: *Comparison of theoretical, simulated, and experimental tangential magnetic stray field distributions (B_x), 1.75 mm above the surface of 0.30 mm thick low carbon steel masks with a gap size of 0.10 mm. The 10th order polynomial fit to the tangential distribution is used to calculate the gradient of the field. Note that, the theoretical approximation is obtained for a system without masks.*

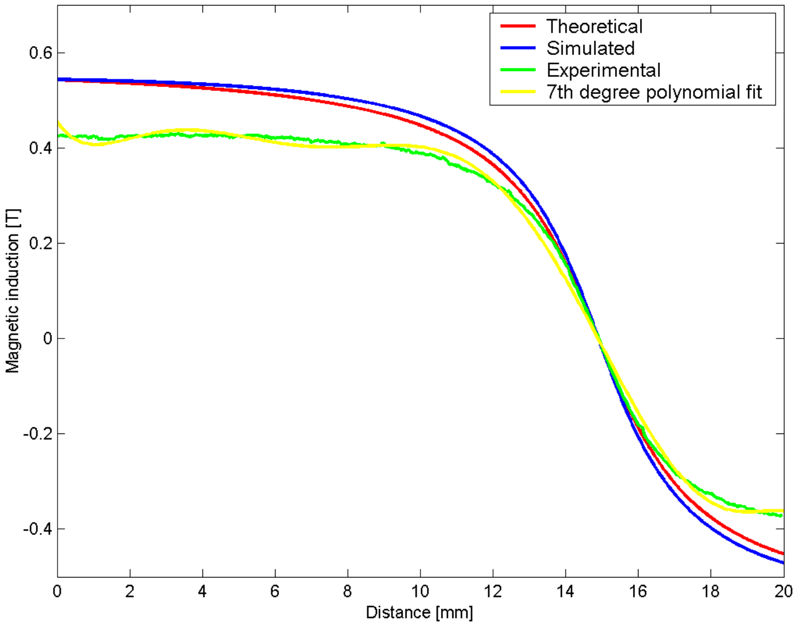

Figure 5.10: *Comparison of theoretical, simulated, and experimental normal magnetic stray field distributions (B_z), 1.75 mm above the surface of 0.30 mm thick low carbon steel masks with a gap size of 0.10 mm. The 7th order polynomial fit to the normal distribution is used to calculate the gradient of the field. Note that, the theoretical approximation is obtained for a system without masks. Furthermore, the experimental distribution is adjusted for a -50 mT error due miss-match in Hall voltage offsets between calibration and experiment. The offset is most likely caused by the multimeter.*

The theoretical approximations to the magnetic stray field assumes no masks, thus strictly not comparable to the simulations. Nevertheless, the field is calculated 1.75 mm above the masks and, according to the simulations in Chapter 4, the singularities at the corners of the masks are no longer detectable, cf., Figure 4.18-4.19, thus behaving much like the field in an analog structure. The only difference is that the masks now act as magnetic screens, consequently decreasing the difference in magnetic induction between simulation and theory, relative to that in the corresponding analog structure, cf., Figure 4.4. Note that, closing in on $x = 0$ in the tangential distribution the difference is actually increased, owing the fact that there are no masks here, while at the same time, since $z > 1$, the theoretical approximation is no longer as accurate. The second term in Equation 3.1 now gives negative contributions, thus predicting to low values. Nevertheless, the theoretical and simulated distributions are comparable.

Most important, however, is that the experimental, tangential, and normal field distributions match the shape of the theoretical approximations as well as the simulations, suggesting gradients on the same order. There is, however, a considerable deviation in magnetic induction, especially in the tangential distribution.

A likely cause for some of the deviation arises from the fact that, the magnetic field is not measured at singular points in space assumed so far. In reality, the active sensor element inside the probe head extends 0.21 mm in the y and z-directions. In a uniform magnetic field this will not cause any problems, however, in this case the field is very inhomogeneous, thus altering the physics of the Hall effect sensor response.

The response to a spatially dependent magnetic field is studied in [28]. Starting from the analytic expression of the response of a Greek cross shaped Hall sensor, to an ideal field dot as a function of its position, as proposed by Thiaville *et al.* [29], a simple formulation is found, allowing the deduction of the response of the sensor to any spatially inhomogeneous magnetic field. The results show that the sensor response has a limited full-width at half-maximum (FWHM), approximately equal to the length of the central part of the Greek cross. Due to spatial field averaging effect occurring over the sensor area, the overall sensitivity is lower than that expected from an ideal point sensor. However, their results show that this average is not equivalent to the simple field average taken over the effective area, especially very close to field sources.

The precise effect the altered Hall effect response has on the experimental data is thus somewhat unclear. The overall induction is, however, lowered because the field is not measured with an ideal point sensor. Moreover, the spatial averaging across the sensor most likely produce more loss of precision closer to the center of the gap, where the field changes more rapidly.

Further deviations in the magnetic induction may be connected to uncertainties in probe thickness in accordance with Table 5.1, distance between probe-surface and mask-surface, as well as perpendicularity between Hall effect sensors and the x and z-component of the magnetic field. Additionally, theory and simulations use permanent magnets with a remanence of 1.32 T, while the real model uses magnets with a remanence of 1.30 T. Furthermore, positioning the sensors in the y-direction is governed with hand-eye precision, ultimately increasing the total uncertainty. The magnetic stray field changes relatively little around the y-axis for small y, however, inevitable ever so slightly decreasing as $|y|$ increases.

In any case, $\mathbf{B}\nabla\mathbf{B}$ depends mostly on the altered shape of the field distribution, as established in Chapter 4. The shape of the experimental curves are comparable to the simulations and the theoretical approximations, thus suggesting that the gradients are on the same order.

5.3.2 B∇B distribution comparisons

Figure 5.11 and 5.12 show experimental $B_x(\nabla B)_x$ and $B_z(\nabla B)_z$ distributions, found directly from the green curves in Figure 5.9 and 5.10. The noise is most likely explained by the fact that, the field is measured in steps as small as 0.05 mm. The combined errors due to the sensors not being able to pick up subtle changes in magnetic field strength, spanning a distance of 0.05 mm, together with small "random" offsets in electronic equipment, produce local discontinuities in the tangential and normal distributions of the magnetic field. The local discontinuities, seen as "disturbances" in the experimental curves, transform into very noisy gradients since any gradient is extremely sensitive to rapid changes of its respective vector field. In any case, polynomial fits to the noisy distributions reveal shapes, which are recognizable from simulations as well as theory.

Figure 5.13 shows a complete comparison of theoretical, simulated, and experimental $B_x(\nabla B)_x$ and $B_z(\nabla B)_z$ distributions. The experimental distributions are obtained from the polynomial fits to the tangential and normal distributions of the magnetic stray field, seen as yellow curves in Figure 5.9 and 5.10.

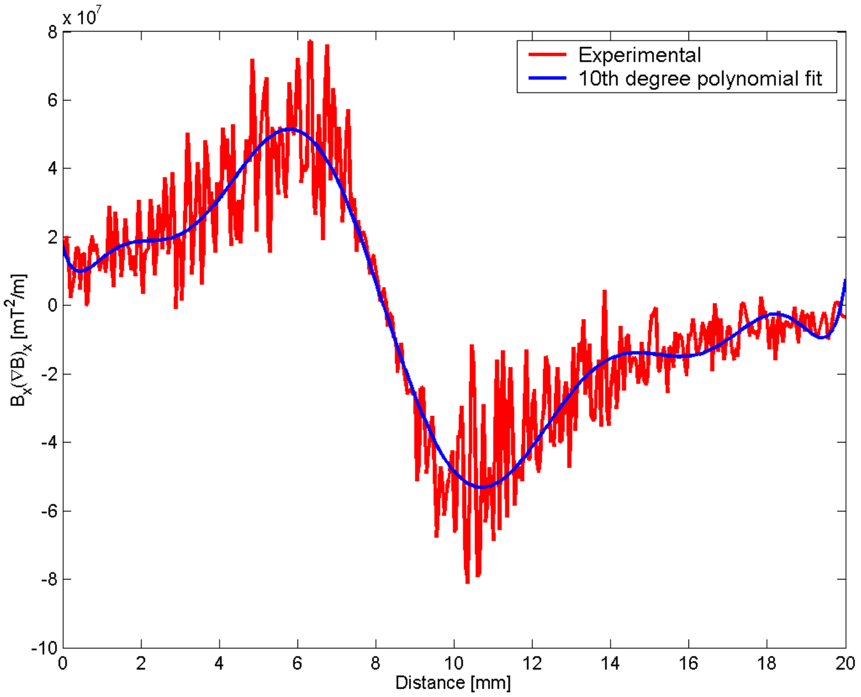

Figure 5.11: *Experimental* $B_x(\nabla B)_x$ *distribution 1.75 mm above the surface of 0.30 mm thick low carbon steel masks, with a gap size of 0.10 mm. The shape of the 10th order polynomial fit to the experimental data is recognizable from simulations. The center of the gap in the masks is approximately in 8.00 on the distance scale.*

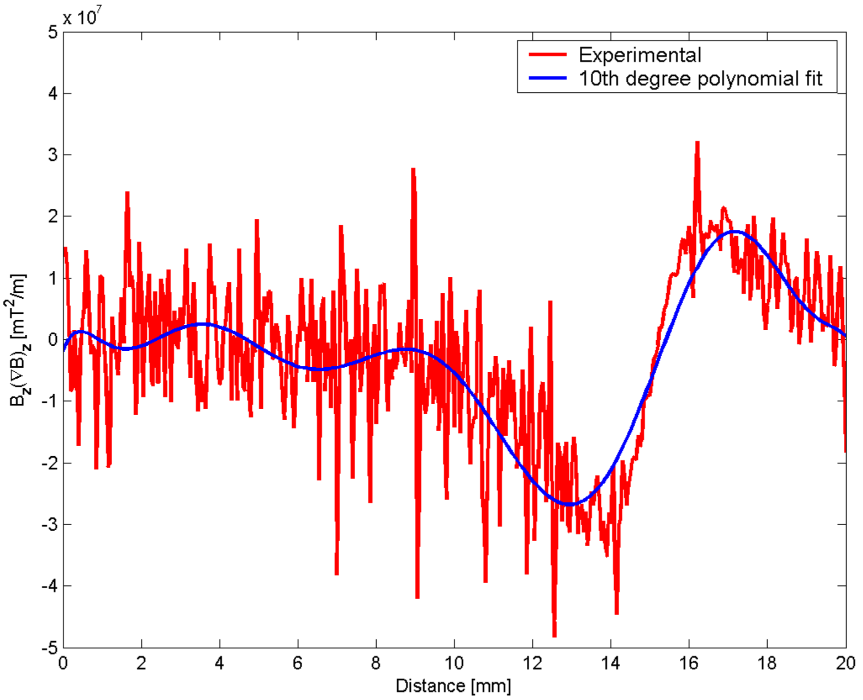

Figure 5.12: *Experimental* $B_z(\nabla B)_z$ *distribution 1.75 mm above the surface of 0.30 mm thick low carbon steel masks, with a gap size of 0.10 mm. The shape of the 10th order polynomial fit to the experimental data is recognizable from simulations. The center of the gap in the masks is approximately in 15.00 on the distance scale.*

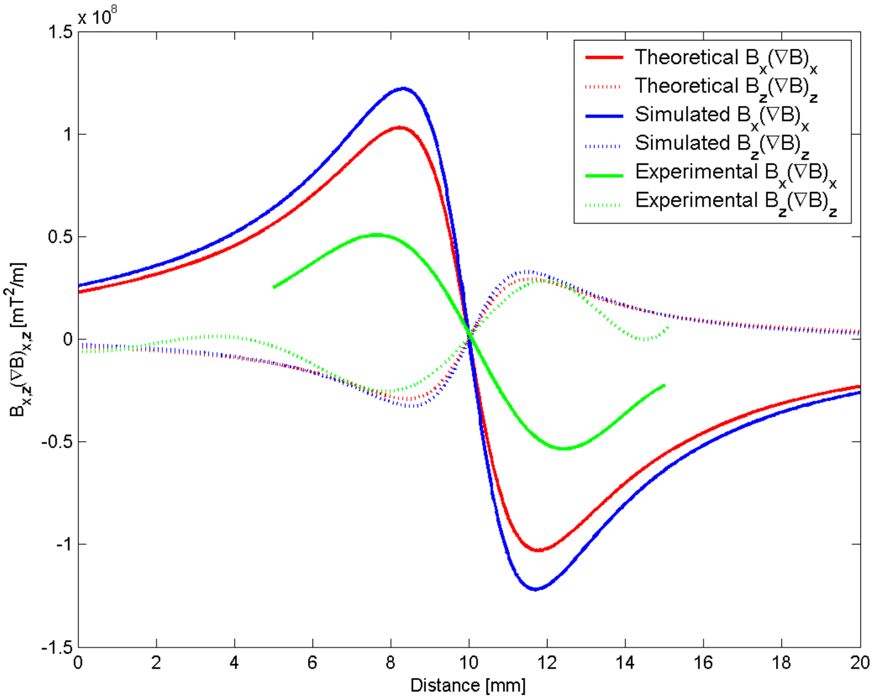

Figure 5.13: *Theoretical, simulated, and experimental $B_x(\nabla B)_x$ and $B_z(\nabla B)_z$ distributions 1.75 mm above the surface of 0.30 mm thick low carbon steel masks, with a gap size of 0.10 mm. The experimental distributions are obtained from the polynomial fits to the tangential and normal distributions of the magnetic stray field, cf., Figure 5.9 and 5.10.*

As explained in Figure 4.14, $B_x(\nabla B)_x$ and $B_z(\nabla B)_z$ are on the same order but oppositely directed, a behavior also observed in the experimental distributions. For the same reasons as in the previous section, theory is comparable to simulations, and experiments. Both experimental distributions match the corresponding simulated and theoretical distributions very well, and show clear signs of the same relative behavior as in the tangential and normal field distributions in Figure 5.9 and 5.10. The conclusion is, nevertheless, that the normal experimental distribution matches its corresponding simulated distribution better than what the tangential experimental distribution matches its corresponding simulated distribution. As discussed earlier, the Hall effect sensor response is altered in the very strong and inhomogeneous part of the field in the center of the gap. Since the tangential field, according to simulations, is roughly 2.3 times stronger than the normal field, the altered response has a much larger impact on the tangential field. The result is a less accurately described tangential distribution in the center of the gap, and the difference between simulated and experimental values increases relative to that further away from the gap, thus increasing the difference in the gradient accordingly. The experimental distributions also match the corresponding distributions in Figure 5.11 and 5.12, topping out at 10^7 mT^2/m.

Figure 5.14 shows the final and complete picture of theoretical, simulated, and experimental $\mathbf{B}\nabla\mathbf{B}$ distributions. The experimental distribution reaches a value of approximately 2.5×10^7 mT^2/m, 3.5 times lower than the simulated value. Comparing the experimental distribution to the simulated distributions in Figure 4.12 and 4.13, where $\mathbf{B}\nabla\mathbf{B}$ reaches values of approximately 3.00×10^9 mT^2/m and 1.75×10^8 mT^2/m, 0.10 mm and 1.00 mm above 0.30 mm thick masks, respectively, the experimental distribution supports the statement that **B∇B** decreases, close to linearly with increasing distance to the masks. This statement, however, assumes that the distance is larger than the critical distance, and does not verify the simulations in the regions where the singularities in the demagnetization field above the corners of the masks are detectable.

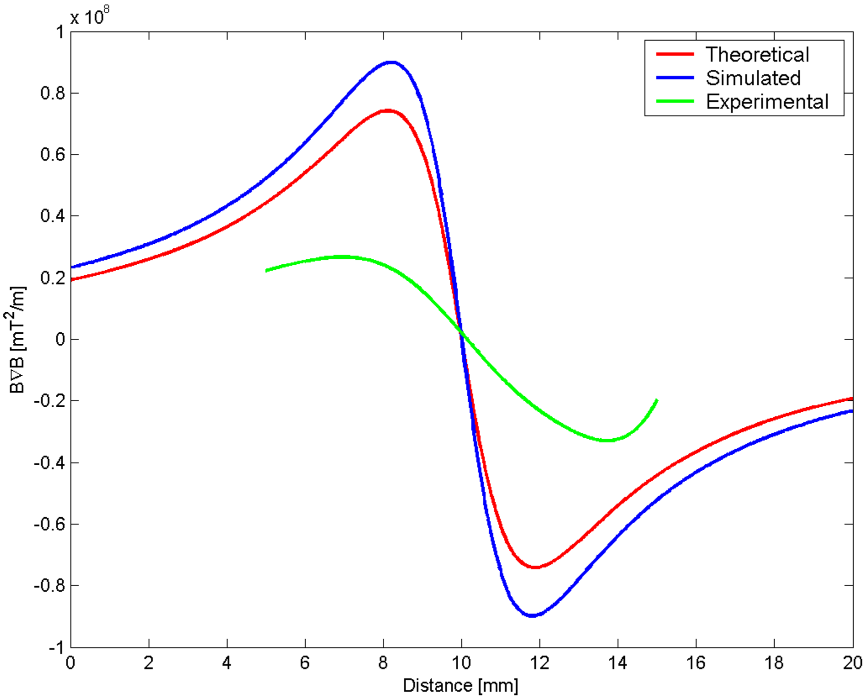

Figure 5.14: *Theoretical, simulated, and experimental* $\boldsymbol{B}\nabla\boldsymbol{B}$ *distributions 1.75 mm above the surface of 0.30 mm thick low carbon steel masks, with a gap size of 0.10 mm. The experimental distribution is obtained from the polynomial fits to the tangential and normal distributions of the magnetic stray field, cf., Figure 5.9 and 5.10. According to Figure 5.13, the experimental tangential and normal distributions only "coexist" between 5 and 15 on the distance scale. The distribution of* $\boldsymbol{B}\nabla\boldsymbol{B}$ *is thus only represented in this region. According to Figure 4.7, however, the distribution outside this region should converge towards the distribution in the simulation.*

5.4 Summary and discussion

Simulations show that the mask corners produce singularities in the magnetic field, detectable in distances less than 0.04 mm. The main problem with the experiment is that, the field can not be measured close enough to observe these singularities, owing to the thickness of the Hall effect probes. The full extent of the simulations from Chapter 4 can, thus not be verified. In any case, if the experiment is any indication, the reported magnetic field and **B∇B** distributions produced in simulations, are close to realistic in distances larger than the critical distance, with slightly overestimated values connected to the fact that, it is difficult to introduce ideal adjoining surfaces between materials in real models. On the other hand, all the uncertainties in perpendicularity between the Hall effect sensors and the x and z-component of the magnetic field, thickness of the probes, distance between probe-surface and mask-surface, position of probes in the y-direction, gap size, coercivity of magnets, and spatial averaging of Hall voltage output in the Greek cross Hall effect sensor suggests that, the magnetic field is stronger than what is really measured.

Measuring the magnetic field using a giant magnetoresistive (GMR) effect sensor, with a magnetic film of thickness less than 0.04 mm, is one possible solution to the experimental problem. GMR is a quantum mechanical effect observed in thin film structures, composed of alternating ferromagnetic, and non-magnetic layers. The effect manifests itself as a significant decrease in electrical resistance in the presence of a magnetic field. In the absence of an external magnetic field, the direction of magnetization of adjacent ferromagnetic layers is anti-parallel, due to a weak anti-ferromagnetic coupling between layers. The result is high-resistance magnetic scattering. When an external magnetic field is applied, the magnetization of the adjacent ferromagnetic layers is parallel. The result is lower magnetic scattering, and lower resistance [30].

As a concluding remark based on assumptions, a real model is most likely not able to produce $\mathbf{B}\nabla\mathbf{B}$ values, in a distance of 0.01 mm above the surface of the masks, exceeding 10^{11} mT^2/m. It is reasonable to assume that, the masks do indeed have a positive effect on the field, and gradient in distances less than the critical distance, but a more realistic suggestion places $\mathbf{B}\nabla\mathbf{B}$ in the region of 10^{10} mT^2/m, still several times the magnitude in an analog structure.

Chapter 6

Magnetophoresis

Magnetism and microfluidics have always been important concepts in physics. Recently, however, micro-electro-mechanical systems[1] (MEMS) techniques for fabrication of miniaturized magnets have gained attention, as it is anticipated that permanent magnet structures can be integrated into microfluidic analysis systems.

The concept of particle separation have historically been dominated by dielectrophoresis, electric manipulation of polarizable particles, in applications like capillary electrophoretic separations, electroosmotic pumping, and dielectrophoretic trapping [31, 32, 33], despite the great advantages applications based on magnetic fields offers. Externally applied magnetic fields can manipulate particles inside a microfluidic channel without direct contact with the fluid itself. Bead manipulation, where bio-material is attached to small but highly magnetic particles, makes it possible to isolate certain types of material from the rest of the sample. Additionally, magnetic interactions are generally not affected by external factors like surface charges, pH, or temperature, all common problems in electrophoresis. Furthermore, magnetic forces are no longer restricted to manipulation of highly magnetizable particles, like ferrofluids, but can even be used to manipulate non-magnetic material, e.g., diamagnetic objects as demonstrated in [34] with the levitation of a frog.

6.1 Magnetic separation techniques

Today there is an on-going effort to miniaturize traditional laboratory functions in lab-on-chip devices, i.e., the integration of functions by means of MEMS techniques onto chips. Functions like transportation, positioning, mixing, separation, and sorting of magnetic, as well as non-magnetic particles, are made automatic and compatible with the physics of fluid flows on microfluidic scales. Miniaturization of lab-on-chip devices offers two things: a fast and highly efficient separation, because the magnetic force on a particle is higher, the closer it is to the magnet surface. Secondly, meeting the growing demand for small devices, able to work efficiently with nano-sized particles.

Magnetic forces and microfluidics are combined in a myriad of ways, all offering different techniques and methods for separation, e.g., high gradient magnetic separation

---

[1] Micro-electro-mechanical systems is the integration of mechanical elements, sensors, actuators, and electronics, on a common silicon substrate through micro-fabrication technology.

(HGMS) techniques, often performed in tubes or capillaries, separating magnetic particles or cells [35, 36, 37]. Field-flow fractionation (FFF) [38, 39, 40], and split-flow thin fractionation (SPLITT) [41, 42, 43] are effective methods for separation of micro-particles in continuous fluid flows, in which several forces, such as gravity, thermal, electric, or magnetic fields, and gradients are combined. Magnetic field-flow fractionation was first demonstrated by Vickrey and Garcia-Ramirez [44], and Figure 6.1 shows the principle of FFF and SPLITT.

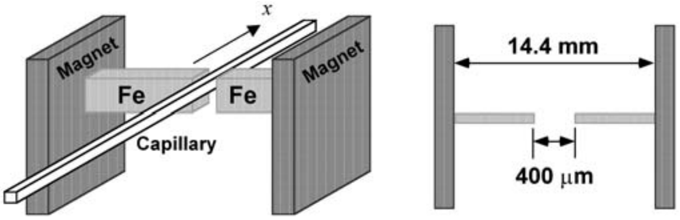

Figure 6.1: *Schematic drawing of the configuration of the magnets and the pole pieces in the capillary magnetophoresis of FFF and SPLITT fractionation, first demonstrated by Vickrey and Garcia-Ramirez.*

Based on FFF and SPLITT separation methods, a continuous flow method, capable of separating magnetic particles from non-magnetic, as well as separating different magnetic particles from each other, is termed on-chip free-flow magnetophoresis [45]. Laminar flow is generated over a flat separation chamber by a number of inlet and outlet channels, as seen in Figure 6.2.

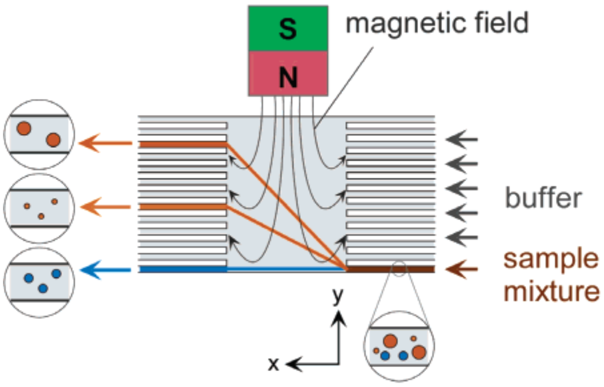

Figure 6.2: *Principle of free-flow magnetophoresis. Magnetic particles are pumped into a laminar flow chamber where a magnetic field is applied perpendicular to the direction of flow. Particles deviate from the direction of laminar flow according to their size and magnetic susceptibility, and are therefore separated from each other, and from non-magnetic material [45].*

Perpendicular to the direction of laminar flow, i.e., in the y-direction, an inhomogeneous magnetic field is applied, which forms a magnetic field gradient over the separation chamber. A mixture of magnetic and non-magnetic particles is injected continuously into the system, through the sample inlet channel. The non-magnetic particles are not influenced by the magnetic field, and leave the chamber at the exit, opposite the sample inlet. Paramagnetic and ferromagnetic particles, however, are dragged into the inhomogeneous magnetic field, leaving the chamber via one of the other outlet channels. Their deflection depend on the susceptibility and size of the particle, and can be studied in a microscope.

The device studied in this thesis produces extremely intense magnetic forces in very small volumes. This makes it perfectly suitable for magnetic and non-magnetic separation purposes in ever smaller environments, and has the potential to significantly improve applications based on magnetophoresis. It is especially interesting in combination with on-chip free-flow separation. The device is based on rare-earth magnets, and as a result can be integrated in microfluidic systems using MEMS techniques. In any case, an understanding of the magnetic forces and how they interact with the surroundings is essential, in order to optimize the magnetophoresis techniques. The next sections, thus outlines one approximation to the magnetic force on objects in hydrodynamic fluid flows.

6.2 Force on a magnetized object

The literature contains a multitude of slightly different expressions for the magnetic force on an object, all based on different assumptions and approximations. One of the most common notation states that, under the influence of a magnetic field ($\mathbf{B}$) the magnetic potential energy (U) of a particle with volume V, and volume magnetic susceptibility χ_p is written as

$$U = -\frac{\chi_p - \chi_m}{2\mu_0} V\mathbf{B}^2, \tag{6.1}$$

where μ_0 is the magnetic permeability of vacuum, and χ_m is the volume magnetic susceptibility of the medium. The magnetic force acting on a particle is consequently described by

$$\mathbf{F}_{mag} = -\nabla U = V\frac{\triangle\,\chi}{\mu_0}\mathbf{B}\nabla\mathbf{B}, \tag{6.2}$$

thus depending on the volume of the particle, difference in magnetic susceptibility between the particle and the surrounding buffer medium, as well as the strength and gradient of the applied magnetic field [21]. Note that, $\triangle\,\chi$ is the effective volume susceptibility, and includes the demagnetization factor of the particles.

This result assumes spherical particles and homogeneous properties of the medium and the particles. Moreover, interactions that come about when there are more than one particle present are disregarded; The field due to magnetization of one particle induces an additional magnetic moment in other particles, gives rise to an inhomogeneity of the field at the position of the other particles and thus a force, and an additional magnetic moment interacts with the dipole field of neighbouring particles. Nevertheless, it is generally a good approximation for the magnetic force on particles in magnetic fields. Note that, in a homogeneous field, i.e., a field where $\nabla\mathbf{B} = 0$, the force on the particle is zero. As a consequence, the particle will be magnetized but not pulled in any direction.

6.2.1 Susceptibility of particle and carrier medium

The difference in magnetic susceptibility between a particle and its surrounding buffer, or medium is termed $\triangle\chi = \chi_p - \chi_m$. For diamagnetic particles ($\chi_p < 0$) in a diamagnetic medium ($\chi_m < 0$), the term $\triangle\chi$ can be positive or negative, i.e., the particle is either repelled from, or attracted to the magnetic field. The magnetic susceptibility of a particle and the surrounding material are generally very close to each other, thus $\triangle\chi$ is often rather small, and the force on the particle almost negligible.

The buffer medium can be made paramagnetic. When a diamagnetic particle ($\chi_p < 0$) is placed into a paramagnetic medium ($\chi_m > 0$), $\triangle\chi$ is always negative, thus the diamagnetic particle is repelled from the magnetic field, and pushed towards field gradient minima. The larger χ_m the stronger the repelling force.

Additionally, a paramagnetic particle ($\chi_p > 0$) can be made to act like a diamagnetic material by placing it into a strongly paramagnetic medium, ($\chi_m > \chi_p > 0$). In this case, $\triangle\chi$ is negative, and the paramagnetic particle is repelled from the magnetic field. In most cases, however, paramagnetic particles are placed into a diamagnetic medium, ($\chi_m < 0 < \chi_p$), resultant in a positive $\triangle\chi$, and consequently attraction of the paramagnetic particles towards field gradient maxima. Attraction of particles, towards field gradient maximum, is perhaps the most interesting case concerning the invention since $|\nabla\mathbf{B}| \gg |\mathbf{B}|$.

6.3 Hydrodynamic interactions

The magnetic force is the sole driving agent of the separation. Nevertheless, a better understanding of how the magnetic force interacts with the surroundings, results in better theoretical understanding of the whole separation process. Magnetism is not the only phenomena contributing to the motion of particles in magnetophoresis in microfluidic environments. Hydrodynamic interactions is the phenomenon that, particles moving *in* a fluid is also moved *by* the surrounding fluid, thus particles subject to a magnetic force is moved relative to the unperturbed fluid flow. This relative motion sets up a viscous drag from the fluid, thus a momentum transfer. This transfer of momentum gives rise to an additional flow, a change in fluid velocity, that in principle affects the global fluid flow pattern. In any case, dampening of velocity differences, caused by viscous action, i.e., the mechanism of dissipation of kinetic energy gives rise to drags on bodies moving relative to the surrounding fluid, and forces the particles to accelerate, in order to establish a force balance between drag, and the external magnetic force.

6.3.1 Motion in viscous fluid

The drag force on a spherical particle of radius a in an incompressible fluid is given by Stokes' law

$$\mathbf{F}_\eta = -6\pi\eta a\mathbf{v}, \tag{6.3}$$

where η is the bulk fluid viscosity, and $\mathbf{v}$ is the velocity of the spheres, relative to the fluid [46].

This definition is only valid under low Reynolds numbers, where the viscous effects dominate, and the motion of $\mathbf{v}$ is laminar[2], and slow. The factor $(6\pi\eta a)^{-1}$ is called the mobility b, and is interpreted as the speed a spherical particle attains, when it is subject to a unit force.

A spherical particle suddenly subject to a changed external force will accelerate until the viscous force balances the external force on the particle. By Newton's second law and Stokes' law for the viscous drag this balance is written as

$$m\frac{\partial \mathbf{v}}{\partial t} = \mathbf{F}_{ext} + \mathbf{F}_{\eta} = \mathbf{F}_{ext} - 6\pi\eta\mathbf{v}. \tag{6.4}$$

The terminal magnetophoretic velocity is thus given as $\mathbf{F}_{ext}/6\pi\eta a$, and is attained exponentially with a time constant of

$$\tau = \frac{m}{6\pi\eta a} = \frac{2\rho a^2}{9\eta}, \tag{6.5}$$

where ρ is the density of the fluid [47]. The acceleration happens very quickly, e.g., in water at room temperature where the viscosity is 10^{-3} kg/ms, and the density is 10^3 kg/m^3, a particle with a radius of 10 μm obtains maximum velocity in less than 0.25 μs.

As the changes in the external force happen on a much shorter time-scale than changes in the force experienced by the particles, the viscous drag balances the external force at all times. Furthermore, since the acceleration happens very quickly, and the mass of the particle is very small, $m\frac{\partial \mathbf{v}}{\partial t}$ is negligible. According to Watarai *et al.* [21] the terminal velocity is then represented as

$$\mathbf{v} = \frac{2}{9}\frac{\triangle\chi}{\mu_0\eta}a^2\mathbf{B}\nabla\mathbf{B}. \tag{6.6}$$

The magnetophoretic velocity is, thus dependent on the size and magnetic characteristics of the particle, i.e., the velocity is proportional to $\triangle\chi$, and a^2. Different sized particles with different susceptibilities will therefore be deflected from the direction of the laminar flow, to different degrees.

6.3.2 Motion in fluid flow and external magnetic field

The balancing of forces in a microfluidic channel, where a particle is subject to a fluid flow and an external magnetic field, thus yields

$$0 = \mathbf{F}_{mag} + \mathbf{F}_{\eta} = \frac{V\triangle\chi}{\mu_0}\mathbf{B}\nabla\mathbf{B} - 6\pi\eta_{eff}a(\mathbf{v} - \mathbf{u}(\mathbf{r})), \tag{6.7}$$

where $\mathbf{u}(\mathbf{r})$ is the velocity of the fluid flow, and $\mathbf{v}$ is the velocity of the particles, relative to the fluid [21, 47]. Note that, η_{eff} is the effective viscosity of the fluid in the channel, and is generally larger than the bulk viscosity (η). The reason is that,

---

[2] A laminar flow is a regular, smooth fluid motion known as a Poiseuille flow. It occurs when $Re = \rho d\mathbf{v}/\eta < Re_c$, where Re is the Reynolds number and Re$_c$ is the critical Reynolds number. A flow that is not laminar is turbulent.

microfluidics is a complex area where fluids often have spatial rheological variations, characterized by length scales comparable to the structure of the system. Nearby walls, as well as correlations between individual particles, severely complicates the local viscosity in tiny, confined, or complex fluids, consequently measuring the rheological properties is quite challenging. Nevertheless, the more complex the system, the more essential it is to understand these properties, in order to describe the "true" motion of the particles. A study, made by Svåsand *et al.* [48], presents a method for measuring the effective viscosity of very small volumes of ferrofluids. The hydrodynamic drag force in Equation 6.3, acting on a particle in an incompressible fluid, is corrected to take into account the effect of nearby walls, as well as correlations between particles, and by doing so obtaining a result, consistent with viscosity values found in standard bulk measurement techniques.

6.4 Summary and discussion

The concept of magnetophoresis in microfluidic flows is well known, nevertheless, by combining extremely intensive magnetic forces produced in very small volumes, where $\mathbf{B}\nabla\mathbf{B}$ reaches values of 10^{10}-10^{11} $\mathrm{mT^2/m}$, the new design opens up new and interesting aspects, especially in combination with on-chip free-flow magnetophoresis. The need to couple weak paramagnetic and diamagnetic biological particles, or cells to highly magnetic beads, in order to separate them out from their surrounding medium, may be obsolete. Imagine the possibilities, being able to separate paramagnetic and diamagnetic gases according to their susceptibilities, using only permanent magnets.

Miniaturizing permanent magnet structures, and integrating them onto lab-on-chip devices allows for functions like transportation, positioning, mixing, separation, and sorting of magnetic, as well as non-magnetic particles to be made automatic and compatible with physics on microfluidic scales. However, manufacturing a microfluidic channel container is a process which requires extremely accurate techniques and tools. Establishing a procedure for pumping, counting, and collecting particles adds even more complexity to the problem. It is, however, imperative that the separation capacity of the device is studied in its native environment. In any magnetic separator, the particles that interact with the magnetic field also interact with the carrier medium, and with each other. This is a complex many-body problem, very hard to treat exactly. As a result, theoretical simulations are in many cases imperative, as they allow one to easily study different geometries, enhance control, as well as optimizing separator design. Nevertheless, testing it out in real life provides with much more useful information, than what simulations of the system do.

Regrettably, there is not enough time to include work on this subject in this thesis. Further study of the device is needed, and the work should focus on making a separation chamber with walls thinner than 0.04 mm, preferably as thin as possible, in order to utilize, and verify the full potential of the extreme magnetic forces this device is capable of producing.

Chapter 7

Summary and outlook

The objectives of this thesis cover the generation of a simulation environment completely describing the behavior of the invention in [4], as well as investigating the simulation results obtained by Il'yashenko *et al.* in [5]. Establishing an optimal configuration of mask thickness, gap size, soft magnetic, and permanent magnet material is essential, in order to maximize the dominating $\mathbf{B}\nabla\mathbf{B}$ term in the magnetic force on objects. The theoretical approximations to a half open Kittel domain, derived by Samofalov *et al.* in [6], forming the basis of the invention, have also been numerically studied. Lastly, experimental measurements have been performed on a model of the invention, aiming to verify both simulations, and theory.

Numerical studies show that, the theoretical approximation to the tangential field in half open Kittel domains closely matches simulation, when corrected for a 15% overestimation of the field value in the immediate vicinity of point O. The theoretical approximation to the normal field matches simulation without the correction. Both theory and simulation estimate $\mathbf{B}\nabla\mathbf{B}$ values on the order of 10^9 mT^2/m, thus within the expected range of 10^8-10^{10} mT^2/m, derived in [6].

Simulations show that, when the mask thickness and gap size are 0.05 mm, the strength of the tangential component of the magnetic stray field, in a distance of 0.01 mm to the surface of the masks, increases with a factor of 20% compared to that in an analog structure. The width of the peak of the tangential component is also narrower than in the analog case, regardless of mask thickness, *if* the gap size is less than 0.10 mm. An extremely strong magnetic field gradient, several times stronger than in the analog structure is thus produced, owing to the fact that most of the dependency in $\mathbf{B}\nabla\mathbf{B}$ lies in the *shape* of the magnetic field. The z-gradient of $\mathbf{B}$, however, opposes the x-gradient, but B_x is approximately five times stronger than B_z, as a result $B_x(\nabla B)_x$ is the dominating contributor to the magnetic force. In the same distance, $\mathbf{B}\nabla\mathbf{B}$ reaches a maximum value of 10^{10}-10^{11} mT^2/m, comparable to what is obtained in [5].

The singularities in the demagnetization field around the sharp corners of the masks, contributing to the increase of the tangential field, merge together to form one when the gap size decreases below approximately 0.10 mm. The consequence is that, the tangential profile is "pushed" upwards, and narrowing in width, thus increasing the gradient. Above this gap size, however, the strongest gradient is no longer positioned in the center of the gap, but governed by the location of the mask corners, with values of **B∇B** in the range of 10^{10}-10^{11} mT^2/m, and approaching analog values of 10^9 mT^2/m in the center of the gap. As a consequence, the device has the ability to control the position of gradient maxima and minima by adjusting the gap size. However, the singularities at the corners of the masks are produced in demagnetization fields near ideal square edges, and precisely controlling the shape of these corners in real devices is difficult. Additionally, when the gap size is smaller than 0.10 mm, the gradient maxima and minima is a result of two singularities merging in the tangential field. For these particular reasons the simulations strongly suggest using gap sizes below 0.10 mm, in order to focus the separation in the center of the gap for and additive effect.

Further analysis show that, the singularities in the demagnetization fields near the corners of the masks, responsible for most of the increase and distortion of the tangential field, disappears in distances larger than a critical distance of 0.04 mm. Depending on thickness, the masks now decrease the magnetic induction of the field compared to that in an analog structure, thus having the opposite effect than what is desired.

In short, the device does the following: (I) Increases the tangential magnetic field in the center of the air gap. (II) By decreasing the gap size the width of the peak in the magnetic field decreases, and as a consequence the gradient increases. (III) As a result, **B∇B** increases.

Final analysis show that, the strength of the magnetic stray field is proportional to the coercivity of the permanent magnets, while **B∇B** is proportional to the square of the coercivity. Furthermore, **B∇B** is proportional to the magnetization saturation of the masks, *if* the distance to the masks is less than the critical distance.

The device has interesting and useful properties with a number of possible applications in electronics, metallurgy, chemistry, and biology. Magnetophoresis in hydrodynamic fluid flows is one of many areas where the device shows promising results. The study show that, in order to utilize the increased potential in the magnetic force obtained by adding masks on top of the magnets, the separation process has to be carried out closer than 0.04 mm to the surface of the masks. As such, it is reasonable to suggest that separation of large bulk quantities, in separation distances larger than this critical distance, is performed better in a device without masks.

However, the situation is quite different in samples that come in small quantities, such as biological material, or fluids that are confined to small regions. Functions like transportation, positioning, mixing, separation, and sorting of magnetic as well as non-magnetic particles can be made automatic, and compatible with the physics of fluid flows on microfluidic scales. This is done by integrating the device onto chips by means of MEMS techniques. Miniaturization of lab-on-chip devices offers a highly efficient separation, because the magnetic force on a particle is higher, the closer it is to the surface of the source. Thus, separation of weak paramagnetic particles from diamagnetic particles in biological environments, is perhaps the most interesting case.

Experimental measurements indicate that the values obtained for **B∇B** in simulations are close to realistic, when the distance to the masks is larger than the critical distance. The magnetic field is measured with Hall effect probes, and because these have finite thicknesses of more than 0.04 mm, the field can not be measured close enough to observe the singularities above the mask corners. The full extent of the simulations can thus not be verified. A possible solution to this problem, in order to observe the interesting tangential magnetic field distribution very close to the surface, is to measure the magnetic stray field using a giant magnetoresistive effect sensor with a magnetic film of thickness less than 0.04 mm.

Further study of the device is needed, and the work should focus on a way to measure the magnetic field closer to the surface of the masks. The magnetophoretic properties should also be tested, by making a separation chamber with walls thinner than 0.04 mm, preferably as thin as possible, in order to utilize and verify the full potential of the extreme magnetic forces this device is able to produce. A better approximation to the magnetic stray field can also be obtained, through a numerical study of how the field changes when the shape of the corners of the masks changes, thus determining the importance of the singularities in the demagnetization field.

As a concluding remark based on the assumption that, perfectly square corners of the masks, as well as ideal adjoining surfaces between materials is difficult to obtain in a real model, $\mathbf{B}\nabla\mathbf{B}$ values exceeding 10^{11} mT^2/m in a distance of 0.01 mm above the surface of the masks is unrealistic. A more reasonable suggestion is 10^{10} mT^2/m, still several times larger than that in an analog structure. In other words, if the device is used for separation in tiny, confined fluids, and the separation distance is less than the critical distance, the newly designed device is far superior to an analog structure.

Further work should also be motivated by the fact that, finding methods that only slightly decreases the width of the stray field distribution will drastically increase its gradient. Additionally, producing new and better magnet and mask material compounds, as well as perfecting techniques ensuring ideal magnet-mask and magnet-magnet junctions will further increase the potency of the device.

References

[1] T. Shiga, M. Okazaki, A. Seiyama, and N. Maeda, *Biochem. and Bioenerg.* **30**, p. 181 (1993).

[2] A. Yamagishi, T. Takeuchi, and M. Date, *Physika B* **177**, p. 523 (1992).

[3] V. N. Samofalov, E. I. Il'yashenko, A. Ramstad, L. Z. Lub'yanuy, and T. H. Johansen, *J. Opt. Adv. Mat.* **6**(3), p. 911−916 (2004).

[4] V. A. Glebov, A. V. Glebov, E. I. Il'yashenko, A. T. Skjeltorp, and T. H. Johansen, *The international application*, PCT/RU 000514 (2004).

[5] E. I. Il'yashenko, V. A. Glebov, A. V. Glebov, A. T. Skjeltorp, and T. H. Johansen, *Phys. Stat. Sol. (a)*, **203**(7), p. 1556−1560 (2006).

[6] V.N. Samofalov, A.G. Ravlika, D.P. Belozorovb, and B.A. Avramenkoa, *J. Opt. Adv. Mat.* **281**, p. 326−335 (2004).

[7] V. I. Arnold, *Ordinary Differential Equations*, MIT Press, Cambridge, U.S.A. (1973).

[8] C. F. Gauss, *Allgemeine Theorie des Erdmagnetismus* (1839).

[9] G. Arfken, *Mathematical Methods for Physicists*, 3rd ed., Orlando, FL, Academic Press, p. 78−84 (1985) .

[10] I. S. Gradshteyn, and I. M. Ryzhik, *Tables of Integrals, Series, and Products*, 6th ed., San Diego, CA, Academic Press, p. 1084 (2000).

[11] B. D. Cullity, *Introduction to Magnetic Materials*, Reading, MA, Addison−Wesley (1972).

[12] C. Kittel, *Introduction to Solid State Physics*, 8th ed., New York, NY, John Wiley and Sons (2005).

[13] Anonymous, *Annual Book of ASTM Standards*, Philadelphia, PA, ASTM, (1995).

[14] D.K. Cheng, *Fundamentals of Engineering Electromagnetics*, Addison−Wesley (1993).

[15] F. Bloch, *IEEE Trans. Magn.* **34**(1), p. 2465 (1988).

[16] F. Bloch, *Eur. Phys. J. Appl. Phys.* **5**, p. 85 (1999).

[17] K. Halbach, *Nucl. Instrum. Methods* **169**, p. 1 (1980).

[18] K. Halbach, *J. Appl. Phys.* **57**, p. 3605 (1985).

[19] H. A. Leupold, and G. F. McLane, *J. Appl. Phys.* **76**, p. 6253 (1994).

[20] E. A. Nesbitt, J. H. Wernick, *Rare Earth Permanent Magnets*, Bell Laoratories Murray Hill, New Jersey, Academic Press, New York and London (1973) IN [6].

[21] H. Watarai, M. Suwa, and Y. Iiguni, *Anal. Bioa. Chem* **378**, p. 1693−1699 (2004).

[22] J. D. Edwards, *An Introduction to MagNet; for Static 2D Modeling*, Infolytica Corporation, Canada (2007).

[23] P.P. Silvester, and R.L. Ferrari, *Finite Elements for Electrical Engineers*, 2nd ed., Cambridge University Press (1990).

[24] P. Deuflhard, *Newton Methods for Nonlinear Problems. Affine Invariance and Adaptive Algorithms* **35**, Springer, Berlin (2004).

[25] W. Rave, K. Ramstöck, and A. Hubert, *J. Magn. Magn. Mater.* **183**, p. 328 (1998).

[26] A. Thiaville, D. Tomàs, and J. Miltat, *Phys. Stat. Sol. (a)* **170**, p. 125 (1998).

[27] R. P. Feynman, R. B. Leighton, and M. Sands, *The Feynman Lectures on Physics*, The Definitive and Extended Edition, 2nd ed., Volume 3: Quantum Mechanics, p. 14−3, (2005).

[28] C. Cordier, L. Mechin, C. Gunther, M. L. C. Sing, D. Bloyet, and V. Mosser, *IEEE Sens. J.* **5**(5), (2005).

[29] A. Thiaville, L. Belliard, D. Majer, E. Zeldov, and J. Miltat, *J. Appl. Phys.* **82**, p. 3182−3191 (1997).

[30] A. Fert, *Phys. Rev. Let.* **61**(21), p. 2472−2475 (1988).

[31] T. Vilkner, D. Janasek, and A. Manz, *Anal. Chem.* **76**, p. 3373 (2004) IN [49].

[32] D. R. Reyes, D. Iossifidis, P. A. Auroux, and A. Manz, *Anal. Chem.* **74**, p. 2623 (2002) IN [45].

[33] P. A. Auroux, D. Iossifidis, D. R. Reyes, and A. Manz, *Anal. Chem.* **74**, p. 2637 (2002) IN [45].

[34] M. D. Simon, and A. K. Geim, *J. Appl. Phys.* **87**, p. 6200 (2000) IN [45].

[35] M. Zborowski, P. S. Malchesky, T. F. Jan, and G. S. Hall, *J. Gen.Microbiol.* **138**, p. 63 (1992) IN [49].

[36] M. Zborowski, L. R. Moore, P. S. Williams, and J. J. Chalmers, *Sep. Sci. Technol.* **37**, p. 3611 (2002) IN [49].

[37] I. Safarik, and M. Safarikova, *J. Chromatogr., B: Biomed. Appl.* **722**, p. 33 (1999) IN [49].

[38] J. C. Giddings, and S. L. Brantley, *Separ. Sci. Technol.* **19**, p. 631−651 (1984) IN [21].

[39] A. H. Latham, R. S. Freitas, P. Schiffer, and M. E. Williams, *Anal. Chem.* **77**, p. 5055 (2005) IN [49].

[40] P. C. Gascoyne, C. Das, J. Vykoukal, R. Weinstein, A. Gandini, D. Parks, and R. Sawh, *Abstr. Pap. − Am. Chem. Soc.* **225**, U138 (2003) IN [49].

[41] C. B. Fuh, and S. Y. Chen, *J. Chromatogr. A.* **813**, 313324 (1998) IN [49].

[42] C. B. Fuh, and S. Y. Chen, *J. Chromatogr. A.* **857**, 193−204 (1999) IN [49].

[43] C. B. Fuh, J. Z. Lai, and C. M. Chang, *J. Chromatogr. A.* **923**, p. 263−270 (2001) IN [21].

[44] T. M. Vickrey, and J. A. Garcia−Ramirez, *Separ. Sci. Technol.* **15**, p. 1297−1304 (1980) IN [21].

[45] N. Pamme, and A. Manz, *Anal. Chem.* **76**(24), Imperial College London, Department of Chemistry, London, p. 7250−7256 (2004).

[46] L. D. Landau, and E. M. Lifshitz, *Fluid Mechanics*, volume 6 of Landau and Lifshitz, Course of Theoretical Physics, 2nd ed., Butterworth−Heinemann, Oxford (1987) IN [47].

[47] C. I. Mikkelsen, *Magnetic separation and hydrodynamic interactions in microfluidic systems*, Ph.D. Thesis, Department of Micro and Nanotechnology, Technical University of Denmark, p. 1−54 (2005).

[48] E. Svaasand, A. T. Skjeltorp, J. Akselvoll, and G. Helgesen, *J. Appl. Phys.* **101** (2007).

[49] N. Pamme, *Magnetism and microfluidics* **6**, Lab chip, p. 24−38 (2006).

Appendix A

Implementation in MagNet

A.1 Vanadium permendur magnetization curve data

```
H [A/m] B [T]
0       0
71.4    0.6
119     1
175     1.6
268     1.8
493     2
804     2.1
1910    2.2
4775    2.26
15120   2.3
42971   2.34
79577   2.39
```

A.2 Low carbon steel magnetization curve data

```
H [A/m] B [T]
0       0
109.3   0.259
120.7   0.2849
132.2   0.3108
143.8   0.3367
157.1   0.3627
171     0.3886
185     0.4145
199.5   0.4404
214.5   0.4663
230.2   0.4922
246.5   0.5181
263.3   0.544
280.7   0.5699
298.9   0.5958
317.9   0.6217
337.5   0.6476
357.9   0.6735
379.2   0.6994
401.3   0.7253
424.3   0.7512
448.2   0.7771
473.1   0.803
498.9   0.8289
525.8   0.8548
553.7   0.8807
582.6   0.9066
612.7   0.9325
643.9   0.9584
676.2   0.9843
709.8   1.01
744.4   1.036
780.3   1.062
817.1   1.088
853.8   1.114
895.8   1.14
935.5   1.166
985.1   1.192
1038    1.217
1096    1.243
1157    1.269
1223    1.295
1301    1.321
1378    1.347
1480    1.373
1590    1.399
1708    1.425
1848    1.451
2007    1.477
2172    1.502
2359    1.528
2592    1.554
2784    1.58
3116    1.606
3562    1.632
4174    1.658
4807    1.684
5455    1.71
6128    1.736
6746    1.761
7559    1.787
9123    1.813
11010   1.839
12940   1.865
14940   1.891
16960   1.917
18640   1.943
21620   1.969
26730   1.995
32240   2.02
42090   2.046
57310   2.072
90470   2.125
124200  2.175
159100  2.22
```

A.3 Configuration of materials

```
Call newDocument()
Call getUserMaterialDatabase().newMaterial("Vanadium permendur")
Call getUserMaterialDatabase().setMaterialColor("Vanadium permendur", 128, 0, 128, 255)
Call getUserMaterialDatabase().setMaterialDescription("Vanadium permendur", "Soft magnetic material with high saturation")
Call getUserMaterialDatabase().setMaterialCategories("Vanadium permendur", Array())
REDIM A(0, 1)
A(0, 0)= 20
REDIM A0(11, 1)
A0(0, 0)= 0
A0(0, 1)= 0
A0(1, 0)= 71.4
A0(1, 1)= 0.6
A0(2, 0)= 119
A0(2, 1)= 1
A0(3, 0)= 175
A0(3, 1)= 1.6
A0(4, 0)= 268
A0(4, 1)= 1.8
A0(5, 0)= 493
A0(5, 1)= 2
A0(6, 0)= 804
A0(6, 1)= 2.1
A0(7, 0)= 1910
A0(7, 1)= 2.2
A0(8, 0)= 4775
A0(8, 1)= 2.26
A0(9, 0)= 15120
A0(9, 1)= 2.3
A0(10, 0)= 42971
A0(10, 1)= 2.34
A0(11, 0)= 79577
A0(11, 1)= 2.39
A(0, 1)= A0
Call getUserMaterialDatabase().setMagneticPermeability("Vanadium permendur", A, infoNonlinearIsotropicReal)
REDIM ArrayOfValues(0, 1)
ArrayOfValues(0, 0)= 20
ArrayOfValues(0, 1)= 0
Call getUserMaterialDatabase().setElectricConductivity("Vanadium permendur", ArrayOfValues, infoLinearIsotropicReal)
REDIM ArrayOfValues(0, 1)
ArrayOfValues(0, 0)= 20
ArrayOfValues(0, 1)= 1
Call getUserMaterialDatabase().setElectricPermittivity("Vanadium permendur", ArrayOfValues, infoLinearIsotropicReal)
If (hasDocument()) Then
   Call getDocument().getModelMaterialDatabase().updateMaterial("Vanadium permendur", False)
End If

Call getUserMaterialDatabase().newMaterial("NdFeB: Neodymium Iron Boron")
Call getUserMaterialDatabase().setMaterialColor("NdFeB: Neodymium Iron Boron", 127, 255, 212, 255)
Call getUserMaterialDatabase().setMaterialCategories("NdFeB: Neodymium Iron Boron", Array("Permanent magnet material"))
REDIM ArrayOfValues(0, 2)
ArrayOfValues(0, 0)= 20
ArrayOfValues(0, 1)= 1.1
ArrayOfValues(0, 2)= -955000
Call getUserMaterialDatabase().setMagneticPermeability("NdFeB: Neodymium Iron Boron", ArrayOfValues, infoLinearIsotropicReal)
REDIM ArrayOfValues(0, 1)
ArrayOfValues(0, 0)= 20
ArrayOfValues(0, 1)= 0
```

```
Call getUserMaterialDatabase().setMagneticDemagnetization("NdFeB: Neodymium Iron Boron", ArrayOfValues)
REDIM ArrayOfValues(0, 1)
ArrayOfValues(0, 0)= 20
ArrayOfValues(0, 1)= 1.5e-006
Call getUserMaterialDatabase().setElectricResistivity("NdFeB: Neodymium Iron Boron", ArrayOfValues, infoLinearIsotropicReal)
REDIM ArrayOfValues(0, 1)
ArrayOfValues(0, 0)= 20
ArrayOfValues(0, 1)= 1
Call getUserMaterialDatabase().setElectricPermittivity("NdFeB: Neodymium Iron Boron", ArrayOfValues, infoLinearIsotropicReal)
If (hasDocument()) Then
   Call getDocument().getModelMaterialDatabase().updateMaterial("NdFeB: Neodymium Iron Boron", False)
End If
```

A.4 Configuration of system

```
Call newDocument()
Call getDocument().beginUndoGroup("Set Default Units", true)
Call getDocument().setDefaultLengthUnit("Millimeters")
Call getDocument().endUndoGroup()
Call getDocument().getView().setScaledToFit(True)

Call getDocument().getView().newLine(-100, -100, 100, -100)
Call getDocument().getView().newLine(100, -100, 100, 100)
Call getDocument().getView().newLine(100, 100, -100, 100)
Call getDocument().getView().newLine(-100, 100, -100, -100)
Call getDocument().getView().setScaledToFit(True)
Call getDocument().getView().newLine(-50, -25, 50, -25)
Call getDocument().getView().newLine(50, -25, 50, 0)
Call getDocument().getView().newLine(50, 0, -50, 0)
Call getDocument().getView().newLine(-50, 0, -50, -25)
Call getDocument().getView().newLine(-50, 0, 0, 0)
Call getDocument().getView().newLine(0, 0, 0, 50)
Call getDocument().getView().newLine(0, 50, -50, 50)
Call getDocument().getView().newLine(-50, 50, -50, 0)
Call getDocument().getView().newLine(0, 0, 50, 0)
Call getDocument().getView().newLine(50, 0, 50, 50)
Call getDocument().getView().newLine(50, 50, 0, 50)
Call getDocument().getView().newLine(0, 50, 0, 0)
Call getDocument().getView().newLine(-50, 50, -0.025, 50)
Call getDocument().getView().newLine(-0.025, 50, -0.025, 50.05)
Call getDocument().getView().newLine(-0.025, 50.05, -50, 50.05)
Call getDocument().getView().newLine(-50, 50.05, -50, 50)
Call getDocument().getView().newLine(0.025, 50, 50, 50)
Call getDocument().getView().newLine(50, 50, 50, 50.05)
Call getDocument().getView().newLine(50, 50.05, 0.025, 50.05)
Call getDocument().getView().newLine(0.025, 50.05, 0.025, 50)

Call getDocument().getView().selectAt(-66.9140625, 54.110668182373, infoSetSelection, Array(infoSliceSurface))
REDIM ArrayOfValues(0)
ArrayOfValues(0)= "Air space"
Call getDocument().getView().makeComponentInALine(25, ArrayOfValues, "Name=AIR", infoMakeComponentUnionSurfaces Or infoMakeComponentRemoveVertices)
Call getDocument().getView().selectAt(-22.5394744873047, 27.2298851013184, infoSetSelection, Array(infoSliceSurface))
REDIM ArrayOfValues(0)
ArrayOfValues(0)= "Magnet up"
Call getDocument().getView().makeComponentInALine(25, ArrayOfValues, "Name=NdFeB: Neodymium Iron Boron;Type=Uniform;Direction=[0,1,0]", infoMakeComponentUnionSurfaces Or infoMakeComponentRemoveVertices)
Call getDocument().getView().selectAt(21.8351154327393, 23.7388744354248, infoSetSelection, Array(infoSliceSurface))
```

```
REDIM ArrayOfValues(0)
ArrayOfValues(0)= "Magnet down"
Call getDocument().getView().makeComponentInALine(25, ArrayOfValues, "Name=NdFeB:
    Neodymium Iron Boron;Type=Uniform;Direction=[0,-1,0]",
    infoMakeComponentUnionSurfaces Or infoMakeComponentRemoveVertices)
Call getDocument().getView().selectAt(-19.0176811218262, -17.1059532165527,
    infoSetSelection, Array(infoSliceSurface))
REDIM ArrayOfValues(0)
ArrayOfValues(0)= "Yoke"
Call getDocument().getView().makeComponentInALine(25, ArrayOfValues, "Name=Vanadium
    permendur", infoMakeComponentUnionSurfaces Or infoMakeComponentRemoveVertices)
Call getDocument().getView().selectAt(-1.00685060024261, 50.0439796447754,
    infoSetSelection, Array(infoSliceSurface))
REDIM ArrayOfValues(0)
ArrayOfValues(0)= "Mask up"
Call getDocument().getView().makeComponentInALine(25, ArrayOfValues, "Name=Vanadium
    permendur", infoMakeComponentUnionSurfaces Or infoMakeComponentRemoveVertices)
Call getDocument().getView().selectAt(0.0939577668905258, 50.0177993774414,
    infoSetSelection, Array(infoSliceSurface))
REDIM ArrayOfValues(0)
ArrayOfValues(0)= "Mask down"
Call getDocument().getView().makeComponentInALine(25, ArrayOfValues, "Name=Vanadium
    permendur", infoMakeComponentUnionSurfaces Or infoMakeComponentRemoveVertices)

Call getDocument().getView().selectObject("Air space", infoSetSelection)
Call getDocument().getView().selectObject("Air space,Face#3", infoSetSelection)
Call getDocument().getView().selectObject("Air space,Face#4", infoAddToSelection)
Call getDocument().getView().selectObject("Air space,Face#3", infoSetSelection)
Call getDocument().getView().selectObject("Air space,Face#4", infoAddToSelection)
Call getDocument().getView().selectObject("Air space,Face#5", infoAddToSelection)
Call getDocument().getView().selectObject("Air space,Face#3", infoSetSelection)
Call getDocument().getView().selectObject("Air space,Face#4", infoAddToSelection)
Call getDocument().getView().selectObject("Air space,Face#5", infoAddToSelection)
Call getDocument().getView().selectObject("Air space,Face#6", infoAddToSelection)
Call getDocument().beginUndoGroup("Assign Boundary Condition")
REDIM ArrayOfValues(3)
ArrayOfValues(0)= "Air space,Face#3"
ArrayOfValues(1)= "Air space,Face#4"
ArrayOfValues(2)= "Air space,Face#5"
ArrayOfValues(3)= "Air space,Face#6"
Call getDocument().createBoundaryCondition(ArrayOfValues, "BoundaryCondition#1")
Call getDocument().setMagneticFluxTangential("BoundaryCondition#1")
Call getDocument().endUndoGroup()
Call getDocument().getView().selectObject("Air space", infoSetSelection)
Call getDocument().getView().selectObject("Air space,Face#3", infoAddToSelection)
Call getDocument().getView().selectObject("Air space,Face#4", infoAddToSelection)
Call getDocument().getView().selectObject("Air space,Face#5", infoAddToSelection)
Call getDocument().getView().selectObject("Air space,Face#6", infoAddToSelection)
Call getDocument().getView().unselectAll()
Call getDocument().beginUndoGroup("Set Properties", true)
Call getDocument().setSolverMaterialType(infoNonlinearMaterial)
Call getDocument().setCGTolerance(1e-022)
Call getDocument().setNewtonTolerance(1e-015)
Call getDocument().setMaxNumberOfNewtonIterations(100000)
Call getDocument().setImproveMeshQuality(True)
Call getDocument().useHAdaption(True)
Call getDocument().setAdaptionTolerance(1e-012)
Call getDocument().setMaximumNumberOfAdaptionSteps(100000)
Call getDocument().setHAdaptionRefinement(1)
Call getDocument().endUndoGroup()
```

Appendix B

Implementation in MatLab

B.1 Theory.m

```
% Written by Inge Buanes Roth, 04/03/09


%------------------------------------------------
%           THEORETICAL CALCULATIONS
%------------------------------------------------


a = 50;   % length of magnets 50 mm
b = a/2;  % depth of magnets 25 mm

x = 0;    % calculate Bx in x = 0
y = 0;    % calculate Bx or Bz in y = 0
z = 0.01; % calculate Bx or Bz 0.01 mm above surface

mu0 = 4*pi*1.0e-7; % permeability of free space
mur = 1.10;        % relative permeability of permanent magnets

M = 2.00/mu0/mur; % NdFeB "perfect", converts Tesla to Ampere per meter
M = 1.45/mu0/mur; % NdFeB 50M
M = 1.32/mu0/mur; % NdFeB 42H

x = -10:0.01:10;  % calculate Bx or Bz around x = 0 in step of 0.01 mm
z = 0.01:0.01:5;  % calculate Bx 0.01 mm to 5.00 mm above surface

step = 0.01;

% ANALYTIC EXPRESSIONS TO BX AND BZ
%-----------------------------------

Hxtheory = M*[log(a.*a-2.*a.*x+x.*x+z.*z) - 2*log(x.*x+z.*z)
         + log(a.*a+2.*a.*x+x.*x+z.*z)];

Bxtheory = Hxtheory*mu0/4/pi; % converts from CGS to SI

Hztheory = 2.*M.*(atan((a+x)/z)-atan((a-x)/z)-2.*atan(x/z));
Bztheory = Hztheory*mu0/4/pi;

plot(x+10,Bxtheory); % +10 converts negative x values to postive
plot(x+10,Bztheory); % +10 converts negative x values to postive
plot(z,Bxtheory);

% GRADIENT CALCULATIONS
%-----------------------

gradxtheory = gradient(Bxtheory);
gradztheory = gradient(Bztheory);
```

```

gradxtheory = gradxtheory .* Bxtheory * 1000 * 1000 * 1000 / step;
gradztheory = gradztheory .* Bztheory * 1000 * 1000 * 1000 / step;

% 1000 * 1000 transforms T^2 -> mT^2
% 1000 * mT^2/mm -> mT^2/m

plot(x+10,gradxtheory+gradztheory);
```

B.2 Simulation.m

```
% Written by Inge Buanes Roth, 04/03/09


%--------------------------------------------------
%            SIMULATION CALCULATIONS
%--------------------------------------------------


Bxsim = importdata('Bx_simulation_175mm.txt');
Bzsim = importdata('Bz_simulation_175mm.txt');

plot(Bxsim(:,1),Bxsim(:,2));
plot(Bzsim(:,1),Bzsim(:,2));

% GRADIENT CALCULATIONS
%------------------------

simx = Bxsim(:,1);
simz = Bzsim(:,1);

simstepx = simx(2)-simx(1);
simstepz = simz(2)-simz(1);

gradxsim = gradient(Bxsim(:,2));
gradzsim = gradient(Bzsim(:,2));

gradxsim = gradxsim .* Bxsim(:,2) * 1000 * 1000 * 1000 / simstepx;
gradzsim = gradzsim .* Bzsim(:,2) * 1000 * 1000 * 1000 / simstepz;

plot(simx,gradxsim+gradzsim);
```

B.3 Experimental.m

```
% Written by Inge Buanes Roth, 04/03/09


%--------------------------------------------------
%            EXPERIMENTAL CALCULATIONS
%--------------------------------------------------


Bxexp = importdata('Bx_experimental_175mm.txt');
Bzexp = importdata('Bz_experimental_175mm.txt');

plot(Bxexp(:,1)*1.25e-6*1000+1.8,(Bxexp(:,2)*587.16-2284.6)/1000);
plot(Bzexp(:,1)*1.25e-6*1000,(Bzexp(:,2)*608.02-2336.7-50)/1000);

% GRADIENT CALCULATIONS
%------------------------

expx = Bxexp(:,1);
```

```
expz = Bzexp(:,1);

expstepx = (expx(2)-expx(1))*1.25e-6*1000;
expstepz = (expz(2)-expz(1))*1.25e-6*1000;

gradxexp = gradient(Bxexp(:,2)*587.16-2284.6);
gradzexp = gradient(Bzexp(:,2)*608.02-2336.7);

gradxexp = gradxexp .* (Bxexp(:,2)*587.16-2284.6) * 1000 / expstepx;
gradzexp = gradzexp .* (Bzexp(:,2)*608.02-2336.7) * 1000 / expstepz;

plot(expx*1.25e-6*1000,gradxexp);

figure

plot(expz*1.25e-6*1000,gradzexp);

% GRADIENT CALCULATION OF 10TH DEGREE POLYNOMIAL CURVE FIT
%-----------------------------------------------------------

x = 0:0.01:18;

expstepx = 0.01;

% BX COEFFISIENTS
%-----------------

px1 = 1.17e-010;
px2 = -6.5397e-009;
px3 = 1.0312e-007;
px4 = 5.2005e-007;
px5 = -3.0867e-005;
px6 = 0.00031096;
px7 = -0.001137;
px8 = 0.00070835;
px9 = 0.0056089;
px10 = 0.025049;
px11 = 0.22247;

Bxexp = px1*x.^10 + px2*x.^9 + px3*x.^8 + px4*x.^7 + px5*x.^6
      + px6*x.^5 + px7*x.^4 + px8*x.^3 + px9*x.^2 + px10*x.^1 + px11;

gradxexp = gradient(Bxexp);

gradxexp = gradxexp .* Bxexp * 1000 * 1000 * 1000 / expstepx;

% GRADIENT CALCULATION OF 7TH DEGREE POLYNOMIAL CURVE FIT
%-----------------------------------------------------------

xx =0:0.01:20;

expstepz = 0.01;

% BZ COEFFISIENTS
%-----------------

pz1 = -1.5794e-007;
pz2 = 1.1097e-005;
pz3 = -0.00030052;
pz4 = 0.0039605;
pz5 = -0.026657;
pz6 = 0.086457;
pz7 = -0.11133;
pz8 = 0.45563;

Bzexp = pz1*xx.^7 + pz2*xx.^6 + pz3*xx.^5 + pz4*xx.^4 + pz5*xx.^3
      + pz6*xx.^2 + pz7*xx.^1 + pz8;

gradzexp = gradient(Bzexp);

```

```
gradzexp = gradzexp .* Bzexp * 1000 * 1000 * 1000 / expstepz;

% PLOT B GRADIENT B FOR POLYNOMIAL CURVE FITS
%----------------------------------------------------------

plot(x,gradxexp);

hold on

plot(xx,gradzexp);
```

B.4 Calibration.m

```
% Written by Inge Buanes Roth, 04/03/09


%-----------------------------------------------
%           CALIBRATION OF SENSORS
%-----------------------------------------------


% CYL49E SENSOR CALIBRATION CURVE
%--------------------------------------

x = -100:0.1:100;

p1 = 0.018437; % linear fit found from data-
p2 = 2.475;    % description of sensor

calibration_curve_cyl49e = p1*x.^1 + p2;

plot(x,calibration_curve_cyl49e);

% CY-P15A NORMAL SENSOR
%--------------------------------------

x = 3.84:0.01:4.00; % Hall voltage range during calibration

normal_measurement = importdata('Normal_measurement.txt');

plot(normal_measurement(:,1),normal_measurement(:,2));

p3 = 608.02;
p4 = -2336.7;

linear_fit_normal = p3*x + p4;

plot(x,linear_fit_normal);

% CY-P15A TANGENTIAL SENSOR
%---------------------------------------

x = 3.87:0.01:4.04; % Hall voltage range during calibration

tangential_measurement = importdata('Tangential_measurement.txt');

plot(tangential_measurement(:,1),tangential_measurement(:,2));

p5 = 587.16;
p6 = -2284.6;

linear_fit_tangential = p5*x + p6;

plot(x,linear_fit_tangential);
```

Appendix C

Implementation in LabView

C.1 Block diagram

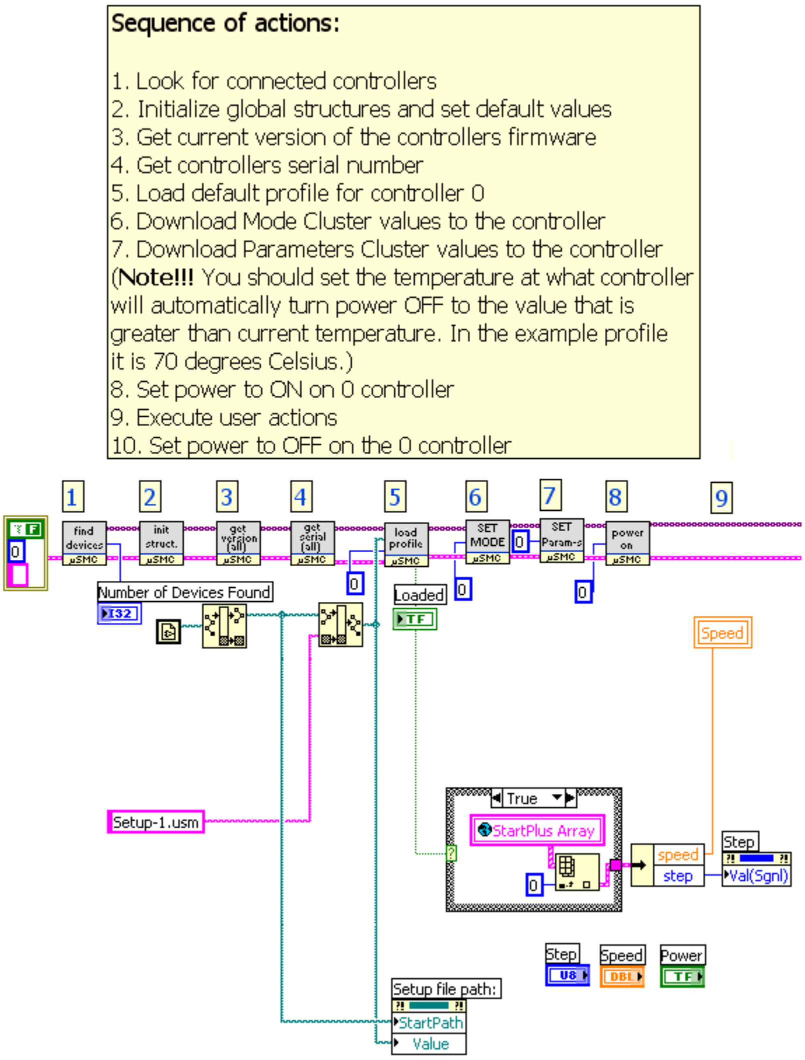

Sequence of actions:

1. Look for connected controllers
2. Initialize global structures and set default values
3. Get current version of the controllers firmware
4. Get controllers serial number
5. Load default profile for controller 0
6. Download Mode Cluster values to the controller
7. Download Parameters Cluster values to the controller (**Note!!!** You should set the temperature at what controller will automatically turn power OFF to the value that is greater than current temperature. In the example profile it is 70 degrees Celsius.)
8. Set power to ON on 0 controller
9. Execute user actions
10. Set power to OFF on the 0 controller

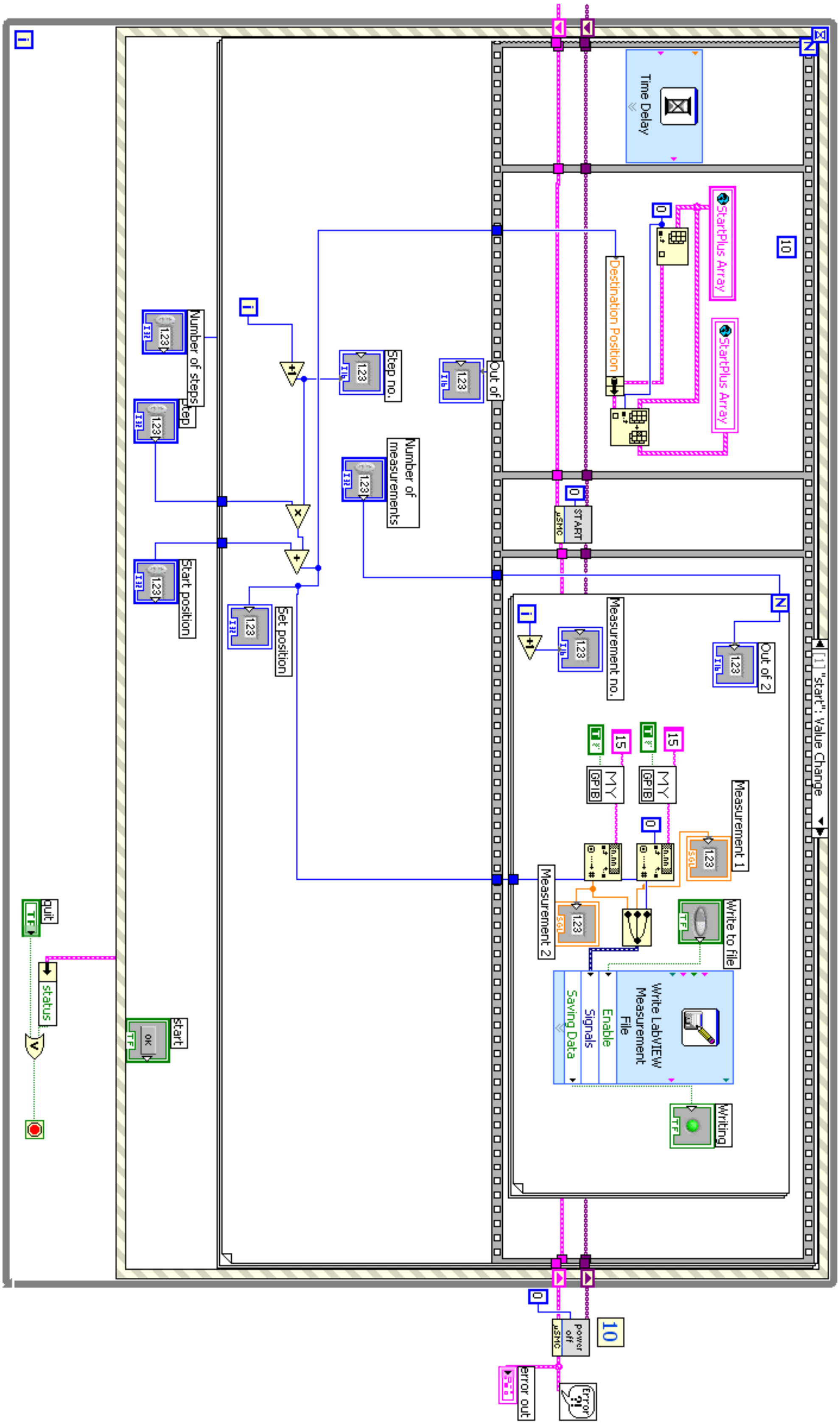
Time Delay
StartPlus Array
StartPlus Array
10
0
Destination Position
Out of
Step no.
Number of steps
Step
Start position
Set position
Number of measurements
0
START
uSMC
Measurement no.
Out of 2
15
15
MY GPIB
MY GPIB
0
Measurement 1
Measurement 2
Write to file
Write LabVIEW Measurement File
Enable
Signals
Saving Data
Writing
[1] "start": Value Change
quit
status
start
ok
0
Power off
uSMC
10
error out
Error ?!

Appendix D

Experimental data

D.1 CYL49E sensor calibration data

```
                      UNIT
MAGNET                 #        1       2
POWER SUPPLY          [V]       5.0018  5.0018
WORKING POINT 0 T     [V]       2.4950  2.4950
INCLINATION           [mT/V]    54.240  54.240
VH 0.75 mm            [V]       4.1095  3.5518
VH 6.50 mm            [V]       3.1692  3.0565
B  0.75 mm            [T]       87.570  57.321
B  6.50 mm            [T]       36.569  30.456
Teslameter 6.50 mm    [T]       37.127  31.000
```

D.2 CY-P15A tangential sensor calibration data

```
                   UNIT
MAGNET              #        1       2
CONTROL CURRENT    [mA]      1.0650  1.0650
WORKING POINT 0 T  [V]       3.8880  3.8880
VH    0.75 mm      [V]       4.0310  4.0000
VH    6.50 mm      [V]       3.9520  3.9450
```

D.3 CY-P15A normal sensor calibration data

```
                   UNIT
MAGNET              #        1       2
CONTROL CURRENT    [mA]      1.0650  1.0650
WORKING POINT 0 T  [V]       3.8420  3.8420
VH 0.75 mm         [V]       3.9880  3.9335
VH 6.50 mm         [V]       3.9030  3.8975
```

D.4 Tangential sensor Hall voltage output

```
Step    V #1    V #2
40      4.3924  4.3958
80      4.3971  4.3984
120     4.4042  4.3999
160     4.4042  4.4061
200     4.4055  4.4036
240     4.4075  4.4122
280     4.4106  4.4096
320     4.4171  4.4175
360     4.4199  4.4211
400     4.4197  4.4233
440     4.4281  4.4263
480     4.4281  4.4313
520     4.4281  4.4319
560     4.4288  4.4331
600     4.4375  4.4429
640     4.4398  4.4401
680     4.446   4.449
720     4.4493  4.4521
760     4.4531  4.4558
```

```
800     4.4546  4.4603
840     4.4604  4.4634
880     4.4616  4.4645
920     4.4654  4.4673
960     4.4701  4.4745
1000    4.4801  4.4811
1040    4.4755  4.4802
1080    4.4828  4.4865
1120    4.4891  4.4897
1160    4.4909  4.4929
1200    4.4972  4.4995
1240    4.495   4.5
1280    4.5044  4.5088
1320    4.5071  4.5122
1360    4.5128  4.5164
1400    4.5148  4.5143
1440    4.5177  4.5212
1480    4.5216  4.5215
1520    4.5217  4.5247
1560    4.5294  4.5304
1600    4.5358  4.5323
1640    4.535   4.5392
1680    4.5374  4.5334
1720    4.5419  4.546
1760    4.5447  4.5474
1800    4.5493  4.5541
1840    4.5585  4.5617
1880    4.5582  4.5592
1920    4.5624  4.5683
1960    4.565   4.5681
2000    4.5752  4.5777
2040    4.5761  4.5757
2080    4.5823  4.5861
2120    4.592   4.5944
2160    4.5951  4.599
2200    4.5983  4.605
2240    4.604   4.611
2280    4.6143  4.6181
2320    4.6138  4.6117
2360    4.6139  4.6195
2400    4.6221  4.6189
2440    4.6212  4.626
2480    4.6227  4.6274
2520    4.6281  4.6261
2560    4.6351  4.6405
2600    4.648   4.6419
2640    4.6481  4.6521
2680    4.6515  4.6572
2720    4.6557  4.6582
2760    4.6622  4.6679
2800    4.6716  4.6716
2840    4.6748  4.679
2880    4.6739  4.6787
2920    4.681   4.6844
2960    4.6918  4.6961
3000    4.6959  4.6963
3040    4.7018  4.7077
3080    4.7079  4.7108
3120    4.7092  4.7165
3160    4.7135  4.72
3200    4.722   4.722
3240    4.7249  4.7312
3280    4.7331  4.7378
3320    4.7429  4.7449
3360    4.7468  4.7538
3400    4.7596  4.7537
3440    4.7575  4.764
3480    4.7655  4.7665
3520    4.7752  4.78
3560    4.7731  4.7791
3600    4.7816  4.7833
3640    4.7832  4.7891
3680    4.7876  4.7913
3720    4.7934  4.7933
3760    4.7995  4.8065
3800    4.809   4.8102
3840    4.8138  4.8221
3880    4.8223  4.828
3920    4.8364  4.8293
3960    4.8384  4.8372
4000    4.8431  4.843
4040    4.8507  4.8561
4080    4.8579  4.8639
4120    4.8676  4.8728
4160    4.8763  4.8723
4200    4.8874  4.8816
4240    4.8824  4.8894
4280    4.892   4.8998
4320    4.8976  4.9035
4360    4.9066  4.9148
4400    4.9095  4.9151
4440    4.9159  4.9229
4480    4.9244  4.9326
4520    4.93    4.9297
4560    4.9347  4.9416
4600    4.9388  4.9508
4640    4.9475  4.9557
4680    4.9568  4.9647
4720    4.9619  4.9684
4760    4.9704  4.9765
4800    4.9761  4.9765
4840    4.9899  4.998
4880    4.9932  4.9923
4920    4.9994  5.006
4960    5.004   5.011
5000    5.0097  5.0164
5040    5.0146  5.0163
5080    5.0298  5.0348
5120    5.0344  5.0398
5160    5.0385  5.0375
5200    5.0412  5.0427
5240    5.0476  5.0552
5280    5.0553  5.0605
5320    5.0559  5.0627
5360    5.0601  5.0607
5400    5.0703  5.0762
5440    5.079   5.083
5480    5.0828  5.0837
5520    5.088   5.092
5560    5.0983  5.0978
5600    5.1017  5.108
5640    5.1075  5.1133
5680    5.1142  5.1186
5720    5.117   5.1213
5760    5.12    5.121
5800    5.1255  5.1307
5840    5.1317  5.1318
5880    5.139   5.1355
5920    5.1383  5.1425
5960    5.1455  5.1415
6000    5.1456  5.1491
6040    5.1492  5.1516
6080    5.1514  5.1542
6120    5.1535  5.156
6160    5.1563  5.1585
6200    5.1585  5.1606
6240    5.1606  5.1619
6280    5.1619  5.163
6320    5.1627  5.1644
6360    5.165   5.1659
```

6400	5.1661	5.1674
6440	5.1675	5.168
6480	5.1677	5.1684
6520	5.1678	5.1688
6560	5.1681	5.1686
6600	5.169	5.1688
6640	5.1684	5.1682
6680	5.1676	5.168
6720	5.1679	5.1671
6760	5.1669	5.167
6800	5.1658	5.1647
6840	5.1647	5.163
6880	5.1613	5.1625
6920	5.1611	5.1592
6960	5.1588	5.1574
7000	5.157	5.1536
7040	5.1539	5.1513
7080	5.151	5.1488
7120	5.1482	5.1462
7160	5.1452	5.143
7200	5.1421	5.1419
7240	5.1393	5.1359
7280	5.1301	5.1316
7320	5.1284	5.1245
7360	5.1244	5.1189
7400	5.1227	5.1154
7440	5.1152	5.1093
7480	5.111	5.1064
7520	5.1051	5.1094
7560	5.1019	5.0973
7600	5.0973	5.097
7640	5.09	5.0835
7680	5.0808	5.0801
7720	5.0754	5.0694
7760	5.0692	5.0615
7800	5.0623	5.055
7840	5.0539	5.0491
7880	5.0483	5.0496
7920	5.041	5.0337
7960	5.036	5.0378
8000	5.0302	5.0205
8040	5.019	5.0124
8080	5.0132	5.0047
8120	5.0091	5.0052
8160	5.0031	4.9974
8200	5.0014	5.0008
8240	4.988	4.9798
8280	4.9811	4.9824
8320	4.9662	4.9731
8360	4.9665	4.9617
8400	4.9631	4.9569
8440	4.9616	4.951
8480	4.9486	4.94
8520	4.9397	4.9294
8560	4.9268	4.9181
8600	4.9253	4.917
8640	4.9186	4.9119
8680	4.9073	4.9089
8720	4.9018	4.895
8760	4.8936	4.887
8800	4.8857	4.8789
8840	4.8734	4.8674
8880	4.8744	4.869
8920	4.8687	4.8604
8960	4.8548	4.8592
9000	4.8541	4.8464
9040	4.8508	4.8442
9080	4.8417	4.8351
9120	4.8318	4.8333
9160	4.8322	4.826
9200	4.8262	4.8273
9240	4.8194	4.8133
9280	4.8078	4.8012
9320	4.8046	4.7969
9360	4.7916	4.7956
9400	4.7893	4.7898
9440	4.7749	4.7806
9480	4.7795	4.7788
9520	4.7706	4.767
9560	4.7645	4.7638
9600	4.7557	4.7512
9640	4.7549	4.7495
9680	4.7474	4.7418
9720	4.7397	4.7358
9760	4.7306	4.7243
9800	4.724	4.7237
9840	4.7185	4.7146
9880	4.7136	4.7073
9920	4.7132	4.7091
9960	4.7073	4.7069
10000	4.6989	4.6926
10040	4.6941	4.6885
10080	4.6839	4.69
10120	4.6837	4.6766
10160	4.6772	4.6782
10200	4.6688	4.6613
10240	4.6623	4.6577
10280	4.6576	4.6564
10320	4.6538	4.6478
10360	4.6466	4.6459
10400	4.6354	4.6287
10440	4.6355	4.6307
10480	4.6306	4.6274
10520	4.621	4.6235
10560	4.6218	4.6208
10600	4.6166	4.6155
10640	4.6152	4.615
10680	4.6149	4.6089
10720	4.6047	4.6084
10760	4.6056	4.6037
10800	4.6001	4.5919
10840	4.5922	4.5936
10880	4.586	4.583
10920	4.5784	4.5803
10960	4.5766	4.5709
11000	4.5716	4.5683
11040	4.5614	4.5616
11080	4.5658	4.5663
11120	4.5633	4.5587
11160	4.5528	4.5477
11200	4.5478	4.5449
11240	4.5418	4.5445
11280	4.5393	4.5372
11320	4.535	4.5303
11360	4.5256	4.5243
11400	4.5243	4.5214
11440	4.5228	4.5227
11480	4.5155	4.5117
11520	4.5112	4.5103
11560	4.511	4.5056
11600	4.5072	4.5033
11640	4.5017	4.4984
11680	4.4991	4.4932
11720	4.4944	4.4938
11760	4.4913	4.4866
11800	4.4833	4.4793
11840	4.481	4.4807
11880	4.478	4.4743
11920	4.4701	4.4636
11960	4.4662	4.4661

```
12000    4.4597  4.4625
12040    4.4618  4.4629
12080    4.4584  4.455
12120    4.4605  4.4604
12160    4.4581  4.4557
12200    4.4512  4.4495
12240    4.4479  4.4448
12280    4.4431  4.4478
12320    4.4415  4.4376
12360    4.4345  4.4285
12400    4.4277  4.4222
12440    4.4278  4.4288
12480    4.421   4.417
12520    4.4178  4.4202
12560    4.4167  4.4144
12600    4.41    4.4068
12640    4.412   4.4087
12680    4.4049  4.4048
12720    4.4045  4.4013
12760    4.3949  4.399
12800    4.3925  4.3891
12840    4.3901  4.3856
12880    4.3872  4.3856
12920    4.3878  4.3869
12960    4.382   4.3783
13000    4.3792  4.3776
13040    4.374   4.3723
13080    4.373   4.3715
13120    4.371   4.3691
13160    4.3686  4.3637
13200    4.363   4.3632
13240    4.3646  4.3631
13280    4.3601  4.3593
13320    4.3526  4.3513
13360    4.3604  4.3548
13400    4.3499  4.3464
13440    4.3517  4.3519
13480    4.3475  4.3438
13520    4.3442  4.3438
13560    4.3372  4.3376
13600    4.3372  4.3329
13640    4.3332  4.33
13680    4.3326  4.3289
13720    4.3239  4.3208
13760    4.3217  4.3182
13800    4.3154  4.3133
13840    4.3114  4.3084
13880    4.3109  4.3095
13920    4.3118  4.3092
13960    4.3114  4.3081
14000    4.3105  4.3079
14040    4.3077  4.3043
14080    4.3041  4.3042
14120    4.3036  4.307
14160    4.2982  4.3013
14200    4.2982  4.2923
14240    4.2911  4.2906
14280    4.2936  4.2931
14320    4.2929  4.289
14360    4.2913  4.2894
14400    4.2917  4.2911
14440    4.2876  4.2865
14480    4.2822  4.2795
14520    4.2829  4.2828
14560    4.2796  4.2764
14600    4.2709  4.2688
14640    4.2714  4.2689
14680    4.2696  4.2662
14720    4.2655  4.2626
14760    4.2612  4.2631
14800    4.2615  4.2611
14840    4.2574  4.26
14880    4.2565  4.2545
14920    4.2522  4.251
14960    4.2525  4.2512
15000    4.2519  4.2516
15040    4.2463  4.2437
15080    4.2428  4.2442
15120    4.2427  4.2403
15160    4.2417  4.242
15200    4.2364  4.2392
15240    4.2395  4.2376
15280    4.2339  4.2319
15320    4.233   4.233
15360    4.2323  4.231
15400    4.2277  4.2275
15440    4.2247  4.2239
15480    4.2196  4.2181
15520    4.2189  4.2176
15560    4.216   4.2171
15600    4.217   4.2136
15640    4.2124  4.2101
15680    4.2079  4.2075
15720    4.2047  4.2007
15760    4.2026  4.2018
15800    4.2037  4.2014
15840    4.2035  4.2019
15880    4.2044  4.2036
15920    4.2031  4.2023
15960    4.2016  4.2015
16000    4.1999  4.2005
```

D.5 Normal sensor Hall voltage output

```
Step     V #1    V #2
40       4.6217  3.3152
80       4.6243  3.3125
120      4.6258  3.3148
160      4.6255  3.3145
200      4.6229  3.3178
240      4.6228  3.3192
280      4.6234  3.3183
320      4.6206  3.3202
360      4.6174  3.3219
400      4.6199  3.3227
440      4.6184  3.3225
480      4.6218  3.321
520      4.6234  3.3231
560      4.6241  3.3284
600      4.6226  3.3288
640      4.6238  3.3326
680      4.622   3.335
720      4.6165  3.3362
760      4.6195  3.3368
800      4.6201  3.338
840      4.623   3.3417
```

```
880     4.6198  3.345
920     4.6206  3.348
960     4.6126  3.3477
1000    4.6135  3.3489
1040    4.6139  3.3485
1080    4.613   3.3503
1120    4.6131  3.3526
1160    4.611   3.3533
1200    4.6121  3.3569
1240    4.6134  3.3596
1280    4.6119  3.3636
1320    4.6174  3.3645
1360    4.6203  3.3718
1400    4.6204  3.3742
1440    4.6239  3.3714
1480    4.6231  3.3756
1520    4.6197  3.3831
1560    4.6197  3.3845
1600    4.6252  3.3887
1640    4.6219  3.3926
1680    4.622   3.3899
1720    4.6225  3.3932
1760    4.6241  3.3996
1800    4.6262  3.3983
1840    4.6218  3.4053
1880    4.6236  3.4037
1920    4.6245  3.414
1960    4.6212  3.4139
2000    4.6221  3.4175
2040    4.6246  3.4266
2080    4.6245  3.4289
2120    4.6214  3.4362
2160    4.6266  3.4374
2200    4.6253  3.4455
2240    4.6231  3.4482
2280    4.6247  3.4483
2320    4.6247  3.4556
2360    4.6244  3.4555
2400    4.6242  3.4681
2440    4.6262  3.4752
2480    4.6248  3.4784
2520    4.6278  3.4906
2560    4.6299  3.4937
2600    4.6287  3.5053
2640    4.6278  3.5041
2680    4.6296  3.5203
2720    4.631   3.5212
2760    4.6274  3.5338
2800    4.627   3.5436
2840    4.6262  3.5532
2880    4.6235  3.5585
2920    4.6237  3.5602
2960    4.6196  3.5736
3000    4.6235  3.5833
3040    4.625   3.5826
3080    4.6261  3.6052
3120    4.628   3.6071
3160    4.6265  3.619
3200    4.6265  3.6363
3240    4.624   3.6372
3280    4.6243  3.6604
3320    4.6244  3.6701
3360    4.6251  3.6812
3400    4.6266  3.6977
3440    4.6283  3.7107
3480    4.6232  3.723
3520    4.6285  3.7302
3560    4.6232  3.7427
3600    4.6251  3.7591
3640    4.6283  3.7613
3680    4.6247  3.7895
3720    4.6257  3.7893
3760    4.6218  3.8162
3800    4.6258  3.8354
3840    4.6187  3.8355
3880    4.6214  3.8617
3920    4.6184  3.8808
3960    4.6207  3.8919
4000    4.6252  3.9072
4040    4.6235  3.9093
4080    4.6213  3.9382
4120    4.6227  3.9553
4160    4.6237  3.9636
4200    4.6237  3.9847
4240    4.6264  4.001
4280    4.6264  4.0126
4320    4.6253  4.0149
4360    4.6256  4.0422
4400    4.6262  4.0414
4440    4.6257  4.072
4480    4.6253  4.0822
4520    4.6225  4.0968
4560    4.6208  4.1102
4600    4.6196  4.1085
4640    4.6222  4.1323
4680    4.6198  4.1482
4720    4.6195  4.1581
4760    4.6148  4.1614
4800    4.6169  4.1768
4840    4.6151  4.2036
4880    4.6168  4.2122
4920    4.6186  4.2124
4960    4.6173  4.236
5000    4.6193  4.2359
5040    4.6149  4.2549
5080    4.6194  4.2562
5120    4.6183  4.2713
5160    4.617   4.2791
5200    4.6194  4.2816
5240    4.6139  4.2991
5280    4.6114  4.2976
5320    4.6156  4.313
5360    4.6138  4.3218
5400    4.6127  4.3233
5440    4.6136  4.3374
5480    4.6112  4.3383
5520    4.6097  4.3547
5560    4.614   4.3531
5600    4.6085  4.361
5640    4.6005  4.3729
5680    4.6027  4.3765
5720    4.6071  4.3829
5760    4.6072  4.3825
5800    4.609   4.3938
5840    4.6058  4.3926
5880    4.6085  4.4052
5920    4.6058  4.4096
5960    4.6005  4.411
6000    4.6021  4.4242
6040    4.6046  4.4272
6080    4.6034  4.4349
6120    4.6016  4.4352
6160    4.6017  4.4445
6200    4.6012  4.4459
6240    4.6046  4.4495
6280    4.598   4.4455
6320    4.5951  4.4529
6360    4.5963  4.4588
6400    4.596   4.4653
6440    4.5914  4.4646
```

6480	4.5934	4.4708
6520	4.5946	4.4717
6560	4.5961	4.4773
6600	4.5979	4.4891
6640	4.5941	4.4838
6680	4.5937	4.486
6720	4.5929	4.4909
6760	4.5914	4.4971
6800	4.5922	4.4956
6840	4.5897	4.4981
6880	4.591	4.499
6920	4.5907	4.5019
6960	4.5902	4.5052
7000	4.5898	4.5125
7040	4.5886	4.5131
7080	4.5901	4.5142
7120	4.5909	4.5185
7160	4.5882	4.5182
7200	4.601	4.5186
7240	4.5964	4.5248
7280	4.5859	4.526
7320	4.5872	4.5278
7360	4.5871	4.5318
7400	4.5839	4.5314
7440	4.5827	4.5451
7480	4.5801	4.5489
7520	4.5808	4.5493
7560	4.5798	4.5461
7600	4.577	4.5506
7640	4.5765	4.5484
7680	4.5781	4.5524
7720	4.5711	4.5548
7760	4.5744	4.5582
7800	4.5739	4.5586
7840	4.5676	4.5598
7880	4.5642	4.5608
7920	4.5657	4.5624
7960	4.568	4.5651
8000	4.5645	4.5637
8040	4.5627	4.5661
8080	4.565	4.5663
8120	4.5617	4.566
8160	4.5593	4.564
8200	4.5589	4.5705
8240	4.5582	4.5732
8280	4.5607	4.5755
8320	4.5547	4.5748
8360	4.553	4.5798
8400	4.5491	4.5774
8440	4.5482	4.5764
8480	4.5442	4.579
8520	4.5498	4.5837
8560	4.5473	4.5804
8600	4.5401	4.5853
8640	4.5365	4.5833
8680	4.5247	4.5858
8720	4.5279	4.587
8760	4.5226	4.587
8800	4.5243	4.6007
8840	4.519	4.597
8880	4.5232	4.5885
8920	4.5161	4.5898
8960	4.511	4.5875
9000	4.5087	4.5894
9040	4.5091	4.587
9080	4.5024	4.5884
9120	4.5042	4.5907
9160	4.501	4.5914
9200	4.4994	4.5915
9240	4.4983	4.5925
9280	4.4934	4.5938
9320	4.4896	4.5924
9360	4.4864	4.5945
9400	4.4824	4.5943
9440	4.4843	4.5971
9480	4.4742	4.5991
9520	4.468	4.5957
9560	4.4661	4.5943
9600	4.4689	4.5919
9640	4.459	4.5977
9680	4.4546	4.5932
9720	4.45	4.5964
9760	4.4453	4.5991
9800	4.4461	4.605
9840	4.4422	4.602
9880	4.4403	4.6025
9920	4.4303	4.6009
9960	4.4329	4.6054
10000	4.4332	4.6033
10040	4.4179	4.6033
10080	4.4105	4.5995
10120	4.4031	4.6083
10160	4.4024	4.6077
10200	4.3937	4.6067
10240	4.3879	4.6092
10280	4.3837	4.6056
10320	4.3796	4.6047
10360	4.3685	4.6038
10400	4.3635	4.6032
10440	4.3575	4.6083
10480	4.3552	4.6147
10520	4.3471	4.6096
10560	4.3383	4.6112
10600	4.3315	4.6136
10640	4.3235	4.614
10680	4.3139	4.6145
10720	4.3074	4.6149
10760	4.2944	4.6115
10800	4.2892	4.6175
10840	4.2794	4.6177
10880	4.2725	4.614
10920	4.2642	4.618
10960	4.2583	4.6183
11000	4.2472	4.6157
11040	4.2365	4.621
11080	4.2269	4.6188
11120	4.2127	4.6165
11160	4.2011	4.6166
11200	4.1915	4.6151
11240	4.1779	4.6167
11280	4.175	4.6179
11320	4.1479	4.621
11360	4.1354	4.6203
11400	4.12	4.6213
11440	4.107	4.6211
11480	4.0998	4.6199
11520	4.0836	4.6243
11560	4.0695	4.6227
11600	4.0557	4.6259
11640	4.0419	4.6272
11680	4.0292	4.6284
11720	4.0142	4.6248
11760	3.9983	4.6265
11800	3.9871	4.6246
11840	3.9657	4.623
11880	3.9514	4.623
11920	3.9421	4.6213
11960	3.9252	4.6222
12000	3.9125	4.6227
12040	3.8897	4.624

```
12080    3.8782  4.6228
12120    3.8657  4.6194
12160    3.8487  4.6217
12200    3.8248  4.6199
12240    3.8183  4.6266
12280    3.8034  4.6212
12320    3.7891  4.6248
12360    3.7765  4.6281
12400    3.7608  4.6275
12440    3.7457  4.6255
12480    3.7318  4.6254
12520    3.7197  4.6299
12560    3.7092  4.6234
12600    3.6977  4.6263
12640    3.6849  4.6274
12680    3.6716  4.6243
12720    3.659   4.6251
12760    3.6512  4.6257
12800    3.6368  4.6227
12840    3.6271  4.6283
12880    3.621   4.6261
12920    3.6188  4.6271
12960    3.5961  4.6264
13000    3.5835  4.6267
13040    3.5737  4.6217
13080    3.5671  4.6203
13120    3.5603  4.6224
13160    3.5506  4.622
13200    3.5446  4.6247
13240    3.5357  4.6274
13280    3.5276  4.6269
13320    3.5203  4.6318
13360    3.5128  4.6298
13400    3.505   4.6261
13440    3.500   4.6324
13480    3.4936  4.6279
13520    3.4836  4.6273
13560    3.4775  4.6254
13600    3.4688  4.6265
13640    3.4636  4.6249
13680    3.4551  4.6246
13720    3.4539  4.6247
13760    3.4475  4.625
13800    3.4424  4.6227
13840    3.4403  4.6235
13880    3.4337  4.6239
13920    3.4318  4.6218
13960    3.4288  4.6236
14000    3.4216  4.6235
14040    3.4168  4.6219
14080    3.4175  4.621
14120    3.4113  4.627
14160    3.4049  4.6247
14200    3.402   4.6245
14240    3.3999  4.6272
14280    3.3951  4.6224
14320    3.3917  4.6213
14360    3.3925  4.6223
14400    3.3907  4.6197
14440    3.3892  4.626
14480    3.3866  4.6205
14520    3.3794  4.6215
14560    3.3751  4.6233
14600    3.3743  4.6209
14640    3.3722  4.6235
14680    3.369   4.6193
14720    3.3647  4.6173
14760    3.3592  4.6117
14800    3.3577  4.6144
14840    3.3523  4.613
14880    3.3527  4.6141
14920    3.3516  4.6153
14960    3.3514  4.6133
15000    3.3464  4.6137
15040    3.3459  4.6147
15080    3.3468  4.6161
15120    3.3455  4.6195
15160    3.3437  4.6187
15200    3.3413  4.6238
15240    3.3349  4.622
15280    3.337   4.6198
15320    3.3351  4.616
15360    3.3359  4.6192
15400    3.3313  4.6227
15440    3.3283  4.626
15480    3.3251  4.6251
15520    3.3244  4.6236
15560    3.3244  4.6241
15600    3.3223  4.6193
15640    3.3233  4.6185
15680    3.3208  4.6193
15720    3.3162  4.6212
15760    3.3182  4.6244
15800    3.3184  4.6239
15840    3.3197  4.6218
15880    3.3149  4.6235
15920    3.3136  4.6272
15960    3.3122  4.6269
16000    3.3169  4.6224
```


UNIVERSITAS